Static Aeroelastic Scaling

Design of a static aeroelastically scaled strut-braced wing wind tunnel test model

by

H.C. Prins

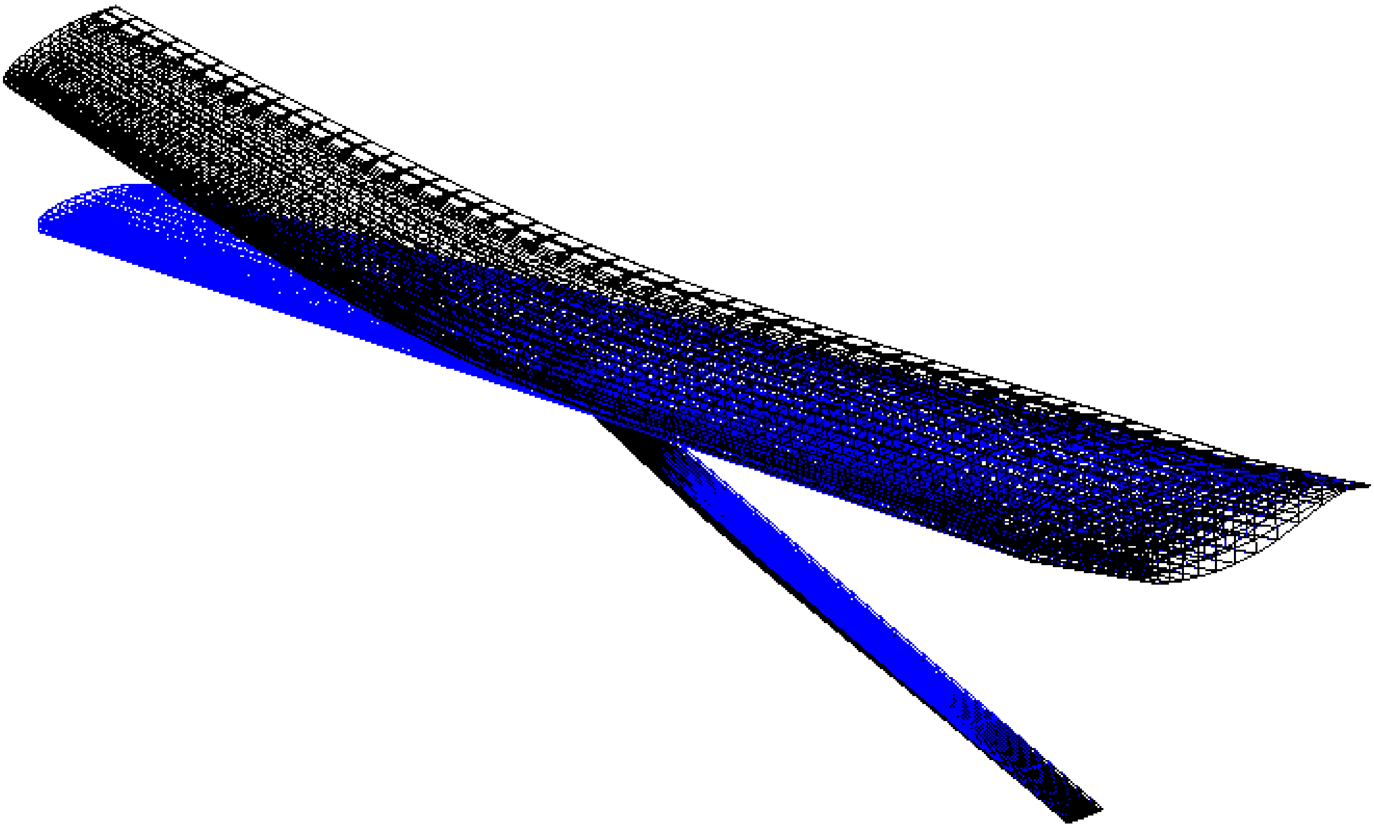

TU Delft

Static Aeroelastic Scaling

Design of a static aeroelastically scaled strut-braced wing wind tunnel test model

by

H.C. Prins

to obtain the degree of Master of Science
at the Delft University of Technology,
to be defended publicly on Friday July 17, 2020 at 9:30 AM.

Student number:	4197534	
Project duration:	June 3, 2019 – July 17, 2020	
Thesis committee:	Dr. ir. R. De Breuker,	TU Delft, supervisor
	Ir. H.S. Timmermans,	NLR, supervisor
	Dr. ir. G. La Rocca,	TU Delft, reader
	Dr. ir. D.M.J. Peeters,	TU Delft, reader

TU Delft

Preface

It has been over two years since I was offered to do my thesis at the NLR. At the time I was still in Texas, on my internship at Lockheed Martin. When I came back and was just about to start, I broke my leg in a very unfortunate icy cycling accident. I would like to thank Kees for being so patient through this time and through it all still offering me a place to do my research at the NLR. From the time I was able to walk (again), it has been Huub who has helped me shape my thesis into what it has now become. He was always one desk over for not only the big picture but was also patient for all the stupid questions I asked. Roeland accepted me, a student not from his own track, and has provided me with great feedback throughout the entire process. Together Huub and Roeland have been a great combination of supervisors and I would like to thank them for the time they invested in me and this research. I also need to thank Gianfranco la Rocca and Daniël Peeters for being part of my graduation committee and taking the time to read this thesis.

I would like to thank Brent, who I lovingly forced to read parts of my thesis, and Jennifer who willingly did so. Both provided me with useful feedback for this thesis you are now holding. Martina, you were the best project partner I could have wished for, thank you for being my sparring partner. Unfortunately, we had to do this project on our own...

I would not have been able to finish this thesis without the support of my colleagues at the NLR. I would like to thank those who have helped me directly with my thesis work but also those who kept me in good spirits with our coffee, ping pong, or pool breaks. Finally, I would like to thank my mom and all my other friends not mentioned previously for supporting me these past years of my studies.

H.C. Prins
Delft, July 2020

Abstract

Classical aerodynamic wind tunnel tests are performed with stiff or rigid wind tunnel models. Over the years wing structures have become more flexible, and with the rise of non-conventional designs, such as strut-braced wings featuring high aspect ratios, even more flexible designs have risen. To capture the aerodynamic performance of these concepts under varying load conditions, resulting in different flight shapes, a static-aeroelastically scaled wind tunnel model is required. The thesis research objective is to structurally design a static-aeroelastically scaled wind tunnel test model using optimization routines to find the optimal scaled aeroelastic characteristics representing the reference wing in wind tunnel test conditions while incorporating the safety constraints. Use cases included in the research are both an unconventional high aspect ratio strut-braced wing as well as a highly flexible cantilever wing.

To obtain aeroelastic and aerodynamic similarity, the aerodynamic similarity parameters should be the same and the elastic properties of the structure should adhere to static-aeroelastic scaling laws, which were found to solely depend on the length and pressure ratios. For finding a structure that has those elastic properties, design optimization is needed. After length scaling for the wind tunnel, little room for structural elements is left, especially in the slender strut-braced wing concept. For this reason, a composite shell with solid foam is used, as composites allow control over the directional stiffness. However, the discrete nature of composites, consisting of various layers with each a variable ply direction, complicates the optimization. To overcome this complication, lamination parameters are used to make the design space continuous, allowing the use of gradient-based solvers. An optimization framework was developed to optimize the lamination parameter space including a finite element solver in combination with scaled aeroelastic loads. The design variables considered in the optimization are the lamination parameters and the thicknesses of the laminate with the root mean square of the difference in deformation as objective. After optimizing in the lamination parameter space, the stacking sequence is retrieved using an open-source tool, OptiBless.

The results showed that the design space of the unconventional strut-braced wing configuration is highly non-convex which results in finding local minimum solutions. For a cantilever wing, the optimization is much more robust, as the optimization yields comparable results for multiple starting points which can be considered as the global optimum. The optimization framework developed was able to design a static-aeroelastically scaled wind tunnel model, consistently resulting in a representative match in terms of deformation with the full-scale design for the cantilever wing. For the strut-braced wing, a representative match can also be found but these results were inconsistent. The optimization framework proved to be successful to optimize composite designs for cantilever wings. For non-conventional designs, this method is less powerful as using a great number of starting values is required, diminishing the computational benefit of using a gradient-based solver, and other strategies could be considered that may yield better results.

Contents

Acronyms

AGILE **A**ircraft 3rd **G**eneration MDO for **I**nnovative Co**ll**aboration of Heterogeneous Teams of **E**xperts

BFO Bacterial Foraging Optimization

CFD Computational Fluid Dynamics
CLPT Classical Laminated Plate Theory
CPACS Common Parametric Aircraft Configuration Schema

DLM Doublet Lattice Method
DNW German-Dutch Wind Tunnels
DOF Degree(s) of Freedom

EAS Equivalent Airspeed

FEA Finite Element Analysis
FEM Finite Element Method

GA Genetic Algorithm
GD Gradient-Based Determinisic

HST High Speed Tunnel

ICA International Cruise Altitude
ISA International Standard Atmosphere

LP Lamination Parameter

MDO Multidisciplinary Design Optimization

NLR Royal Netherlands Aerospace Centre

PSO Particle Swarm Optimization

RMSD Root Mean Square Deviation

SBW Strut-Braced Wing
SPC Single-Point Constraint
SS Stacking Sequence
SSA Aeroelastic Effects on Static Stability
SSR Stacking Sequence Retrieval
SUGAR Subsonic Ultra Green Aircraft Research

TAS True Airspeed
TBW Truss-Braced Wing
TTBW Transonic Truss-Braced Wing

WAM Wind tunnel to Atmospheric Mapping

Nomenclature

A	Crossectional area	m^2
a	Speed of sound	m/s
b	Wingspan	m
C_D	Drag coefficient	-
$C_{D,0}$	Zero-lift drag coefficient	-
C_f	Friction coefficient	-
C_L	Lift coefficient (3D)	-
C_l	Lift coefficient (2D)	-
C_M	Aerodynamic moment coefficient	-
c	Chord	m
D	Drag	N
E	Euclidean distance	-
E	Material Young's modulus	Pa
EA	Axial rigidity	N
EI	Bending rigidity	$N \cdot m^2$
e	Oswald factor	-
F	Force	N
f	Distributed force	N/m
$f_k\left(\theta_j, \theta_i\right)$	Coefficient function of ply drop between j and i	-
G	Material shear modulus	Pa
GJ	Torsional rigidity	Nm^2
h	Laminate thickness	m
I	Area moment of inertia	m^4
J	Torsion constant	m^4
k_x	Scaling ratio of parameter x	-
L	Lift	N
L	Reference length	m
M	Aerodynamic moment	Nm
M_a	Mach number	-
N	Difference in number of plies between thicker and thinner laminate	-
p	Pressure	Pa
Qxx	Reduced stiffness (xx=11,22,12,66)	-
q	Dynamic pressure	Pa
R	Specific gas constant of air	$287\, J/(kg \cdot K)$
Re	Reynolds number	-
S	Sutherland's temperature	$110.5\, K$
S	Wing planform area	m^2
T	Temperature	K
T_0	Reference temperature	$273.15\, K$
t	Thickness	m
U	Stiffness invariant	-
V	Airspeed	m/s
X	Number of plies thicker laminate	-
x	x-coordinate	m
y	y-coordinate	m
z	z-coordinate	m
$\bar{z}$	Ply's location from the laminate centre normalized with laminate thickness	-

α	Angle of attack	$^{\circ}$
γ	Heat capacity ratio of air	1.4
δ	Deformation	m
$\theta(\bar{z})$	Ply angle at $\bar{z}$	$^{\circ}$
κ	Stiffness	N/m
μ	Dynamic viscosity	$kg/(m \cdot s)$
μ_0	Dynamic viscosity of air at reference temperature $T_0 = 273.15K$	$1.716 \cdot 10^{-5}\, kg/(m \cdot s)$
ξ	Lamination parameter	-
ϕ	Twist angle	rad

$\mathcal{AR}$	Aspect Ratio	-

$\mathbf{A}$	In-plane stiffness matrix
$\mathbf{B}$	Coupling stiffness matrix
$\mathbf{C_s}$	Structural damping matrix
$\mathbf{D}$	Out-of-plane stiffness matrix
$\mathbf{K_s}$	Structural stiffness matrix
$\mathbf{M_s}$	Structural mass matrix
$\mathbf{M}$	Out-of-plane moment resultants
$\mathbf{N}$	In-plane force resultants
$\mathbf{Q_A}$	Aerodynamic force matrix
$\mathbf{x}$	Vector of (deformed) coordinates
$\boldsymbol{\epsilon}$	Vector of mid-plane strains
$\boldsymbol{\kappa}$	Vector of plate curvature

Subscripts

max	Maximum
ref	Reference model
WT	Wind Tunnel model

1

Introduction

Wind tunnel tests are often used to verify applied methods during the design process. In recent years more lightweight materials and slender wings have been introduced to make aircraft more fuel-efficient. Generally highly stiff models have been used to assess the aerodynamic properties but this is no longer valid as the difference between the jig and flight-shape of the full scale wing has increased. Therefore properly scaled aeroelastic models need to be designed. It would be possible to create multiple rigid models that are built in the different required flight shape, but this would result in large material, mold and man hour costs. Another option is to use a single model that deforms in the same manner as the reference wing. The latter would lead to lower costs to manufacture but a more complex structure to design. Heeg et al. [1] validated a set of aeroelastic scaling laws that can be used to scale a wing to fit inside the wind tunnel. The challenge they found, however, was to find a manufacturable design that matches the required elastic properties after scaling, especially while being restricted by the wind tunnel strength requirements.

As part of the H2020 AGILE project [2], a Strut-Braced Wing (SBW) is designed and optimized. The Royal Netherlands Aerospace Centre (NLR), the company at which this thesis research takes place, wishes to be able to scale this design for a wind tunnel test in the DNW HST wind tunnel where the static aeroelastic properties are scaled to match the full-scale deformations. The H2020 AGILE SBW will be used as a reference case for this thesis as it is representative of possible wings that may be tested aeroelastically in the near future. A conventional cantilever version will also be considered in this thesis. As the slenderness of the H2020 AGILE SBW is very high, the scaled model would, therefore, be very thin. This provides a challenge for the strength requirements of the wind tunnel and it also limits the structural options for the wind tunnel model. Structural elements such as ribs are hard to fit, thus, the use of a composite shell model is considered.

The aim of this research project is, therefore, to ***structurally design a static aeroelastically scaled wind tunnel test model by writing an optimization routine that computes the structural characteristics of the composite model, such that they represent the scaled static aeroelastic characteristics of the reference wing, within its flight envelope, while incorporating the safety constraints***.

For this thesis an optimization framework is developed, capable of finding initial composite laminate designs for a composite shell wind tunnel model. The developed framework is then used to scale two wings, a conventional cantilever wing and a strut-braced wing. The methodology of the developed framework is evalutated as a whole and the results found for both wings are evaluated for the test-envelope.

This thesis starts with an overview of the found literature in chapter 2. The literature covers three main topics: strut-braced wings, aeroelastic scaling, and (aeroelastic tailoring/optimization of) composite structures. The literature review led to the methodology found in chapter 3, which discusses the steps that were to be taken in this thesis, but also the limitations of optimization framework. In chapter 4, the aeroelastic scaling parameters are derived using the formulas from literature and wind tunnel limits, and a CFD verification of aerodynamic discrepancies still present. In the next chapter, chapter 5, the objective of the optimization is determined, namely the full-scale static aeroelastic results, which can be scaled with the factors found in the chapter before it. The FEM model set-up of the wind tunnel model is discussed in chapter 6, which includes a sensitivity analysis of the mesh size. Chapter 7 discusses the optimization process. These latter two chapters together describe the developed framework and the design choices made in the process. The results of this thesis, shown in chapter 8, analyze the performance of the developed framework for various cases and show the overall capabilities of the developed framework. Finally, the thesis is concluded in chapter 9, in which also several recommendations are made for future research.

2

Literature Review

This literature review establishes the state of the art of aeroelastic scaling and composite model optimization. Also, the impact of using a strut-braced wing as a case study is researched by establishing the advantages, disadvantages, and the design impact of strut-braced wings. This is done in section 2.1, with a brief description of the use-case of this research, the H2020 AGILE SBW. Next aeroelastic scaling is discussed in section 2.2, this section discusses aeroelastic phenomena, aerodynamic scaling for wind tunnel tests, and static-aeroelastic scaling parameters. Thereafter, composite structures and aeroelastic tailoring is reviewed in section 2.3. Here an overview will be given of the state of the art of designing composite models and optimizations strategies for composite design.

This literature review is meant to set a framework for the research in this thesis. As such it does, albeit focusing on the general, include an introduction to specifics for this thesis.

2.1. Strut-Braced Wings

In this section strut-braced wings (SBW) will be discussed. First, a short introduction to the aerodynamic and structural (dis)advantages of strut-braced wings is given. Next an overview of the AGILE model, one of the reference models for this research, is presented.

A strut-braced wing is a wing that is supported by an external strut. Generally, the main wing has a high-wing configuration and the strut is placed somewhere near the bottom of the fuselage and is connected to the wing about halfway along the wing's span. Strut-braced wings are not a new concept, struts or trusses were used in some of the very first aircraft. However, the external structures caused a drag penalty and replacing this idea with a cantilever wing with a bigger thickness to chord ratio was found to be more efficient in terms of drag. However, using a strut allows for a longer wing with minimal weight penalty as the strut relieves some of the bending moment. The Transonic Truss-Braced Wing (TTBW)[1] concept, in development by Boeing and NASA, has an aspect ratio of 19.55, while a Boeing 787's composite wing has an aspect ratio of 11 and the aspect ratio of the conventional wing of the Boeing 747-400 is only 8 [3]. This shows the great difference between the two concepts and the potential of a SBW. When the aspect ratio ($A\!\!R$) increases the lift to drag ratio increases, as can be seen in equation (2.1). At the same time, an increase in zero-lift drag ($C_{D,0}$) decreases the lift to drag ratio. The latter will increase for a SBW as it has a larger wetted surface. For this reason, it can not be clearly said whether a SBW is better or worse than a cantilever wing.

$$\left(\frac{L}{D}\right)_{max} = \frac{1}{2}\sqrt{\frac{\pi e A\!\!R}{C_{D,0}}} \tag{2.1}$$

The relief in bending moment from the strut allows a SBW to be lighter than a cantilever wing of the same length as the wing has to be less strong. Similarly, a longer wing with the same weight is possible.

---

[1] A truss braced wing is similar to a SBW but has one or more additional juries between the strut and wing.

Such a longer, more slender, wing will result in a lower induced drag. Another option is to decrease the wing-thickness and keep the same weight, as less strength is needed. A thinner wing decreases transonic wave drag and parasite drag, which would allow for a lower sweep. The former is due to the lower velocities around the airfoil, lowering the local Mach number, thus reducing transonic effects, the latter is due to the reduced wetted area. Sweep is often used to delay shock formation in transonic flow, which, due to the reduced transonic wave drag that comes with the thinner wing, is no longer necessary. The lower wing sweep and high aspect ratio result in a larger region of laminar flow and laminar flow has a lower skin friction drag than turbulent flow of the same Reynolds number [4]. This can be seen in figure 2.1, which shows that laminar flow has a much lower friction coefficient than turbulent flow. At the same time, a higher Reynolds number can give lower total drag due to the delay in flow separation when dealing with turbulent flow, this is shown by the dip in the drag vs Reynolds number curve in figure 2.2. The Reynolds number at which this dip occurs depends on the Mach number, surface roughness, and the shape of the object in the flow. For streamlined bodies, such as airfoils, this dip is not as pronounced as for blunt bodies such as a sphere. This is because that streamlined bodies are designed such that they minimize flow separation. At larger angles of attack, the difference between Reynolds numbers may be more pronounced. It will have to be verified whether the Reynolds number differences between the full-scale and wind tunnel model pose a problem in this thesis.

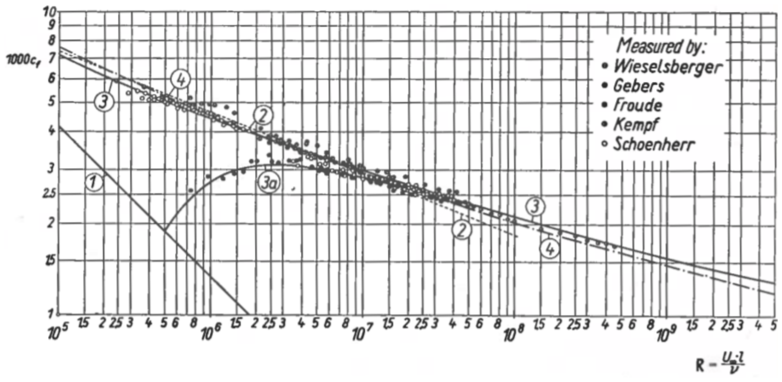

Figure 2.1: Effect of transition on the friction coefficient, for a smooth flat plate at zero incidence [4].
Curves from theory: (1) laminar (based on Blasius' theory [5], (2) turbulent (based on theory from Prandtl [6]), (3) turbulent (based on theory from Prandtl and Schlichting [7]), (3a) transition (based on theory from Schlichting [4]), (4) turbulent (based on theory from Schultz-Grunow [8])

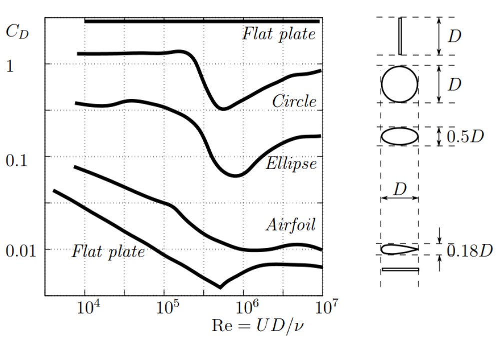

Figure 2.2: Drag coefficient vs Reynolds number for various bodies [4]

The strut does increase the zero-lift drag due to an increase in wetted area from the strut but the increase in aspect ratio at the same time decreases the induced and transonic drag. This makes that the positive effects of using a SBW can sometimes outweigh the negative, depending on the specific use. A 1978 analysis by Boeing concluded that although the strut saved wing weight and had favorable effects on the main wing, the strut buckling due to -1G load condition increased the thickness to chord ratio, t/c, of the strut so much the strut drag was too high to outweigh the benefits [9]. A current SBW study, which is not completely finished, by NASA and Boeing, called the SUGAR (Subsonic Ultra Green Aircraft Research) project does show promising results for the SBW concept so far [10–13]. An approximate decrease of 8% in fuel consumption was reported compared to a cantilever winged aircraft which was analyzed and optimized in the same way [11].

SBWs, as mentioned, offer the possibility to decrease the wing thickness without increasing the wing weight. However, the thinner airfoils result in smaller wing box dimensions, which, although capable of handling the lower load, also have a reduced torsional stiffness. This lower torsional stiffness increases the static aeroelastic deformations and may reduce the flutter and divergence speeds [14]. This makes the aeroelastic analyses of these types of wings even more important than for conventional cantilever wings. The aeroelasticity of SBWs can be analyzed similarly as conventional high aspect ratio wings, however, the interaction between the strut and the wing makes for an extra constraint for structural (FEM) analysis, as the strut 'pulls' the wing down and takes up part of the bending load of the wing from root to strut. Also, an extra interaction between the strut and wing in the aerodynamic analysis is present. Figure 2.3 shows the interference drag at the strut-wing joint, mostly due to (shock-induced) separation, at different Mach numbers. It can be seen that, even at low Mach numbers, separation occurs at the strut-wing intersection resulting in interference drag which would not occur for a cantilever wing.

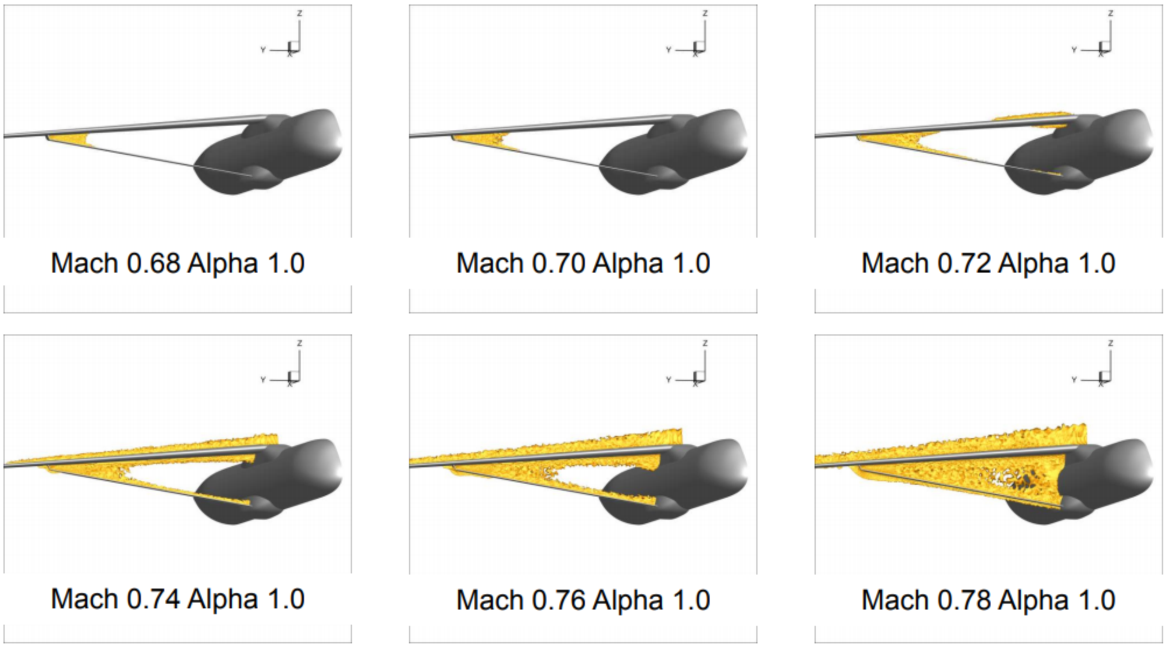

Figure 2.3: Interference drag over a SBW at various Mach numbers [15]

2.1.1. Aeroelastic Behaviour of SBWs

Non-linear aeroelasticity for fixed-wing aircraft was analyzed first to create an understanding of aeroelastic responses in transonic flight, as aerodynamic non-linearities arise from shocks and separation [16, 17]. For high aspect ratio wings, non-linear effects for the structure are important to include [17], as the geometry of the structure changes so much due to the high flexibility. Since the AGILE wing has a high aspect ratio and deals with shocks due to the strut-wing interaction, non-linear effects are of importance.

Aeroelastic testing of SBWs in wind tunnels has been done for a dynamically scaled SBW, where natural frequencies and the flutter boundary were of main interest [18, 19]. These tests showed a significant non-linear variation of the flutter boundary with different angles of attacks that seems to be characteristic to truss-braced wings [18]. No tests of a similar type as intended in this research were found, where a model is static aeroelastically scaled to match in deformations as to show aerodynamic (including transonic) effects on a strut-braced wing. Section 2.2.2 will give some more insight into aeroelastic testing.

2.1.2. SBW Configuration Studies

Several Multidisciplinary Design Optimization (MDO) studies have been performed into the optimal design of SBWs, these all focus on the wing or overall aircraft weight but some did include a constraint for the flutter boundary, flutter was shown to often be a problem for Strut-Braced Wings and thus the design driving constraint [20]. Sulaeman parameterized a SBW and looked into the effects of strut-wing junction positions. It was found that the optimum position of the junction is between 50-80% of the wingspan, values more near the tip will decrease the flutter speed and the buckling capacity while the strut will have little positive effect nearer to the root [21]. A similar study by Bhatia et al. confirmed this and suggested a junction location between 55-70% of the span [22]. They also suggest that the same or more forward sweep for the strut compared to the wing is favorable for the flutter speed. Chakraborty et al. compared the effect of using a clamped, pinned, or ball-joint for the strut-wing joint. They found that for both Strut-Braced Wings and Truss-Braced Wings there was a very small weight benefit for using a clamped strut, however, the benefit was insignificant and using a ball-joint in the model would be beneficial for production reasons [23]. Using a ball-joint results in the fact that all forces and no moments are transferred at the strut wing interaction point. This reduces the bending moment in the wing (for positive G-forces). For SBWs, the -1.0G loading condition can be critical due to strut buckling, while for cantilever wings positive loads (which are higher) are almost always critical. Naghshineh-Pour avoided this issue by suggesting a form of telescopic strut, allowing the strut to only help with bending relief but avoid strut-buckling [24].

2.1.3. Strut-Braced AGILE Model

As one of the use-cases for this research the strut-braced design of the European Horizon2020 AGILE project was chosen. The other use case is a cantilever wing version of this wing. The AGILE project focuses on the development of MDO frameworks and has used several different aircraft designs as use-cases [25].

One of them is the SBW shown in figure 2.4, which is a transonic mid-range passenger aircraft, the top level requirements for this design are shown in table 2.1.

Figure 2.4: AGILE Strut-Braced Wing design [2]

Top Level Aircraft Requirements

Passengers [-]	90
Max payload [kg]	9180
Range @ max payload [km]	3500
Mach number in cruise @ ICA [-]	0.78
Dive Mach number [-]	0.89
Initial cruise altitude [m]	11000

Table 2.1: AGILE Strut-Braced Wing design's top level requirements [26]

This aircraft is interesting because it is a Strut-Braced Wing which has a lot of data freely available and the data that is not online is (or can become) available at the NLR. This data includes the exact dimensions and mass and stiffness matrices of the optimized full-scale wing. The SBW is modeled, in the provided full-scale model, as two wing surfaces, the wing and the strut, which are connected at the strut-wing intersection with a clamped strut-wing-joint at the front spar location. The wing root is clamped while there is a ball joint at the strut root. Negative G-forces, and thus possible buckling due to the compression on the strut are not expected during wind tunnel testing and will therefore not be considered in the design and verification process.

Another use-case could have been chosen for this research as not the exact wind tunnel model design is of interest but the method of designing it. The AGILE wing is a good representation of SBWs currently under analysis for which such an aeroelastic wind tunnel test may be interesting in the near future.

2.2. Aeroelastic Scaling

In the past, some research has already been performed in (static) aeroelastic scaling for wind tunnel testing. No research was found in aeroelastic scaling for SBWs specifically, but several researchers have researched the aeroelastic scaling of conventional cantilever wings and for joined-wings.

This section first gives a brief overview of aeroelasticity in section 2.2.1, in particular static aeroelasticity equations. Next, the wind tunnel capabilities of the HST wind tunnel are presented in section 2.2.2 and how wind tunnel testing relates to aerodynamic scaling is discussed in section 2.2.3. Finally, the additional aeroelastic scaling parameters, based on the found research and derivations, will be presented in section 2.2.4.

2.2.1. Aeroelasticity

Aeroelasticity is the interaction between the forces due to aerodynamic flow and the behavior of elastic structures. As mentioned, this thesis focuses on static aeroelastic scaling, this means only elastic and aerodynamic forces are considered and inertial forces (due to acceleration) are ignored. However, for the wing to not break in the wind tunnel the dynamic instability boundary mustn't be crossed, this phenomenon is known as flutter.

Figure 2.5 shows the relation between the aerodynamic, elastic, and inertial forces and the types of problems that happen between them. From this triangle we are particularly interested in 'SSA' the aeroelastic effects on static stability and 'L' the load distribution when deformed. At the same time, we want to keep the wing stable in the wind tunnel, therefore the instability boundaries are important too and divergence and flutter should not occur during testing conditions.

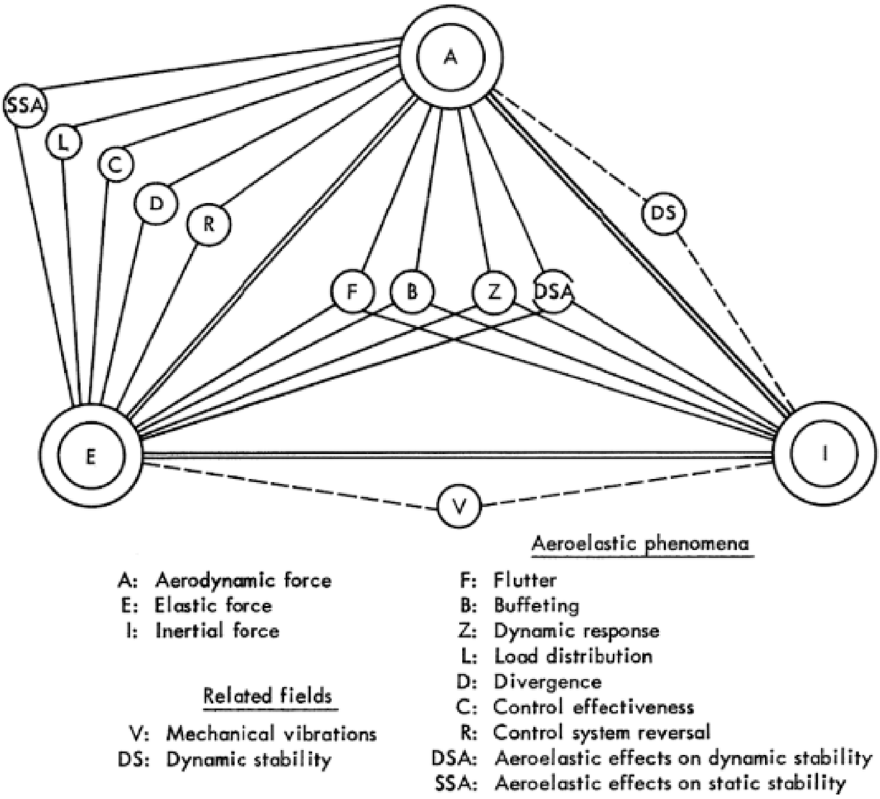

Figure 2.5: Collar's Triangle [27, 28]

In section 2.2.1.1, static aeroelasticity is discussed to explain the governing equation of static aeroelasticity needed in this thesis. Next, in section 2.2.1.2, flutter is discussed and it is explained how the flutter boundary can be computed.

2.2.1.1. Static Aeroelasticity

Static aeroelasticity focuses on the determination of the steady operating condition of an aircraft/wing while taking structural deformations into account. In this research no control surfaces will be considered, therefore control effectiveness and reversal are not considered either.

A basic differential equation, as shown in equation (2.2), represents the forces acting in the structure. Here, $\mathbf{M_s}$, $\mathbf{K_s}$ and $\mathbf{C_s}$ are the mass, stiffness and damping matrices of the structure [29, 30]. $\mathbf{Q_A}$ is a matrix of the aerodynamic forces. It follows the structure of the equations of motion of a mass-spring-damper system but with the structural (left-hand side of the equation) and aerodynamic (right-hand side of the equation) components separated. The aerodynamic forces depend, in part, on the deformations of the structure, e.g. if the structure twists the local angle of attack and thus the local lift coefficient changes.

The aerodynamic forces are mostly linearly related to the change in angle of attack. However, since the angle of attack change varies with the span due to the structural deformations this also results in a non-linearity of the total aerodynamic forces [17, 31]. Also, when shocks are present there is a discontinuity in the pressure distribution causing separation and for high angles of attack separation occurs, separation also results in a non-linearity in the aerodynamic forces. For the structure the stiffness becomes non-linear when significant changes in the initial geometry are present, this is the case for highly flexible structures, such as a high aspect ratio wing like the one in this research. Material non-linearity can also occur but this occurs when the material plastically deforms as it reaches its yield strength, which, due to the wind tunnel constraints on structural strength (see section 2.2.2), will not occur in this research. Lastly, damping forces can result in structural non-linearities [17], however, since we are looking at a static response this will not be of interest in this research either.

$$\mathbf{M_s}\ddot{\mathbf{x}} + \mathbf{C_s}\dot{\mathbf{x}} + \mathbf{K_s}\mathbf{x} = \mathbf{Q_A}(\mathbf{x}) \tag{2.2}$$

$$\text{Static: } \ddot{\mathbf{x}} = \dot{\mathbf{x}} = 0, \qquad \mathbf{K_s}\mathbf{x} = \mathbf{Q_A}(\mathbf{x}) \tag{2.3}$$

For static aeroelasticity, the time derivatives are assumed to be zero. This leaves a seemingly simple equation and only the stiffness matrix $\mathbf{K_s}$ of the structure is needed, equation (2.3). The aerodynamic forces and the stiffnesses change when the structure is deflected. For small deflections, this can be assumed to be linear, as the error with the real case would be small. However, for large deflections, the error would become too large and a linear solution is no longer accurate. It depends on the required accuracy and the properties of the structure and the forces that act upon it whether geometric non-linearity is of importance. Typically, a loop is needed to solve a non-linear aeroelastic equation when the deformations become larger. This loop stops when the forces and deformations (and thus the internal forces of the structure that withstand the aerodynamic forces) are balanced.

The aerodynamic forces may be computed using a CFD analysis, however, a lower fidelity method (such as a (higher-order) panel method) is more useful for this research as CFD is computationally much more expensive and would not be feasible for optimization. Several commercial solvers are available which could be used in this research to compute the pressure distribution on the wing. A Doublet Lattice Method (DLM) is included in NASTRAN (an available Finite Element Method (FEM) solver, see next paragraph), a higher-order version, which has a slightly higher accuracy [30] and includes wake effects, ZAERO, is available for this research as well.

The structural analysis part can be performed using Finite Element Analysis (FEA). A FEM solver can find the deformations of a specified structure under a specified load, they work by dividing a structure into various small elements which makes a complicated computation much easier to solve. Several commercial FEM solvers exist, for this research NASTRAN is available. The supplied full-scale research model is available in NASTRAN as well, allowing fast integration by using this software.

2.2.1.2. Flutter

Flutter is a dynamic instability that occurs at a certain flight speed. The flutter point is the point where the damping becomes zero and thus the wing is in a constant state of oscillation. After the flutter point, the damping is further decreased and becomes amplification, which leads to such high stresses in the structure that the wing can break. For aircraft, the flutter boundary is a set of points for different flight and loading conditions. The region within the flutter boundary is known as the flutter envelope, which must always be ~15% larger than the flight envelope [29].

The flutter point can be computed using several methods, the k-method, pk-method, and p-method are the most known. The k-method was developed first and uses a fictitious structural damping term to determine the required value to have a purely harmonic response (as the response is purely harmonic (only) in the flutter point). This damping term can then be related to the velocity. This method performs very well for predicting the flutter point but the damping values found close to the flutter point are non-physical and have no meaning. This means that it is unknown whether velocities just below the flutter point have a lot or very little damping. For this reason, the pk- and p-method were developed. The pk-method gives a more accurate representation of the frequency and damping near the flutter point, it is however also only exact in the flutter point and deviates when moving away from this point. The p-method is accurate over the entire range but does not give an exact solution due to increased numerical errors in the computation method.

When considering the topic of static aeroelasticity the k-method should be sufficient, as it would only be important that the wind tunnel model does not flutter in the test envelope.

2.2.2. (Aeroelastic) Wind Tunnel Testing

Wind tunnel tests are used to verify aerodynamic research and proposed designs. Although numerical models have improved greatly over the last decade and CFD analyses are becoming more and more accurate the validation of new designs and modeling methods is still needed. The type of wind tunnel that is chosen depends on the type of testing that is required.

Most aeroelastic wind tunnel tests are performed to analyze the flutter behavior, to make sure a design has sufficient flutter margins. Not many static aeroelastic tests were found in literature. While static aeroelasticity is often considered while performing flutter tests (as the steady-state has an effect on flutter), it is often not considered as a topic on its own during testing. For example, Xie et al. validated a structurally non-linear aeroelastic analysis method with a wind tunnel test [32]. They also compared this to a linear analysis to show the difference it makes for such a highly flexible structure. Besides their focus on the dynamic stability analysis, they showed that 'large elastic deformations make the horizontal bend mode unstable and may decrease the flutter speed'. They showed that the angle of attack for a non-linear structure has a big effect on the flutter boundary, for this, they also showed the computed static aeroelastic deformations, as they computed the structural frequencies of the deformed state. While their non-linear method succeeded in predicting the tip-deformation the model used was not a scaled model of a full-size research model.

Hooker et al. performed a static aeroelastic wind tunnel test to compare the accuracy of a 1D beam and 3D solid FEM computation method for aeroelastic deformations [33]. The tests were on a typical transonic low cantilever wing. They found that both models provided a reasonably accurate representation of the wing twist under load, but the 3D-model performed slightly better. Baker et al., while performing a dynamic test, did perform static aeroelastic tests as well to see how well their aeroelastic analysis matched the real case [34]. After creating a wind tunnel model they found the actual stiffness and torsion of the wing by doing structural tests and used these to update their static aeroelastic model. For the subsonic regime, their computations were close to the actual deformed aerodynamic performance, but once transonic effects were present their computations were far off. This shows the need for more research as models for static aeroelastic predictions in the transonic regime are still in development.

For the transonic wing used in this research, it is important to validate the aerodynamic performance while including deformations. The SBW will be tested to prove the concept as a fuel-efficient alternative to traditional cantilever wings. The most important conditions for these tests will be cruise and climbing performance as these have the largest effect on the fuel efficiency of the aircraft. Various angles of attack shall be tested to show the performance in climb, this has to be done at various pressures, reflecting the various altitudes of the full-scale model, ranging from sea level to cruise altitude. During cruise (at $M_a = 0.78$) shocks may occur due to transonic effects, as the strut has an effect of the overall aerodynamics of the wing and causes additional drag. The way the shocks form may change due to the aeroelastic deformations in the wing. Figure 2.3 clearly shows that the interference drag strongly increases when the Mach number increases, the SBW depicted is different than the research model in this thesis but is representable to what may happen with the AGILE wing. Because transonic effects are so important the High Speed Tunnel (HST) of the DNW is chosen as a possible tunnel for future tests and a reference for this research. This tunnel has a relatively large test section (compared to other sonic wind tunnels), can be pressurized, and is easily available to the NLR, at which this research takes place.

2.2.2.1. Tunnel test conditions

DNW's HST can vary the pressure and the Mach number of the flow, see Table table 2.2. The test section is 2.0 meters wide of which approximately 70% could be used for the model span without significant wall interference. The height of the tunnel can vary between 1.6 and 1.8 meter, the smaller of the two allows for a greater operating envelope (see figure 2.6). Wall interference in this direction is not a problem as the total vertical distance (including the strut) is significantly smaller than the total span.

DNW HST Wind Tunnel Operating Range

	min	max
Test Section Geometry	2.0m x 1.6m	2.0m x 1.8m
Mach Number	0.15	1.35
Pressure	25kPa	390kPa
Temperature	288K	323K

Table 2.2: DNW HST operating range

The wind tunnel requires a 3.5 safety factor on the strength of the wind tunnel model. The allowable stress should thus be at least 3.5 times higher than the maximum stress that occurs in any of the tests.

Although the temperature may vary in the wind tunnel when it is operating, the temperature lies within the range given in table 2.2 and on average is $303K$. Figure 2.6 shows the operating envelope of the HST. As can be seen, not all combinations of wind tunnel pressure and Mach are possible, for example, for the cruise Mach ($M_a = 0.78$, see section 2.1.3) the maximum pressure that can be achieved in the wind tunnel is $320kPa$ for the $2.0x1.6m^2$ test section and $290kPa$ for the $2.0x1.8m^2$ test section.

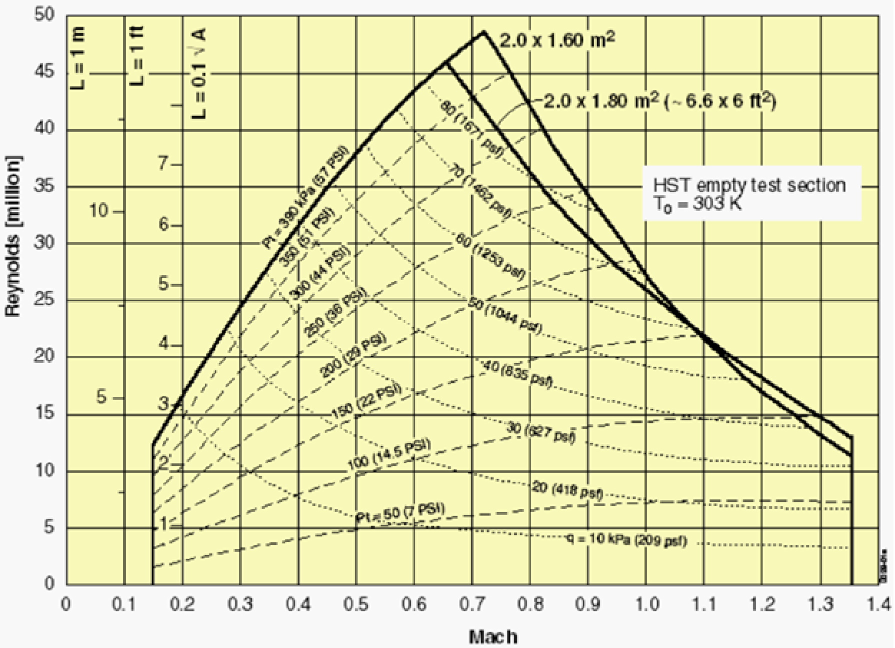

Figure 2.6: DNW's HST operating envelope

2.2.3. Aerodynamic Scaling

Aircraft are generally too large to test at full-scale, as wind tunnels can not possibly be made to have such a large test section while also being able to vary the airspeed and pressure as required. For this reason, the aircraft are scaled to fit into the available wind tunnels. The downside of this is that the way the flow interacts on the wing changes and the boundary layer thickness, turbulence, and other effects such as flow separation, are no longer accurately represented. Luckily aircraft fly the fastest at high altitudes such that they can benefit from the lower air density and thus experience less drag. When scaling the wings down the air density should increase to create comparable conditions. At lower altitudes, aircraft fly slower due to the higher air pressure which increases the drag force, which has to be compensated by the engines, and the lift force, which increases the forces on the wing and is limited by the strength of the wings.

To find out exactly what the test flow conditions should be the Reynolds number is needed, see equation (2.4). The length ratio is quickly determined from the wind tunnel size after which the flow conditions should compensate to get the same Reynolds number.

$$Re = \frac{\rho V L}{\mu} \tag{2.4}$$

For incompressible flow ($M_a < 0.3$) the velocity can be changed freely for testing of aerodynamic efficiency (as long as the new Mach number also stays below 0.3) but for higher flow velocities this is not the case and the flow conditions should also be such that the Mach number stays the same. The tests to be performed on the SBW are meant to check the transonic characteristics of the deformed wing, at these points, flow transition and separation are not a major factor of the aerodynamic properties unless induced by shocks. This means that matching the Reynolds number will be of lesser importance than matching the Mach number. The Reynolds number should however be in the same order of magnitude to give valid results [1].

$$M_a = \frac{V}{a} = \frac{V}{\sqrt{\gamma R T}} \tag{2.5}$$

As the Mach number will be known and R and γ are constants the required velocity can be expressed as a function of temperature by rewriting equation (2.5), which will later be shown in equation (2.10).

The density and the viscosity in the Reynolds number equation can also both be expressed as a function of pressure and temperature using the ideal gas law and Sutherland's law, found in equations (2.6) and (2.7). Here, S, T_0 and μ_0 are constants. Expressing the equations as functions of Mach, pressure, and temperature is beneficial as these are parameters that are influenced by the wind tunnel test.

$$\rho = \frac{p}{RT} \tag{2.6}$$

$$\mu = \mu_0 \left(\frac{T}{T_0}\right)^{3/2} \frac{T_0 + S}{T + S} \tag{2.7}$$

The Reynolds number can now be expressed as a function of Mach number, pressure, and temperature, as seen in equation (2.8). While the Mach number should be the same as for the full-scale and the temperature depends on the operating temperature during testing the pressure can be changed freely (within the wind tunnel operating range). The pressure can now vary such that they represent the full-scale Reynolds number as accurately as possible.

$$Re = \frac{\frac{p}{RT} M_a \sqrt{\gamma R T} L}{\mu_0 \left(\frac{T}{T_0}\right)^{3/2} \frac{T_0 + S}{T + S}} \tag{2.8}$$

2.2.4. Aeroelastic Scaling Parameters

Now that aerodynamic scaling is explained in the previous section the additional scaling parameters for aeroelastic similarity are discussed here.

Wan and Cesnik [35] created a methodology for the aeroelastic scaling of geometrically nonlinear structures. This was based upon the widely used methodology for geometrically linear structures created by Bisplinghoff in 1955 [27]. They noted that the main difference for geometrically non-linear structures is that the stiffness matrix should be updated for the current deformed state, whereas for linear structures only the load vectors are updated. Bisplinghoff provides seven similarity constraints, between the reference and scaled wing, with which the load distribution and elastic deformation shape are the same. These are (further) translated by Wan and Cesnik into more straight forward scaling parameters. They define scaling parameters such that only the length, speed, and density ratio need to be determined and all other scaling parameters can be derived from those.

Ting et al. [36] used a similar approach but scaled the torsion such that is had the same twist over span rather than the same twist over span percentage. This approach will not be useful for the goal of this research but the derivations presented in this paper do give a useful insight into where Wan and Cesnik's parameters are derived from as the rest of the parameters are scaled in the same way.

Heeg et al. [1] developed static aeroelastic scaling laws for a wind tunnel tests and numerically confirmed the accuracy of their scaled design, this was done for a conventional cantilever wing. This research provides insight into which factors are required for dynamic scaling but can be ignored for static scaling. They looked into the fact that the stiffness scaling depends on the flight condition scaling, which they called Wind tunnel to Atmospheric Mapping (WAM). If the dynamic pressure q is not scaled with the same parameter for each flight condition, the stiffness can also not be scaled the same for each flight condition, which is needed to be able to use only one test model. This research paved the way for this particular thesis, as the scaling laws needed are presented and confirmed. They noted that the challenge of static aeroelastic scaling lies with creating a physical model having the particular elastic properties found by scaling.

As mentioned Wan and Cesnik [35] used tree main ratios to which all others can be related; the length ratio k_b, the density ratio k_ρ and the speed ratio k_V. Essentially the wind tunnel is able to indeed influence these three ratios but it may be interesting to use k_b, k_{Ma}, k_p and k_T, the length, Mach, pressure and temperature ratio, instead, as these are determined by the HST. The length ratio can best be defined by the span ratio, as the span is generally the limiting factor for the size of wind tunnel models and is based on the wind tunnel width, this ratio can then be used to scale other geometrical coordinates. Equation (2.9) shows the relationships between the reference (ref) and wind tunnel (WT) model. Next, all other scaling parameters can be defined from these four, after these parameters are defined by wind tunnel size, Mach and (if possible) Reynolds number scaling as in section 2.2.3.

$$k_T = \frac{T_{WT}}{T_{ref}} \qquad k_p = \frac{p_{WT}}{p_{ref}} \qquad k_{M_a} = \frac{M_{a_{WT}}}{M_{a_{ref}}} \qquad k_b = \frac{b_{WT}}{b_{ref}} \tag{2.9}$$

The density ratio can be defined by the pressure and temperature ratios via equation (2.6). In the same manner, the velocity ratio can be defined by the Mach and temperature ratio via equation (2.5). These ratios can then be defined as in equations (2.10) and (2.11). From the velocity and density ratio, the dynamic pressure ratio can be determined. Later on, in this section, it is shown that the temperature ratio will not affect the static deformations since the stiffness scaling only depends on the dynamic pressure which in turn only depends on the pressure and Mach ratio and the temperature ratio can be canceled. The temperature does still affect the Reynolds number and therefore on how well the Reynolds number (equation (2.8)) is scaled for each condition.

$$V = M_a\sqrt{\gamma R T} \qquad \Longrightarrow k_V = \frac{V_{WT}}{V_{ref}} = \frac{M_{a_{WT}}\sqrt{\gamma R T_{WT}}}{M_{a_{ref}}\sqrt{\gamma R T_{ref}}} \qquad \Longrightarrow k_V = \frac{M_{a_{WT}}}{M_{a_{ref}}}\sqrt{\frac{T_{WT}}{T_{ref}}} = k_{M_a}\sqrt{k_T} \tag{2.10}$$

$$\rho = \frac{p}{RT} \qquad \Longrightarrow k_\rho = \frac{\rho_{WT}}{\rho_{ref}} = \frac{\frac{p_{WT}}{RT_{WT}}}{\frac{p_{ref}}{RT_{ref}}} \qquad \Longrightarrow k_\rho = \frac{k_p}{k_T} \tag{2.11}$$

$$q = \frac{1}{2}\rho V^2 \qquad \Longrightarrow k_q = k_\rho k_V^2 \qquad \Longrightarrow k_q = \frac{k_p}{k_T}\left(k_{M_a}\sqrt{k_T}\right)^2 = k_p k_{M_a} \tag{2.12}$$

Next, the bending rigidity's scaling parameter is defined. For this firstly the wing will be assumed to act as a cantilever beam with a constant distributed force under a small deformation [1]. This simplifies the problem to derive the scaling factor. Figure 2.7 shows the schematic of this problem. Here there is

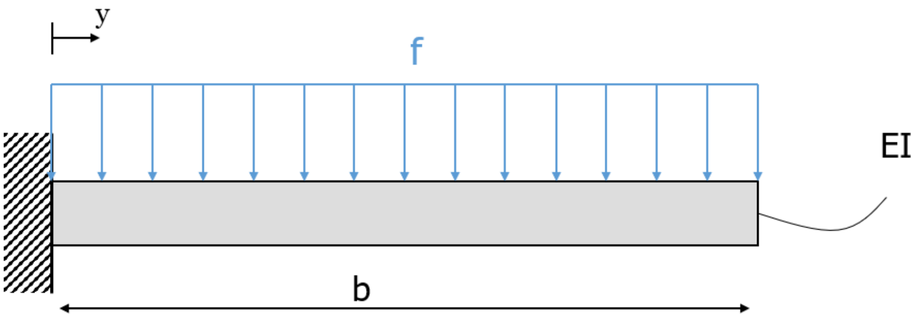

Figure 2.7: Cantilever beam with a distributed load f

a uniform pressure distribution f over the cantilever wing with span b. EI is assumed constant in the wing as well.

Now the bending deformation of such a beam can be defined by equation (2.13) [1, 37]. All parameters are non-dimensionalized using L, ρ, V and EI_0, resulting in the non-dimensional parameters indicated with an apostrophe ('). The distributed force is scaled assuming it is a distributed lift force (in this equation $F' = C_L$, the 3D lift coefficient and $f' = C_l$, the 2D lift coefficient).

$$\Delta z = \frac{f}{EI}\left(\frac{y^4}{24} - \frac{y^3 b}{6} + \frac{y^2 b^2}{4}\right) \tag{2.13}$$

$$\begin{array}{lcl}
F = \frac{1}{2}\rho V^2 S F' & & \\
b = L b' & & \\
S = L^2 S' & \Longrightarrow & F = \frac{1}{2}\rho V^2 L^2 S' F' \\
f = \frac{F}{b} & \Longrightarrow & f = \frac{\frac{1}{2}\rho V^2 S' L^2 F'}{L b'} \\
f' = \frac{F'}{b'} & \Longrightarrow & f = \frac{1}{2}\rho V^2 S' L f' \\
\Delta z = \Delta z' L & & \\
EI = E' I' E I_0 & & \\
y = y' L & &
\end{array} \tag{2.14}$$

$$\begin{aligned}
\Delta z' L &= \frac{f' \frac{1}{2}\rho V^2 S' L}{E' I' E I_0}\left(\frac{y'^4 L^4}{24} - \frac{y'^3 b' L^4}{6} + \frac{y'^2 b'^2 L^4}{4}\right) \\
\Delta z' &= \left(\frac{\rho V^2 L^4}{E I_0}\right)\left(\frac{f' S'}{E' I'}\left(\frac{y'^4}{24} - \frac{y'^3 b'}{6} + \frac{y'^2 b'^2}{4}\right)\right)
\end{aligned} \tag{2.15}$$

Now, as for similarity it is needed that all non-dimensional parameters in equation (2.15) are the same for the full-scale and scaled version, the similarity parameter for the bending rigidity can be derived as shown in equation (2.16). As can be seen, the stiffness scaling depends on the scaling of the density times velocity squared, and thus on the dynamic pressure, the scaling factors between the different flight conditions thus should be the same to be able to use one scaled model with a certain stiffness scaling. Heeg et al. first created a mapping of the to-be-tested flight conditions and from that determined a dynamic pressure scaling that was feasible in the chosen wind tunnel for all those conditions. This meant that the Reynolds number in some conditions was further off than possible with that wind tunnel as it depends on the highest Reynolds number test case what the dynamic pressure scaling is [1]. The temperature scaling factor has no effect on the scaling of the bending stiffness. This is a good thing in this research, as the temperature scaling will be different for the different flight conditions. As is does not change in the chosen wind tunnel but does for the full-scale flight at different altitudes.

$$\begin{aligned} \left(\frac{\rho V^2 L^4}{EI_0}\right)_{WT} &= \left(\frac{\rho V^2 L^4}{EI_0}\right)_{ref} \\ k_{EI} &= \frac{(EI_0)_{WT}}{(EI_0)_{ref}} \qquad \Longrightarrow k_{EI} = k_\rho k_V^2 k_b^4 = k_p k_{M_a} k_b^4 \end{aligned} \tag{2.16}$$

The scaling of forces on the wing can be derived from equation (2.14) as the non-dimensional parameters S' and F' are again constant. The force ratio can be found in equation (2.17). This equation can be used to scale the lift and drag forces acting on the wing.

$$\begin{aligned} \left(\frac{F}{\frac{1}{2}\rho V^2 L^2}\right)_{WT} &= \left(\frac{F}{\frac{1}{2}\rho V^2 L^2}\right)_{ref} \\ k_F &= \frac{F_{WT}}{F_{ref}} \qquad \Longrightarrow k_F = k_\rho k_V^2 k_b^2 = k_p k_{M_a} k_b^2 \end{aligned} \tag{2.17}$$

The aerodynamic moment can be scaled in a similar fashion as is shown in equation (2.18).

$$\begin{aligned} M &= \frac{1}{2}\rho V^2 S c C_M \qquad \Longrightarrow \qquad \left(\frac{M}{\frac{1}{2}\rho V^2 L^3}\right)_{WT} = \left(\frac{M}{\frac{1}{2}\rho V^2 L^3}\right)_{ref} \\ k_M &= \frac{M_{WT}}{M_{ref}} \qquad \Longrightarrow \qquad k_M = k_\rho k_V^2 k_b^3 = k_p k_{M_a} k_b^3 \end{aligned} \tag{2.18}$$

Where the force distribution leads to scaling of the bending rigidity the moment distribution leads to scaling of the torsional rigidity. The wing rotation can be modeled as a beam such as in figure 2.8, then the equation for the twist angle at position y under torsion M is given by equation (2.19). The twist should be the same for the full-scale and wind tunnel model as that will allow for geometric scaling in all dimensions. The torsional rigidity ratio is found with equation (2.20) [36].

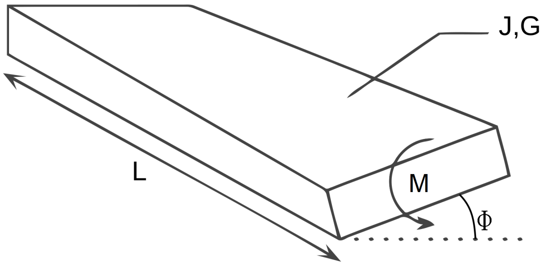

Figure 2.8: Beam under twist, showing the relevant parameters [38]

$$\Delta\phi = \frac{My}{GJ} \tag{2.19}$$

$$(\Delta\phi)_{WT} = (\Delta\phi)_{ref} \qquad \Longrightarrow \qquad \left(\frac{My}{GJ}\right)_{WT} = \left(\frac{My}{GJ}\right)_{ref}$$

$$k_{GJ} = \frac{(GJ)_{WT}}{(GJ)_{ref}} = \frac{(My)_{WT}}{(My)_{ref}} \qquad \Longrightarrow \qquad k_{GJ} = k_M k_b = k_\rho k_V^2 k_b^4 = k_p k_{Ma} k_b^4 \tag{2.20}$$

Finally, the axial rigidity EA can be scaled as well, although less important for the main wing, as axial deformation is negligible, this will be important for the strut. The extension of a beam can be computed using equation (2.21) which leads to the axial rigidity ratio found in equation (2.22).

$$\Delta y = \frac{FL}{AE} \qquad \Longrightarrow \qquad AE = \frac{FL}{\Delta y} \tag{2.21}$$

$$k_{AE} = \frac{(AE)_{WT}}{(AE)_{ref}} \qquad \Longrightarrow \qquad k_{AE} = k_F = k_\rho k_V^2 k_b^2 = k_p k_{Ma} k_b^2 \tag{2.22}$$

Finally general relations for the stiffness similarity can be defined, see equation (2.23). Stiffness is defined as $\kappa = \frac{F}{\delta}$, where F is the force and δ is the resulting deformation.

$$k_\kappa = \frac{\kappa_{WT}}{\kappa_{ref}} = \frac{\left(\frac{F}{\delta}\right)_{WT}}{\left(\frac{F}{\delta}\right)_{ref}}$$

$$k_\kappa = \frac{k_F}{k_b} = k_\rho k_V^2 k_b = k_p k_{M_a} k_b \tag{2.23}$$

The scaling parameters for bending, torsional en axial rigidity have been derived from simple beam models with simple load cases, however, the found ratios should be valid for more complex structures. Care should be taken to use the correct forces and moments as they will not be uniform over a wing. Also, the stiffnesses will not be uniform over the wing and should, therefore, be scaled for each discretized section.

While it may be easy to say that the rigidities and stiffnesses can be scaled by a simple factor it does not that easy to design a structure with those specific rigidities and stiffnesses. What is shown in this section, though, is that only the pressure, Mach, and length scaling parameters influence the static deformations. The Mach, dynamic pressure, and Reynolds number have an effect on the aerodynamic forces, where only the Reynolds number is dependant on the temperature in the wind tunnel.

2.3. Composite Structures and Aeroelastic Tailoring

A wind tunnel model design is almost always very different from the full-scale model design. It will not always contain the same structural elements (e.g. spars, ribs, stringers) and does not have to be built from the same type of materials. The wind tunnel model is constraint by the wind tunnel geometry, as SBW's have a very large span compared to its wing chord thickness there is very little space left in the wind tunnel model for internal structures, if any at all. This necessitates the use of a different structural concept and materials. For this research, it is intended to use a carbon- or glass-fiber composite airfoil skin with a foam core to prevent buckling. The full-scale reference model contains a wing box type structure with two spars and several ribs.

Composites have the benefit of creating more design freedom in terms of directional strength and stiffness, however, this freedom comes at a cost of complexity. Metal design problems can usually be reduced to the determination of a single thickness for each section [39]. For composites, it becomes much more complicated and the number of plies and the fiber orientation should be determined for each section. This makes the use of optimization techniques essential.

To create a composite model with the required aeroelastic properties aeroelastic tailoring can be used. Aeroelastic tailoring is defined by Shirk [39] as ”the embodiment of directional stiffness into an aircraft structural design to control aeroelastic deformation, static or dynamic, in such a fashion as to affect the aerodynamic and structural performance of that aircraft in a beneficial way”. Especially with the rise of composites, aeroelastic tailoring became interesting, as using a specific direction of fibers can create a coupling between bending and torsion. This concept was explored as early as 1949 by Munk [40] where he used the directions of the grain in wood to tailor propeller blades to deform favorably under load. Once fiber reinforced composites, mathematical programming methods and computers became more advanced aeroelastic tailoring matured as well. The fiber reinforced composites in a larger design space as the direction of the fibers is added. The mathematical programming advancements made it much easier for designers to consider multiple design options for composite wings.

For this research, aeroelastic tailoring is intended to be used to create a certain static aeroelastic behavior. In contrast to earlier work where aeroelastic tailoring is most widely used for the optimization of the (wing) weight [39, 41, 42] or to increase the flutter speed to acceptable values [20, 43].

This section starts with a general review of composite laminates which is followed by section 2.3.2 which discusses the two main ways of expressing a laminate. As a Stacking Sequence (SS) or as Lamination Parameters (LP), the latter is discussed further as it is found useful in optimization. The constraints on the lamination parameters are also further discussed.

2.3.1. Laminate Types and Behaviour

For production purposes not all laminates are possible. Often laminates consist of only one type of ply with one single thickness. These plies are unidirectional (all fibers in the same direction) or fabric plies (woven plies with 2 perpendicular directions). The combination of the plies can be described with a stacking sequence, where the angles of the plies are described with respect to one reference direction for the plate. In many cases laminates are symmetrical around the mid-plane, having the same types of plies at the top and the bottom. Balanced laminates are laminates that have a $-\theta$ ply for each θ ply. Quasi-isotropic laminates are laminates that have a similar stiffness in each direction, this is achieved by using a stacking sequence where there is no direction that has more plies than another by dividing the 180-degree range of directions by the number of plies [44].

Having an unbalanced and/or asymmetrical laminate can help attain certain torsion/bending coupling properties, however, for production purposes having an asymmetrical laminate can leave residual stresses in the material or result in torsion and/or bending of the unloaded structure respectively due to thermal effects. Therefore most laminates are symmetrical laminates, which decouples membrane stresses (in-plane) from bending stresses (out of plane) and stretching from shearing deformations [44].

While a lot of production methods require the composite part to go into an oven to cure, the facilities at the NLR are capable of curing the laminate at room (or low) temperature [45]. This means that symmetrical laminates may be possible, however, a symmetrical laminate is still preferred as the wind tunnel's temperature rise may be significant enough to still induce some thermal effects. Unbalanced laminates should not be a problem for the intended purpose [45] as the thermal effects on the structure are less significant. Using only -45/0/45/90 plies is an often-used design rule and will limit the design space. Delamination occurs faster if many of the same plies are used after each other and if the angle between two layers is high, it is therefore recommended to use -45/45 layers in between 0/90 and vice versa and to not have more than ~3 layers of the same angle after each other[45, 46]. Also, some plies (~10%) should be present for each of the four directions even if they are not needed for the load cases, to supply sufficient strength around holes and for physical movement of the part in preparation for testing [45, 46].

Since the wing will have a varying cross-section and an unequal load distribution the laminates will differ throughout the wing. The different sections have to be blended such that they can be manufactured and to minimize stress concentrations. A laminate can be blended in several ways, traditionally the two main types were inward and outward blending, which can be seen in figure 2.9.

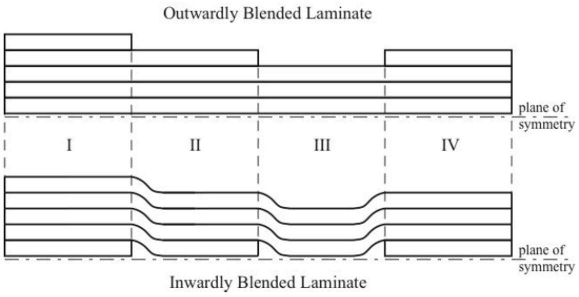

Figure 1. Inward and outward blending.

Figure 2.9: Inward and outward blending [47]

Adams et al. [48] simplified blending problems by using a guide based approach where the thinner laminates are obtained by deleting plies from a thicker stack, thus ensuring continuity. Van Campen et al. [47] suggested using 'generalized blending' which could be used for such guide-based blending approaches while not being as restrictive as using only inward and outward blending. According to van Campen et al. 'two adjacent panels are completely blended if all the layers from the thinner panel continue in the thicker panel, regardless of their position along the thickness of the laminate', an example of this 'generalized blending' is shown in figure 2.10.

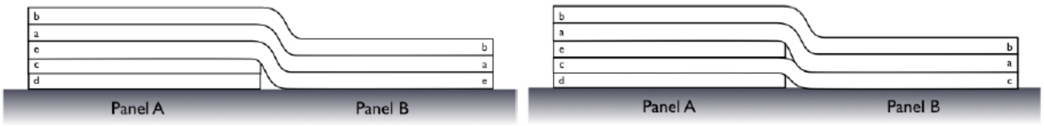

(a) According to the definition these panels are inwardly blended.

(b) These panels do not fit the definition of inward and outward blending, yet they are fully manufacturable.

Figure 2.10: a) inward blending; b) generalized blending [47]

To counteract stress concentrations it is important to drop plies one by one over a short range rather than an instant drop of all required plies at the panel transition, as was shown in both figures [45]. As the implications of these are small this step is generally not incorporated in the initial designs and only considered for a final optimized laminate. Dropping a very large number of plies between two panels, however, increases the dissimilarity between the analyzed and actual case as the required dropping distance increases.

2.3.2. Composite Design Optimization

Designing a composite structure is not as simple as designing a metal structure and most software is used to design a composite structure of sufficient strength rather than for a certain stiffness. This makes it much harder to use the standard methods of composite design. While optimization can be useful to find the best number of plies for a certain region, to get the correct bending and torsion under load, it may need a decent estimate for the starting point, which provides a challenge.

It is possible to describe the composite structure in different ways. The most obvious is the material, the number of layers, and the direction of each ply. It is also possible to describe a laminate with lamination parameters [44, 49], which could make the optimization process easier as it could make the optimization continuous. The lamination parameters only have a specific feasible region as they depend on the other lamination parameters [50, 51], this feasible region for the lamination parameters can be implemented into the optimization as constraints.

Guo et al. [43] optimized a wing for aeroelastic characteristics and for weight where the plies were the input of the optimization whereas Kameyama and Fukunaga [52] used lamination parameters. The first would give the outcome immediately after finding a solution but, if the number of layers in the laminate can vary, it would be difficult to solve. This is due to a changing number of design variables resulting in the orientations changing completely as well, creating a discontinuous problem. The latter is preferred for optimizing if the number of plies can vary throughout the optimization, but the lamination parameters would have to be translated to the actual laminate lay-up afterward as an additional step.

Lamination parameters are also useful as they create a convex design space [53], a useful property for gradient-based optimizers. The type of laminate (symmetrical, balanced, cross-ply, restrictions in ply angles, etc.) can result in a smaller number of lamination parameters. E.g. for a symmetrical laminate the coupling between in-plane stresses and curvature can be ignored. Not all laminates can be produced with every production method. The high temperatures needed for some production methods can lead to pre-stresses and deformations in unsymmetrical laminates.

Once optimal lamination parameters are found this does not mean a laminate with those exact properties may be produced, especially not when restricting the ply-angle options and when there are multiple regions in a structure with different optima. The second can be aided by added blending-constraints, which ensure generalized blending in the lamination parameter space.

Also getting back a stacking sequence that actually has those lamination parameters, is not a simple task. Multi-step optimizations are necessary. After finding an optimum in the continuous lamination parameter space a second, mixed-integer optimization has to be performed to find a stacking sequence that has those lamination parameters.

2.3.2.1. Laminate Optimization Methods

There are various methods to optimize a function, however, not all of them give the same results. As was briefly introduced in, lamination parameters are useful because they result in a continuous optimization problem, this means that gradient-based solvers can be used to find an optimum. When using the ply-angles a more complex optimization would be needed, as the number of layers, and thus ply-angle variables, depend on the number of layers. Also, this optimization would only be possible by using optimizers that can optimize discreet problems.

Guo et al. [43] compared a Genetic Algorithm (GA) to a Gradient-Based Determinisic (GD) optimizer while using ply-angles. He concluded that while the GD performed better for some initial designs the GA performed better overall. Georgiou et al. [54] compared various biology-inspired optimizers (such as GA) and compared them on a simplified version of this problem (simple box wing with 6-ply laminate where the ply orientation was optimized). The Particle Swarm Optimization (PSO) gave good results but the Bacterial Foraging Optimization (BFO) solutions showed great robustness.

When using lamination parameters most researchers have used gradient-based optimizers [52, 55, 56]. Kameyama and Fukunaga also achieved good results with a GA-solver [52], but favored this only because they wanted to study the discontinuity of flutter speed due to switching in flutter mode. Using a gradient-based solver is thus regarded as most favorable when using lamination parameters.

The downside of using lamination parameters is that the found optimum may not be a possible laminate as the stacking sequence is still unknown. A second optimization can find an optimal stacking sequence for the found lamination parameters. The final objective value might change slightly due to this. But the much faster convergence when using lamination parameters compared to using a stacking sequence in the first place makes this favorable.

2.3.2.2. Lamination Parameters

Using Classical Laminated Plate Theory (CLPT) it is possible to define an ABD matrix, as in equation (2.24), that connects the in-plane loads and out-of-plane moments on a laminated plate to the mid-plane strains and plate curvature. Here, $\mathbf{N}$ are the in-plane stress resultants and $\mathbf{M}$ are the out-of-plane moments. $\mathbf{A}, \mathbf{B}$ and $\mathbf{D}$ are the in-plane, coupling and out-of-plane stiffnesses respectively, $\boldsymbol{\epsilon}$ and $\boldsymbol{\kappa}$ are the mid-plain strains and plate curvatures. CLPT uses several assumptions for the laminate and plies, these can be found in literature [44, 57].

$$\begin{bmatrix}\mathbf{N}\\ \mathbf{M}\end{bmatrix} = \begin{bmatrix}\mathbf{A} & \mathbf{B}\\ \mathbf{B} & \mathbf{D}\end{bmatrix}\begin{bmatrix}\boldsymbol{\epsilon}\\ \boldsymbol{\kappa}\end{bmatrix} \tag{2.24}$$

For symmetric laminates, the $\mathbf{B}$-matrix is zero and the equations can be simplified. Using lamination parameters, as introduced by Tsai and Hahn [57], the in-plane and out-of-plane stiffness tensors can be defined $\xi_{[1,2,3,4]}^{[A,B,D]}$ as in equations (2.25) to (2.31) [50, 51, 57]. This makes it possible to only use a small set of continuous parameters to describe a laminate. For the use of lamination parameters, the different plies need to be of the same material, as otherwise the Q's from equation (2.32) would not be the same.

$$\begin{bmatrix} A_{11} \\ A_{22} \\ A_{12} \\ A_{66} \\ A_{16} \\ A_{26} \end{bmatrix} = h \begin{bmatrix} 1 & \xi_1^A & \xi_2^A & 0 & 0 \\ 1 & -\xi_1^A & \xi_2^A & 0 & 0 \\ 0 & 0 & -\xi_2^A & 1 & 0 \\ 0 & 0 & -\xi_2^A & 0 & 1 \\ 0 & \frac{1}{2}\xi_3^A & \xi_4^A & 0 & 0 \\ 0 & \frac{1}{2}\xi_3^A & -\xi_4^A & 0 & 0 \end{bmatrix} \begin{bmatrix} U_1 \\ U_2 \\ U_3 \\ U_4 \\ U_5 \end{bmatrix} \tag{2.25}$$

$$\begin{bmatrix} B_{11} \\ B_{22} \\ B_{12} \\ B_{66} \\ B_{16} \\ B_{26} \end{bmatrix} = \frac{h^2}{4} \begin{bmatrix} 0 & \xi_1^B & \xi_2^B & 0 & 0 \\ 0 & -\xi_1^B & \xi_2^B & 0 & 0 \\ 0 & 0 & -\xi_2^B & 0 & 0 \\ 0 & 0 & -\xi_2^B & 0 & 0 \\ 0 & \frac{1}{2}\xi_3^B & \xi_4^B & 0 & 0 \\ 0 & \frac{1}{2}\xi_3^B & -\xi_4^B & 0 & 0 \end{bmatrix} \begin{bmatrix} U_1 \\ U_2 \\ U_3 \\ U_4 \\ U_5 \end{bmatrix} \tag{2.26}$$

$$\begin{bmatrix} D_{11} \\ D_{22} \\ D_{12} \\ D_{66} \\ D_{16} \\ D_{26} \end{bmatrix} = \frac{h^3}{12} \begin{bmatrix} 1 & \xi_1^D & \xi_2^D & 0 & 0 \\ 1 & -\xi_1^D & \xi_2^D & 0 & 0 \\ 0 & 0 & -\xi_2^D & 1 & 0 \\ 0 & 0 & -\xi_2^D & 0 & 1 \\ 0 & \frac{1}{2}\xi_3^D & \xi_4^D & 0 & 0 \\ 0 & \frac{1}{2}\xi_3^D & -\xi_4^D & 0 & 0 \end{bmatrix} \begin{bmatrix} U_1 \\ U_2 \\ U_3 \\ U_4 \\ U_5 \end{bmatrix} \tag{2.27}$$

$$\begin{bmatrix} U_1 \\ U_2 \\ U_3 \\ U_4 \\ U_5 \end{bmatrix} = \begin{bmatrix} 3/8 & 3/8 & 1/4 & 1/2 \\ 1/2 & -1/2 & 0 & 0 \\ 1/8 & 1/8 & -1/4 & -1/2 \\ 1/8 & 1/8 & 3/4 & -1/2 \\ 1/8 & 1/8 & -1/4 & 1/2 \end{bmatrix} \begin{bmatrix} Q_{11} \\ Q_{22} \\ Q_{12} \\ Q_{66} \end{bmatrix} \tag{2.28}$$

$$\xi_{[1,2,3,4]}^A = \frac{1}{2}\int_{-1}^{1} [cos(2\theta(\bar{z})), cos(4\theta(\bar{z})), sin(2\theta(\bar{z})), sin(4\theta(\bar{z}))]\, d\bar{z} \tag{2.29}$$

$$\xi_{[1,2,3,4]}^B = \int_{-1}^{1} [cos(2\theta(\bar{z})), cos(4\theta(\bar{z})), sin(2\theta(\bar{z})), sin(4\theta(\bar{z}))]\, \bar{z}d\bar{z} \tag{2.30}$$

$$\xi_{[1,2,3,4]}^D = \frac{3}{2}\int_{-1}^{1} [cos(2\theta(\bar{z})), cos(4\theta(\bar{z})), sin(2\theta(\bar{z})), sin(4\theta(\bar{z}))]\, \bar{z}^2 d\bar{z} \tag{2.31}$$

where the z-location is normalized with the thickness: $\bar{z} = \frac{2z}{h}$

The reduced stiffnesses, which are material properties of a single unidirectional ply are given by equation (2.32). The integration shown in equations (2.29) and (2.31) can, in practice, be replaced by a summation, Bloomfelt et al. have shown this summation and its meaning to the feasible region, discussed in the next section, when optimizing with lamination parameters [51].

$$\left.\begin{aligned} Q_{11} &= \frac{E_{11}^2}{E_{11} - E_{22}\nu_{12}^2} \\ Q_{22} &= \frac{E_{11}E_{22}}{E_{11} - E_{22}\nu_{12}^2} \\ Q_{12} &= \nu_{12}Q_{22} \\ Q_{66} &= G_{12} \end{aligned}\right\} \tag{2.32}$$

Lamination parameters allow the definition of a laminate using only 13 parameters: $\xi_{[1,2,3,4]}^{[A,B,D]}$ and the thickness of the laminate h. For a symmetrical laminate, this can be reduced, the stress-strain relations are defined by only 9 variables, $\xi_{[1,2,3,4]}^{[A,D]}$, and the thickness of the laminate h, for each defined section. Although this may still be a lot of parameters, they are continuous and it has been proven by Grenestedt and Gudmundson that the feasible region is convex [53], a useful property in optimization, as a found local minimum is also a global minimum if both the feasible region and the objective function are convex[2]. For balanced laminates $\xi_{[3,4]}^{A} = 0$, as the angle pairs cancel out each other in the sine functions. When using only -45/0/45/90 plies $\xi_{[4]}^{A,B,D} = 0$, since the $sin(4\theta)$ function is then always zero, which can reduce the number of variables also [58].

2.3.2.3. Constraints on lamination parameters

Although the lamination parameters are continuous they are not independent, as they are a function of the lay-up function $\theta(\bar{z})$. The interrelations between the parameters are given by equations (2.33) to (2.35) [50, 51, 53, 59], which are the relations within either the in-plane or out-of-plane parameters. There also exists a relation between the in and out of plane parameters for orthotropic symmetric laminates, this feasible region is given by equations (2.36) and (2.37) [53]. For an optimization problem, these equations will be the non-linear constraints that can be applied to the design variables. For non-symmetrical laminates with only -45/0/45/90 plies the many added constraints for the coupling parameters were described by Diaconu and Sekine [58] and these may be found there if needed in future research.

$$2\left(\xi_1^{[A,D]}\right)^2 - 1 - \xi_2^{[A,D]} \leq 0 \tag{2.33}$$

$$\left(\xi_1^{[A,D]}\right)^2 + \left(\xi_3^{[A,D]}\right)^2 - 1 \leq 0 \tag{2.34}$$

$$2\left(1 + \xi_2^{[A,D]}\right)\left(\xi_3^{[A,D]}\right)^2 - 4\xi_1^{[A,D]}\xi_3^{[A,D]}\xi_4^{[A,D]} + \left(\xi_4^{[A,D]}\right)^2 - \left(\xi_2^{[A,D]} - 2\left(\xi_1^{[A,D]}\right)^2 + 1\right)\left(1 - \xi_2^{[A,D]}\right) \leq 0 \tag{2.35}$$

$$\frac{1}{4}\left(\xi_{1,2,3,4}^{A} + 1\right)^3 - 1 - \xi_{[1,2,3,4]}^{D} \leq 0 \tag{2.36}$$

$$\xi_{[1,2,3,4]}^{D} - \frac{1}{4}\left(\xi_{1,2,3,4}^{A} - 1\right)^3 - 1 \leq 0 \tag{2.37}$$

With the parameters above a feasible laminate is ensured. However, when a composite part is locally optimized to respond to the load distribution structural continuity should be ensured to make the design manufactureable [60]. Blending rules can be applied in the stacking sequence retrieval step but it was found by Macquart et al. that Stacking Sequence Retrieval (SSR) is much more likely to find a close

---

[2] The objective function is not necessarily convex in this thesis

equivalent in the fiber angle space if blending constraints are added in the lamination parameter design space [61, 62].

The blending constraints between two panels were derived by subtracting the equation of the thicker laminate by the thinner laminate. A general equation was derived for symmetrical laminates which relates the maximum Euclidean distance between two lamination parameter vectors to a single equation, equation (2.38).

$$\left(E_{k\ (N)\rightarrow(N-X)}^{A,D}\right)^2 - f_k\left(\theta_j,\theta_i\right)\left[\underbrace{\left(\frac{X}{N}\right)^2}_{\text{In-Plane (A)}} + \underbrace{4\left(9\left(\frac{X}{2N}\right)^2 - 36\left(\frac{X}{2N}\right)^3 + 60\left(\frac{X}{2N}\right)^4 - 48\left(\frac{X}{2N}\right)^5 + 16\left(\frac{X}{2N}\right)^6\right)}_{\text{Out-of-Plane (D)}}\right] \leq 0 \quad (2.38)$$

This generalized equation relates the in-plane (A) to the out-of-plane (D) lamination parameters. When only relating one of the two the under-braced sections of either in-plane or out-of-plane that are valid are active. In this equation, the Euclidean distance (E) is related to the difference in number of plies (X) and number of plies of the thickest of the two laminate panels (N). The equation $f_k\left(\theta_j,\theta_i\right)$ is deduced from the cosines and sines in equations (2.29) and (2.31) and was shown by Macquart et al. to lead to 3 maxima, each valid for a specific combination of k, as shown in table 2.3. Since both X and N are only used as fractions of each other these can be replaced by the difference in thickness and the thickness of the thickest of the two laminate panels, resulting in the continuous equations needed.

Values of k	$\max\limits_{\theta_j,\theta_i} f_k\left(\theta_j,\theta_i\right)$
1 or 2 or 3 or 4 or 12 or 34	4
13 or 23	5.1443
14 or 24 or 123 or 124 or 134 or 234 or 1234	6.25

Table 2.3: Maximum values of $f_k\left(\theta_j,\theta_i\right)$ for combinations of k. Adapted from [60]

It has to be noted that the shown blending constraints are conservative since they assume a ply-drop that gives the biggest impact on the new lamination parameter (90degree angles).

2.3.2.4. Strength constraints

Since lamination parameters are used it is not easy to determine the strength of the laminate, especially since the actual layup of the laminate is unknown and required for the standard methods to determine the strength of a composite. Since stresses will be unknown due to this the only way to incorporate strength constraints is to use the strain in the laminate. The failure strain, together with a safety factor can be used to impose a strength constrain on the optimization. The downside of this constrain is that the FEM analysis within the optimization is needed to find the strains present in the current design. The maximum strain for each panel ($max(\epsilon_i)$) should be lower than the failure strain (ϵ_{max}) divided by the safety factor (SF), equation (2.39).

$$max(\epsilon_i) - \frac{\epsilon_{max}}{SF} \leq 0 \quad (2.39)$$

The safety factor may need to be higher than the final required structural safety factor since the stacking sequence retrieval step results in a slightly different laminate which may reduce the final safety factor.

2.3.2.5. Stacking Sequence Retrieval

When using lamination parameters it is necessary to retrieve a stacking sequence that matches these parameters as closely as possible.

The stacking sequence retrieval is the last step in the multi-step optimization approach and it is a discreet optimization using ply-angles as design variables. Generally, the number of plies is set or heavily restricted in this stage and several manufacturing constraints can be enforced.

Several open-source tools are available to do this that have shown to give good results. Two examples of these are optiBless, a Matlab-based tool and pyTLO a recently (2019) developed python-based tool. Both use a genetic algorithm and use stacking sequence tables (SST) to find valid designs [62, 63]. Stacking sequence tables are often used as they guarantee that if a laminate is chosen from this table a manufacturable blended composite is found [64].

Both pyTLO and OptiBless work by additive SST creation, using the thinnest panel as the guide and adding plies, this showed a faster generation of feasible designs [63]. Then from the created SST, a blended composite design is created and the lamination parameters found can be compared to the required lamination parameters.

Several manufacturing constraints are added, besides the blending constraints already mentioned. Manufacturing constraints such as the 10% rule, where the laminate should contain at least 10% of plies in all of the 4 primary directions (-45/0/45/90). Ply contiguity, where plies with equal orientation should not be used over x-times in a row[3]. Disorientation, which means that two consecutive plies should not vary more than 45°. For detailed explanations of all applicable constraints and the methods used the reader is referred to the stacking sequence retrieval tools [62, 63]

---

[3] this was earlier mentioned to be 3 plies for the design rules used [45]

3

Research Objective, Questions, and Methodology

The aim for this thesis was to develop and assess an optimization framework capable of designing a static aeroelastically scaled wind tunnel test model by writing an optimization routine that computes the structural characteristics of a composite shell model, such that they represent the scaled static aeroelastic characteristics of the reference wing within its flight envelope, while incorporating safety constraints. This thesis also aims to consider the non-conventional strut-braced wing design to look into the possible complications or added constraints associated with such a design. The literature review from the previous chapter has shown that relatively simple scaling parameters exist to get aeroelastic similarity. These, however, only scale the overall elastic properties. Finding a structural design which has those properties is the next step. This chapter will discuss the methodology used in the optimization framework developed for this thesis in section 3.2. Before doing so section 3.1 will discuss the research questions this thesis aims to answer with the development of the optimization framework.

3.1. Research Questions

To reach the research objective, the main research question is defined as:

> **How can a composite laminate of a wind tunnel model be optimized such that the model's static aeroelastic characteristics represent those of the full-scale reference model for various loading conditions, in order to validate the aerodynamic performance in transonic flight including the elastic shape variations?**

Solving this research question and acting on the found answer reaches the research objective. However, it is a difficult question to answer directly. Therefore, several sub-questions were defined:

1. What are the implications of analyzing/designing a Strut-Braced Wing compared to a conventional cantilever wing?
2. How can a wing be aeroelastically scaled?
    (a) What are the applicable aeroelastic scaling laws?
    (b) What is the effect of the chosen wind tunnel on the scaling of the model?
3. How can a composite wing be optimized for a specific deflection and twist?
    (a) How can a composite wing be paremeterized for optimization?
    (b) What are suitable optimization methods for composite optimization?
    (c) Which constraints are required for composite optimization and how can these be parameterized?

Some of these questions can be partially answered using the literature review of the previous chapter. These answers were provided below and the gaps still unknown are used to set up the steps of this thesis in the next section.

1) The literature review has shown that the aeroelasticity methodology itself will not change when analzsing/designing a SBW. The relations do become more complex as there is a strut/wing interaction, leading to an extra constraint with the strut and aerodynamic interference effects near the wing-strut joint. The effects of the strut on the chosen optimization method for a composite shell still need to be analyzed within the thesis.

2a) The scaling parameters, shown by equations (2.9) to (2.11), (2.16) to (2.18), (2.20), (2.22) and (2.23), can be used to scale the model for static aeroelastic behavior. It is important that the model is scaled with a constant dynamic pressure for each flight/test condition. The stiffness of the model and the forces acting upon it can be scaled using scaling factors, which can be used for numerical verification of aeroelastic models. Physical testing will, however, still need a structural design optimized to have those properties. The scaling laws imply that if a proper match is found the aeroelastic properties are correct for all loading conditions. The error in multiple loading conditions should, however, still be considered when evaluating the optimization framework.

2b) The wind tunnel size and test condition range can be used to determine the scaling parameters k_b, k_{M_a}, k_T, k_p. Matching the Mach number is more important than matching the Reynolds number in this research as the final tests will be transonic aerodynamic tests, therefore $k_{M_a} = 1$ and the Reynolds number should be in the same order of magnitude for similarity. The Reynolds number cannot be matched by the HST wind tunnel. It should be verified in this thesis if the scaling factors may be used for this different Reynolds number. The flight conditions that are of interest can be mapped to possible wind tunnel conditions using WAM by defining a range of possible pressure scaling values.

3a/b) Composite laminates can either be expressed in the number of layers and each respective angle or be expressed in lamination parameters which express the laminate's properties in a constant number of variables. Literature has shown that lamination parameters are useful during optimization. The design space created is continuous. Gradient-based solvers are generally much faster in finding an optimum than stochastic search methods such as a genetic algorithm. The downside is that a feasible existing laminate should still be retrieved after the continuous optimization in the lamination parameter space. Making use of this bi-step optimization approach is evaluated in this thesis. The stacking sequence retrieval step likely causes a deviation from the found optimum. The implications of these should be evaluated in this thesis. For the FEM analysis, the wing has to be discretized into sections. A basic convergence study can be used to define the proper amount of elements in the FEM analysis.

3c) The optimal design should adhere to the wind tunnel safety factor. The composite optimization should also constrain the found laminate according to several production rules, they should for example ensure blending between different laminate panels. When additionally enforcing the blending constraints in the lamination parameter space, it was shown that it is easier to find an optimum [61]. The lamination parameters are interrelated and constraints should be applied to the lamination parameter design space. These constraints should be integrated into the framework.

3.2. Research Plan

A general overview of the items required for the optimization framework can be seen in figure 3.1. This overview was used during development of the optimization framework to indicate the seperate functions. This general program overview also serves as a guideline for the research plan. Detailed diagrams, including a legend, that elaborate on some of the steps can be found in appendix B.

Firstly, the scaling factors should be determined for the combination of wing and wind tunnel used. Representative test conditions will have to be determined for which the wind tunnel model should match the reference wing. The effect of Reynolds number dissimilarity should be evaluated, as this determines whether the scaling laws are valid.

Next, the objective deformations should be determined by performing the full-scale aeroelastic analysis. The found scaling factors can then be used to set the scaled objective deformations and to determine the scaled forces on the wing. The full-scale model and the scaling factors could be used to numerically

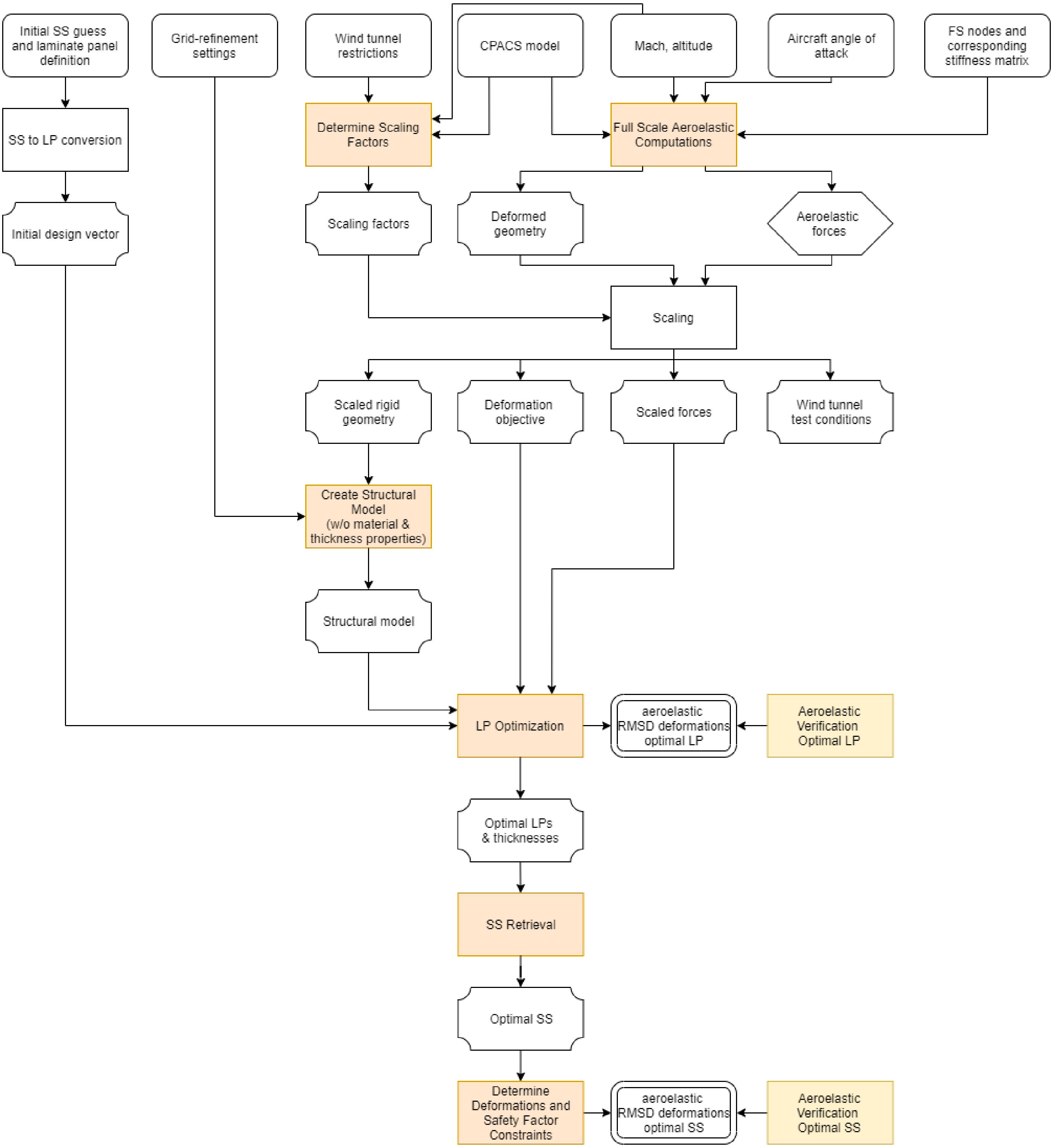

Figure 3.1: General overview of the steps performed in the thesis

verify the aeroelastic model used by using a beam model with scaled elastic properties. A single angle of attack is used for the objective of the optimization since a found design with well matching aeroelastic properties will match for all points. This angle needs to be the highest angle required in testing, as this is the limiting angle for the strength requirements.

The next step is to develop the optimization framework. This consists of two steps. Firstly, setting up the parameterized structural model. Secondly defining the optimization problem. For the structural model, the used mesh should be verified for convergence. When setting up the optimization problem, not only an objective function should be set up but also the constraints of the model and the bounds of the design space (lower and upper limits for the optimization) should be determined. Since an aeroelastic analysis is computationally more much expensive than a static FEM analysis, it was chosen to use the latter. It was also chosen to use linear methods rather than non-linear methods for this same reason. If a well-matching structure is designed the results should be the same, as the literature review has shown, even when the used analysis in the optimization is less accurate this is true. Deviations from the objective may propagate in the aeroelastic deformations which may increase the error in this step. How large these deviations are is something to investigate from the results generated by the framework.

After this, the optimization framework is ran for varying conditionsm, the found results are analyzed, and the chosen methodology is evaluated. The chosen optimization methodology (from the previous paragraph) assumes that a reasonable match is found, in which case using a linear static analysis, with the scaled forces from the objective wing, would be valid. It should thus be verified if the found optimal designs are close enough for this methodology to be used. Additionally, the differences between the cantilever and strut-braced wing will be evaluated.

Finally, the applicability of the developed optimization framework can be determined by analyzing the similarity of the wind tunnel and reference models for the entire flight envelope.

3.3. Limitations

The research plan has several limitations. Firstly, the intended designs are meant to be initial designs, therefore ignoring attachments and testing equipment that may be added to the wind tunnel model. The found initial design is intended to show applicability to the problem and, if so, can be used to determine the sizing and placements of additional elements. A design iteration will be needed in which the stiffnesses of these additional elements are taken into account before a wing can be built for wind tunnel testing. The framework does not check if the scaled wing does not flutter, this will have to be checked in the final design step. While it is not important for static scaling that the dynamic properties are the same it is still important that the wind tunnel model meets the safety requirements of the wind tunnel.

This framework is specifically developed for composite shell wind tunnel models with a foam core. Other types of wind tunnels models exist but are not evaluated in this thesis.

If a wind tunnel model design with proper stiffness similarity is not found by the lamination parameter optimizer the aeroelastic result may suffer even more, as the assumption that static and aeroelastic results are the same for a well matching model are no longer true. The same goes for using a single angle of attack's deformation and forces for the objective rather than performing a multi-objective optimization. If the found optimum has properly scaled elastic properties the other angles of attack will also show proper similarity but deviations may propagate.

Since lower fidelity tools are used in the optimization framework the actual aerodynamic resultants in the wind tunnel during testing may be different. This should have little effect on the optimization framework as the full-scale's objective is determined with the same fidelity. It should however be taken into account when looking at the aerodynamic results found by these lower fidelity tools.

The lamination parameters are restricted to symmetrical laminates and to only using -45, 0, 45, and 90 plies to reduce complexity and the number of design variables.

4

Test Conditions and Scaling Factors

As mentioned in the literature review, the scaling parameters should be chosen such that the static aeroelastic characteristics of the full-scale and wind tunnel model can be matched throughout the whole test envelope. Since this is an initial research program, exact flight envelope ranges are still unknown. Therefore, it is of importance to review a reasonable testing range to show the full possibilities of the research.

This chapter shows the method for defining the scaling parameters for the use case, the H2020 AGILE SBW. The conventional design, used as a comparison case, is a cantilever version of this wing, with the same span and flight conditions, therefore the scaling factors will be the same for this wing. In section 4.1 the range of possible scaling factors for the SBW in the HST wind tunnel are shown. Since section 4.1 shows it is impossible to match both the Mach number and Reynolds number perfectly in the HST tunnel for this wing, section 4.2 shows the CFD results of the SBW for the two different Reynolds numbers to show the effects of this mismatch on the aerodynamics. Finally, in section 4.3 a set of factors is chosen that lies within this range that will be used for the rest of this thesis.

4.1. Scaling Factors for H2020 AGILE Wing in HST

To show the benefits of the conceptual design in terms of aerodynamic efficiency, it is of interest how the wing acts in climb as well as during cruise. Several angle of attack values should thus be considered and the deformations should match for each of these. Also, several flight levels should be considered. The lower the altitude the higher the air pressure and thus the higher the dynamic pressure will be for a given Mach number. However, the Mach number at which the aircraft flies is restricted by the flight maneuvering envelope, and these velocities restrict a lower Mach number at lower altitudes. The next subsection will go into this flight maneuvering envelope for the H2020 AGILE SBW specifically. After the flight envelope is determined the scaling factors can be determined by using the wind tunnel testing ranges.

4.1.1. Flight Envelope

A full flight envelope for this research aircraft is not available but cruise and dive speeds were set at Mach = 0.78 and Mach = 0.89, respectively [2]. During this thesis, it is assumed that throughout climb, the aircraft flies at a similar cruise Equivalent Airspeed (EAS), V_C. While actual climb speeds may differ this value will be of similar magnitude and should thus provide representative test cases.

Figure 4.1 shows the flight envelope as defined by the CS-25 regulations. The aircraft would be certified to fly at speeds up to V_D, the dive Mach number, but in normal operation would fly at speeds close to V_C, which is of interest for this research pertaining to the performance of the SBW. The EAS is determined as in equation (4.1), where TAS stands for True Airspeed. The EAS of an aircraft flying at 0.78 Mach at 11000m altitude is 244kt, which is used as a reference for all the flight levels. If the EAS is the same the dynamic pressure is the same.

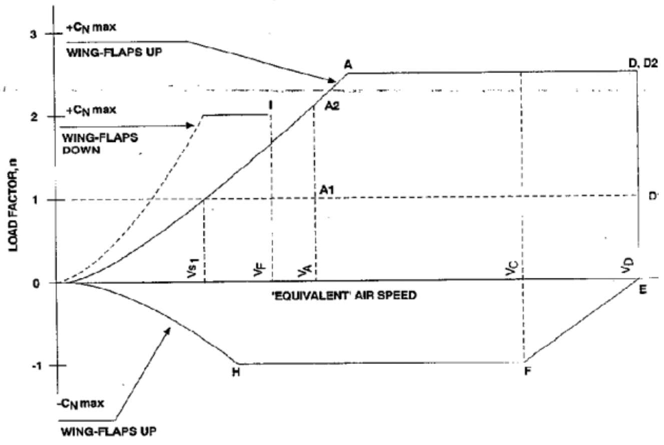

Figure 4.1: CS-25 Flight Maneuvering Envelope [65]

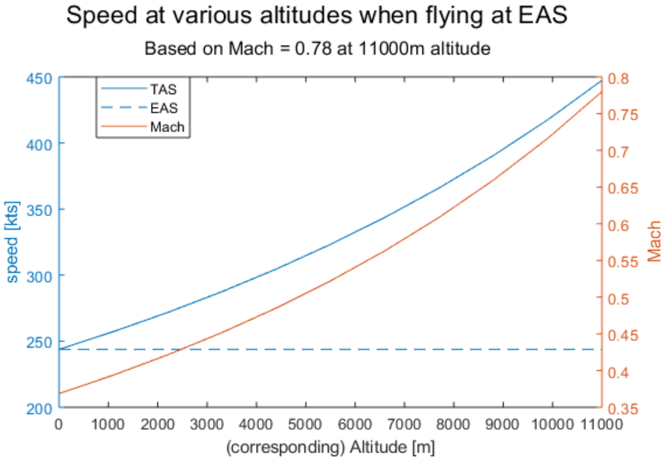

Figure 4.2: True Airspeed and Mach variation for constant Equivalent Airspeed

$$EAS = TAS\sqrt{\frac{\rho}{\rho_0}} \tag{4.1}$$

The TAS is thus different for each flight altitude and, together with the density from the ISA, can be converted to a Mach number, which for cruise altitude is 0.78, but at sea level is only ~0.4. This difference in Mach number can lead to aerodynamic differences which may lead to differences in the forces on the wing but since the dynamic pressure does not vary much throughout climb the loads are of similar proportions. Figure 4.2 shows the variation of the TAS and Mach number for different altitudes, while the EAS remains constant.

Finally, the test envelope will be the scaled equivalent of the flight envelope during climb. Within this thesis, this results in Mach numbers between ~0.4 and ~0.8 from sea level to ICA, and angles of attack between ~-2.5 to ~7.5 degrees, which gives a broad spectrum of angles.

4.1.2. Scaling Factors

Using the equations in section 2.2, all other relevant scaling parameters can be derived from 4 scaling parameters that may be varied: k_T, k_p, k_{Ma} and k_b.

As a start, $k_{Ma} = 1$, since the Mach number should be the same in the test as in the flight conditions to be able to see the transonic effects properly.

The length scaling factor, k_b, can be determined by scaling the semi-span of the wing (b_{ref}) to fit into the wind tunnel test section. The wind tunnel section is 2m wide, of which, according to the DNW, approximately 70% may be used without creating large wall interference effects[1]. k_b can thus be determined as in equation (4.2).

$$\left.\begin{aligned} b_{WT} &= y_{WT-testsection} \cdot 70\% = 1.4m \\ b_{ref} &= 18m \end{aligned}\right\} \Rightarrow k_b = \frac{b_{WT}}{b_{ref}} = 0.07\bar{7} \tag{4.2}$$

k_T, the temperature scaling parameter, is determined by the operating temperature of the wind tunnel, which varies between $288 - 323K$. Within this research the value from figure 2.6, $T_0 = 303K$, will be used as a reference. Since the forces on and the stiffness of the structure do not depend on the temperature, this parameter has no influence on the consistency of static scaling throughout the flight envelope. This is a good thing, as the temperature is different throughout different flight conditions (as

---

[1] this statement was given by DNW experts that work with the HST wind tunnel, for spans up to 70% wall correction factors can be applied with relative certainty.

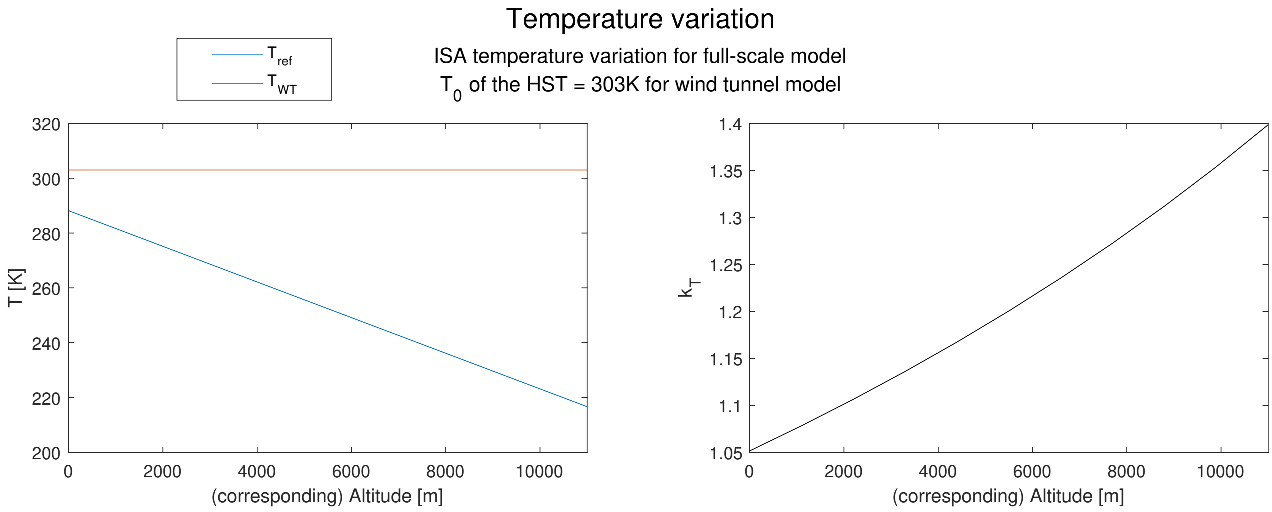

Figure 4.3: Left: Temperature in flight and in the wind tunnel. Right: k_T variation

it varies with altitude) but cannot be varied similarly for the wind tunnel test conditions. Thus, k_T is not a constant value throughout the test envelope. Figure 4.3 shows this effect. The temperature may not be exactly $303K$ during actual testing conditions, the Reynolds numbers during the tests may, therefore, be (very slightly) different than the ones shown in this report.

The last scaling factor, k_p, can be varied by the HST and is the most important factor for static aeroelastic scaling as it is directly proportionate to the scaling of dynamic pressure, the forces and the rigidity, as was shown in section 2.2.4. The pressure scaling factor k_p should be the same for all test conditions if only one aeroelastic wind tunnel model is created. As for the temperature, the pressure changes at different altitudes, therefore different pressures are needed during wind tunnel testing. In figure 4.4, the variation of the pressure scaling factor with corresponding flight altitude is shown in the left graph. The two curved lines (in yellow and red) correspond to the scaling parameter using the minimum and maximum wind tunnel pressure. Since a constant k_p is needed, only the values of k_p that lie in the shaded area are valid options and are determined by the maximum k_p of the minimum wind tunnel pressure and the minimum k_p of the maximum wind tunnel pressure. This green area corresponds to the green area in the right graph of figure 4.4, which shows the air pressures. The maximum pressure of the wind tunnel is 390kPa, for Mach numbers lower than 0.72, see figure 2.6. For higher Mach numbers, figure 2.6 shows that the maximum pressure is lower. However from the right graph in figure 4.4 it can be seen that the lower altitudes are limiting for the pressure range. These are the altitudes with lower Mach numbers as seen in figure 4.2. This therefore no longer causes a restriction allowing the 390kPa pressure to stay limiting.

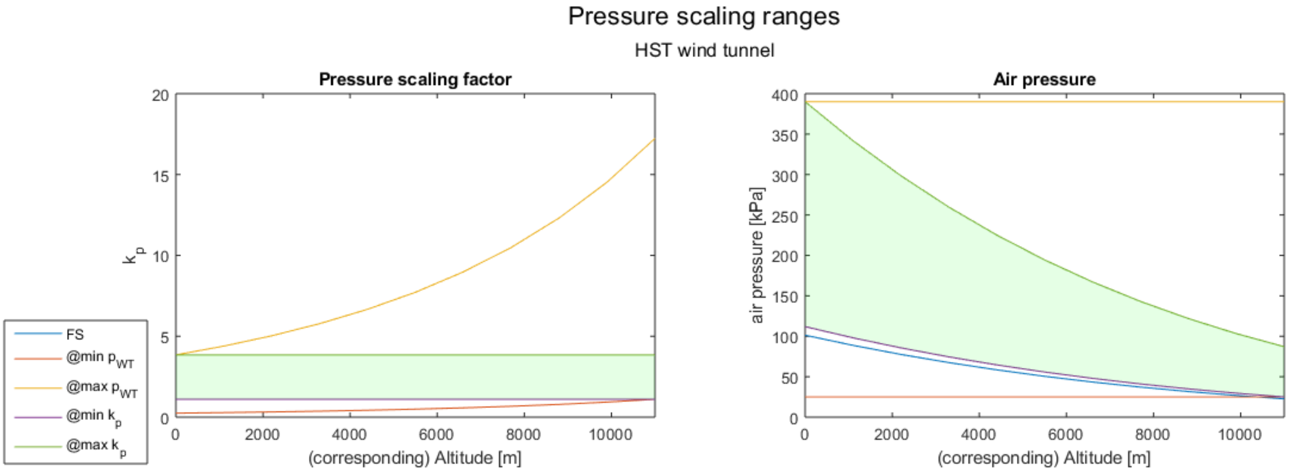

Figure 4.4: Valid pressure range of the HST that can provide a constant k_p for AGILE wing

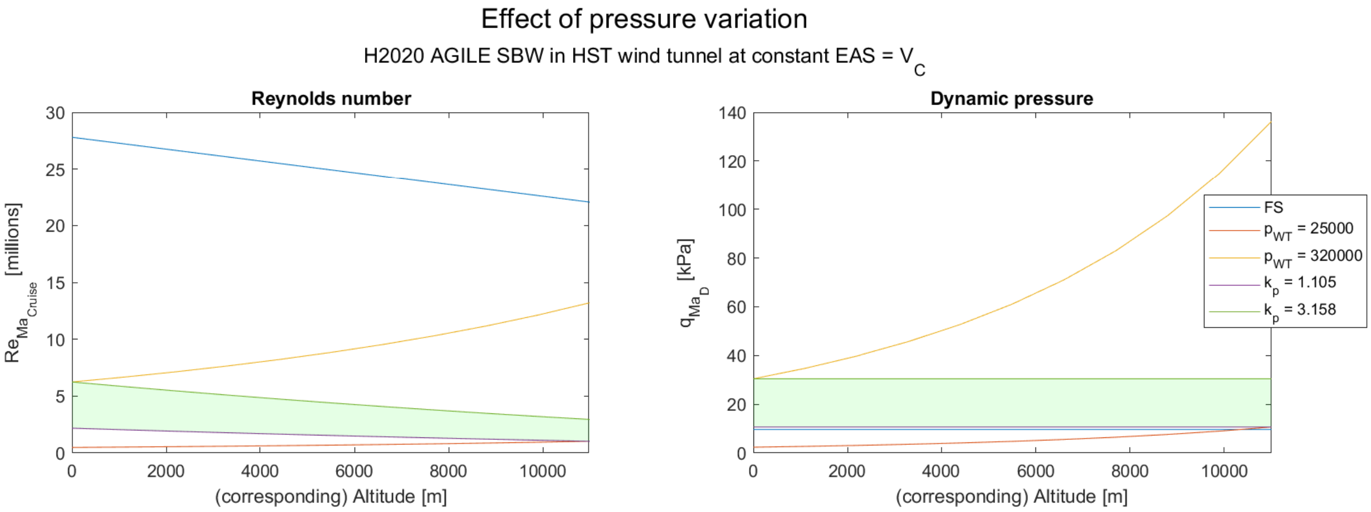

Figure 4.5: Possible Reynolds number and dynamic pressure ranges for AGILE wing in HST

As the dynamic pressure scaling parameter is the same as the pressure scaling parameter (for k_{M_a} = 1, equation (2.12)), it can be seen from figure 4.5 that the dynamic pressure in the wind tunnel is higher than for the full-scale wing, even if the lowest possible k_p is chosen[2]. A high dynamic pressure results in higher forces and thus higher limit loads that the wind tunnel model should be able to handle. The difference between the dynamic pressures when choosing the highest and lowest wind tunnel pressure may seem small in figure 4.5, but the difference is a factor 3, meaning the wind tunnel needs to be a factor 3 stronger when using the higher pressure scaling factor. When only considering this, it may seem beneficial to choose the lowest constant k_p possible as it would be easier to meet strength requirements. However, when doing so the Reynolds number is further off than it would be when choosing the highest possible constant k_p value.

While the difference between highest and lowest possible Reynolds numbers is also approximately a factor 3, this difference does have another meaning, as for this variable the difference between the full and small scale model is of importance. This difference varies from a factor 5 for the highest pressure at a corresponding altitude at sea level to a factor 20 at the lowest pressure at a corresponding altitude of 11000m. While a small difference in Reynolds number will not have a large effect on the aerodynamics of the wing, an order of magnitude can have an effect. The next section explores the effects of a Reynolds number change of factor 10 by CFD analysis to assess the applicability of the k_p range.

4.2. CFD Results

As mentioned, it is impossible to obtain the same Reynolds number in the wind tunnel as in full-scale flight[3]. This gives concern to the accuracy of the wind tunnel results as improper Reynolds number scaling can result in different aerodynamic resultants. Especially when the angles of attack get higher and separation occurs, a different Reynolds number can have a large effect on the forces on the wing. For this reason, CFD results of the SBW have been compared for the full-scale wing in cruise condition and for the same wing in a flow for which the Reynolds number was changed with a factor 10, which falls within the valid range as seen in figure 4.5. Only the flow conditions were changed. The actual size of the wing was unchanged in order to use the same grid. The Mach number was the same for both cases at M=0.78. The CFD analysis incorporates aeroelastic effects and uses the same structural model for both Reynolds numbers.

For the wing at an angle of attack of 0 degrees, figure 4.6 shows that the pressure distribution over the wing is indeed nearly the same for the top and bottom figure. A small difference is seen in the upwards displacement (delta Z) of the wing's tip, but the difference can be considered insignificant.

---

[2] Since the EAS is set as a constant value the dynamic pressure indeed does not change with (corresponding) altitude.
[3] for the H2020 AGILE SBW in the HST wind tunnel

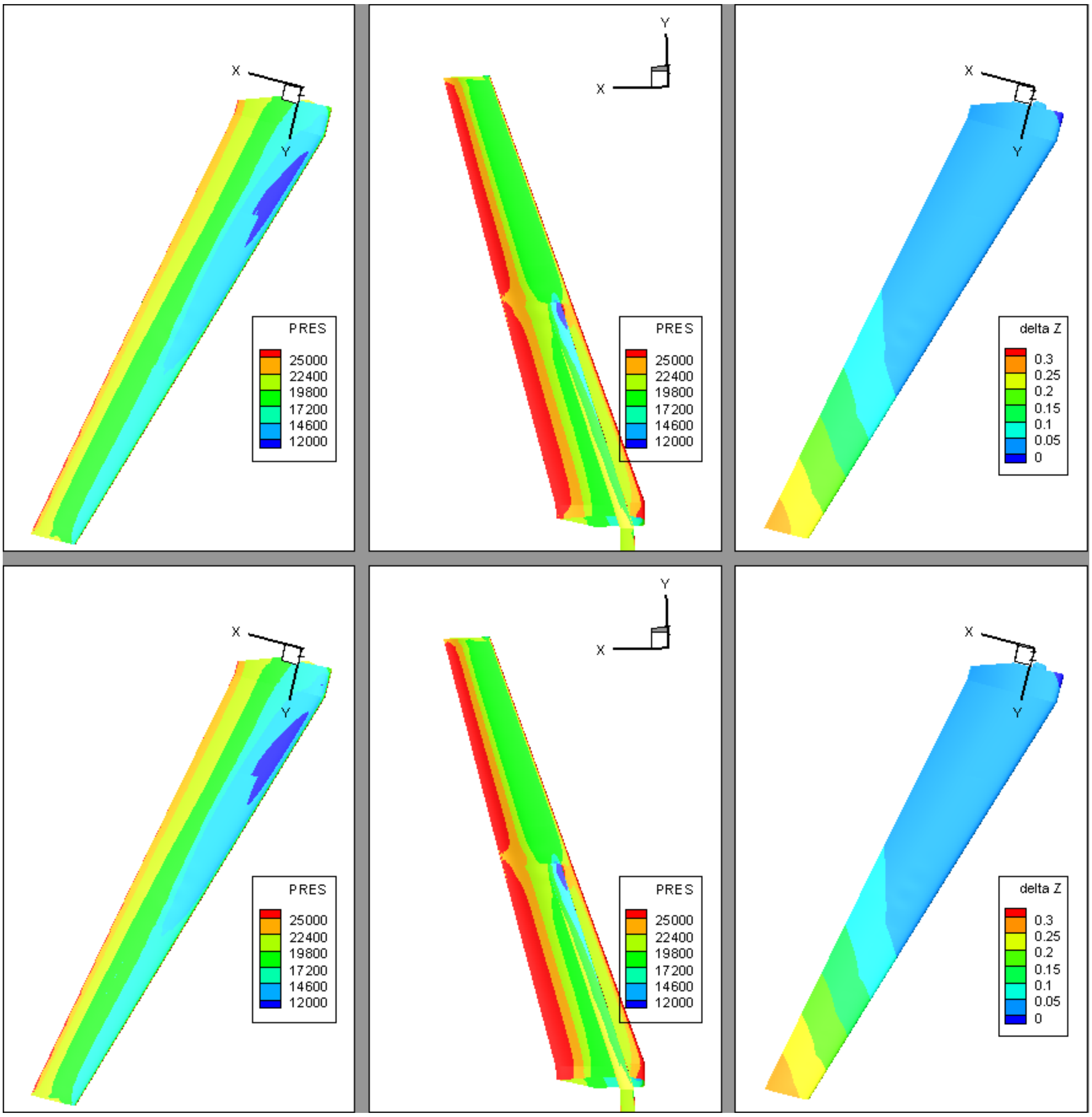

Figure 4.6: CFD results for $\alpha = 0^{\circ}$,
top: lowered Reynolds number, bottom: full-scale results,
l: pressure over top surface (Pa), m: pressure over lower surface (Pa), r: deformation in Z (m)

Similar results can be seen for the -2.5, 2.5 and 5 degree angle of attack CFD results, which can be found in appendix A, where only minor differences can be seen in the pressure and deformation plots.

What can be seen in figure 4.7 is that for an angle of attack of 7.5 degrees there is a substantial difference between the lower (wind tunnel) and higher (full-scale) Reynolds number. The deformation for the lower Reynolds number is lower at the tip than in the higher Reynolds number flow. This can be seen as well in the pressure plot, which indeed shows a lower pressure over the top surface for the higher Reynolds number, thus indicating more lift and deformation.

As mentioned in the previous section, the largest factor the Reynolds number could differ with would be ~20 when the lowest k_p is chosen. This larger difference was not analyzed with CFD but it is to be expected that a similar result will be found, as the order of magnitude of the Reynolds number does not change much further. Thus, it is expected that lower angles of attack will show good similarity, while higher angles of attack will show differences.

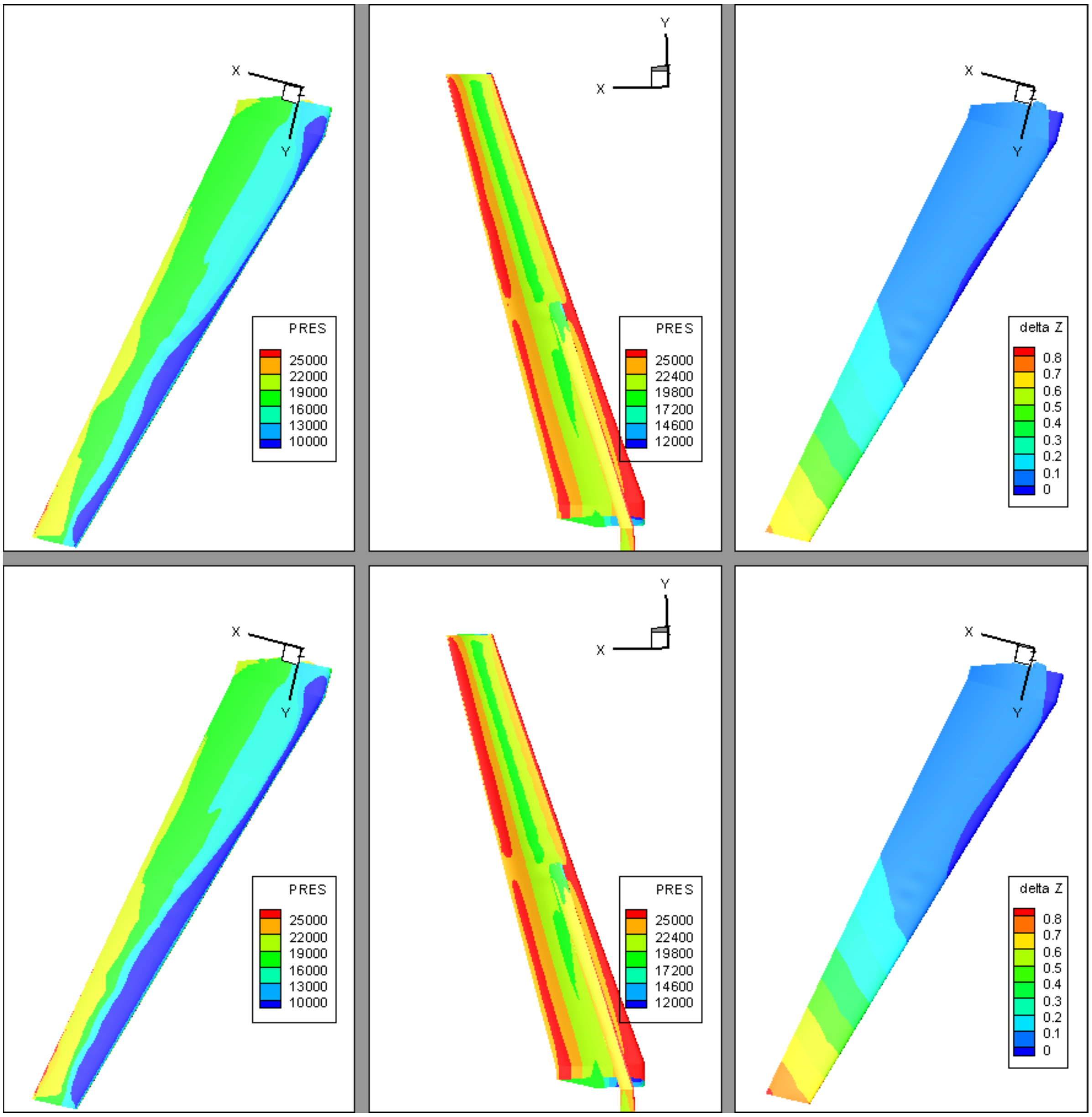

Figure 4.7: CFD results for $\alpha = 7.5°$,
top: lowered Reynolds number, bottom: full-scale results,
l: pressure over top surface (Pa), m: pressure over lower surface (Pa), r: deformation in Z (m)

4.3. Discussion

As is shown in the previous sections, the pressure scaling factor depends on the available wind tunnel and the flight conditions that are to be simulated. For this research k_p should lie between 1.2 and 3.8 if the wind tunnel model of the AGILE SBW is to be tested in the HST. A lower value would be beneficial in terms of strength requirements, whereas a higher value would result in a better Reynolds number similarity.

Section 4.2 showed that if the Reynolds number is changed by a factor 10 that there is no substantial effect for angles of attack from -2.5 to 5 degrees but for the angle of attack of 7.5 a change in the pressure field can be seen, especially in the outer section of the wing, after the strut. This means that wind tunnel tests will show different results than the full-scale version would in flight for higher angles of attack. It is thus not deemed feasible to use the HST for the reference, or similar, wing when angles close to stall are of interest, with these type of flight conditions. Other wind tunnel types could be useful in those cases, for example, cryogenic tunnels may be able to match both Reynolds and Mach conditions. When only testing lower angles of attack the changes to the pressure distribution and deformations on the wing are small and Mach and interference effects can be verified in the wind tunnel.

For the tests intended in this research; assessing efficiency in cruise and climb conditions; the lower Reynolds number is sufficient. Since the CFD results showed that Reynolds numbers do have an effect but the effects are small for lower angles of attack, it was decided that the Reynolds number effects are not of interest for the purpose of this thesis. This assumption is however only valid for angles of attack of ~5 degrees and lower. This assumes that when using the lower k_p, and thus a larger difference in the Reynolds number (up to a factor 20), it would still not have a significant effect at 5 degrees. This should be further analyzed in future research and may depend on the exact configuration that is to be tested.

Choosing the lowest possible k_p value decreases the strength requirements on the wing, as it decreases the force on the wing that causes the deformations. A higher value would allow more design freedom for a composite model's layup as there will be more layers. These layers should, however, fit inside the geometry of the wing. It is therefore left free in the design and optimization phase to vary this value between 1.2 and 3.8. Pressure scaling parameter values of 1.25, 2.5, and 3.75 are compared in this thesis.

5

Full-Scale Static Aeroelastic Analysis

Before starting to design a composite wind tunnel model, it is necessary to determine the full-scale aeroelastic results, as it will be important for the wind tunnel model to match these deformations in scaled flight conditions. This chapter discusses the process of computing the static aeroelastic results and ends with the results found that can be used in the objective function for the optimization later on.

This full-scale aeroelastic analysis is performed on the two reference aircraft, the H2020 AGILE SBW and its cantilever version. Figure 5.1 show these two reference aircraft, it can be seen that the main wing of the SBW is the same as the cantilever wing.

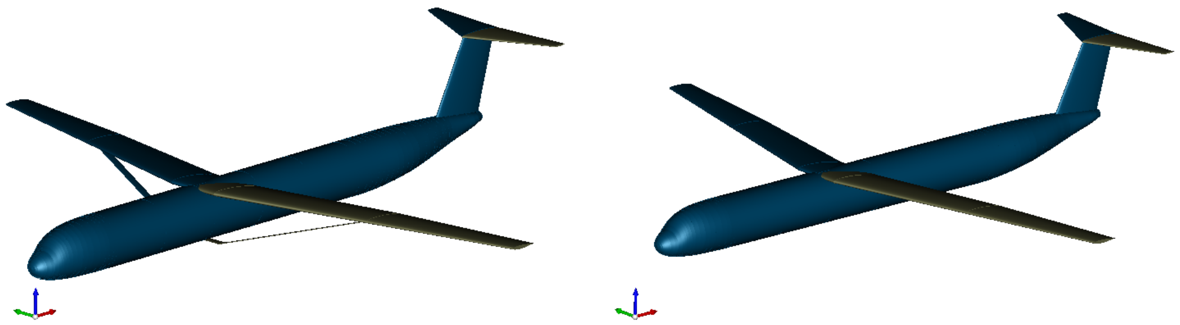
(a) Strut-braced wing

(b) Cantilever wing

Figure 5.1: Reference aircraft

5.1. Method

A static aeroelastic analysis was performed to retrieve the deformations of the wing and the forces acting on it. A structural model was created in Nastran on which a modal analysis was done. Next, the eigenmodes and frequencies together with the structural model itself were supplied to Zaero, a higher fidelity panel method solver for aeroelastic analysis. The next section will briefly discuss the layout of this original structural (NASTRAN) model, followed by a brief section on the aerodynamic (Zaero) model. Note that although the model shown in this section is for the SBW, the same steps were taken of the cantilever wing, unless otherwise specified.

The flowchart in figure 5.2 shows the steps taken in the MATLAB program that was written to perform these actions. The CPACS model and the str.xyz (locations used in the supplied matrices), str.K (stiffness matrix) and str.M (mass matrix) values were initially provided as well as part of the rewrite-

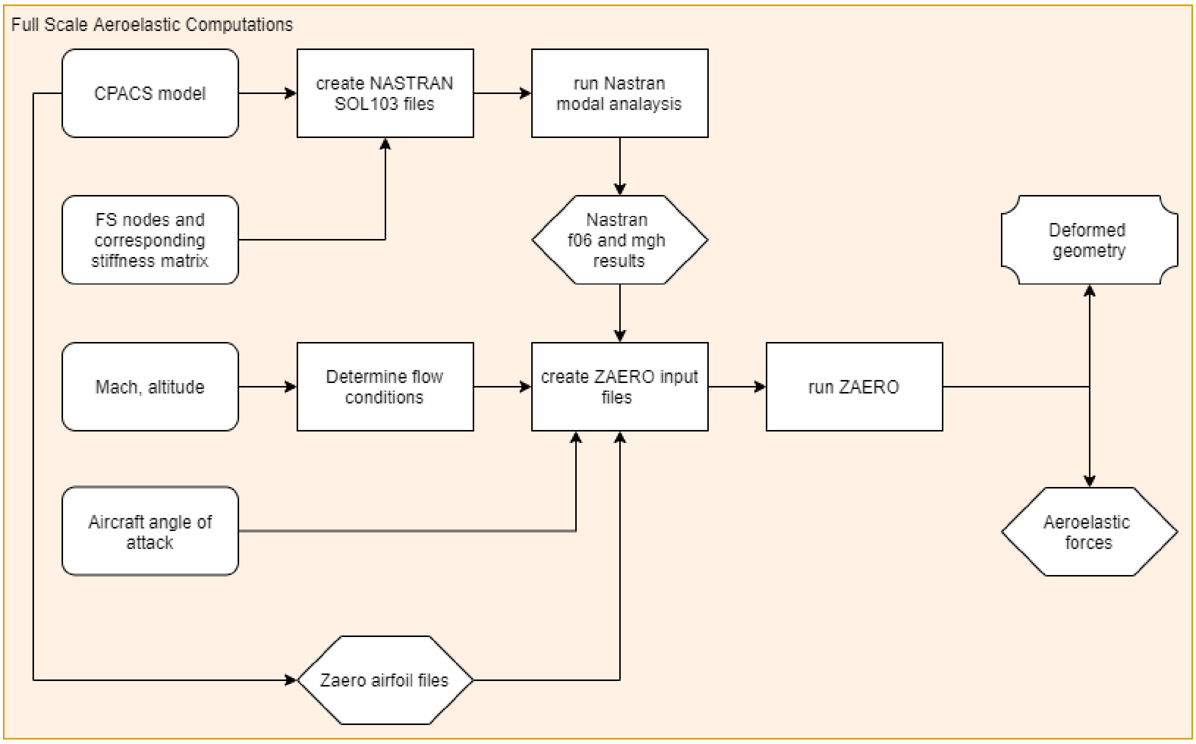

Figure 5.2: Steps taken in the full-scale aeroelastic computations. Excerpt of program diagrams found in appendix B

MODEL function which defines part of the original grid locations [1]. When considering a new wing in future research similar inputs would be required but may have to be slightly rewritten to match the used structure. The stiffness and mass matrices can be extracted from a FEM solver and be saved in the required parameters.

The Mach and altitude can be chosen from the test envelope as discussed in the previous chapter. The input shown in the rest of this chapter was chosen at cruise and an angle of attack of 5 and is shown as an example. This resulted in files that contain the deformed shape and the forces that act on the wing for the chosen case.

5.1.1. Structural Model

A beam model of the full-scale wing was already present from the H2020 AGILE SBW research project that was chosen as a research model. The model contained stiffness and mass matrices and consisted of 24 beam elements for the wing and five elements for the strut. No information about the exact structural elements and material were present but these matrices contained the information needed for the aeroelastic sum. For the cantilever wing, the same elements were used minus the strut elements. [2]

The defined structural grid runs through the front spar of the reference wing[3]. The mass and stiffness matrices defined between these points define the structural behavior of the model. To transfer loads and to model the rotation of the structural model to the aerodynamic model, two points per airfoil are defined at the leading and trailing edge. A rigid element is placed between these two points as cross-sections were assumed very stiff. Figure 5.3 shows the full-scale Nastran model. The green points are the defined nodes, whereas the red points and lines are the rigid elements. It can be seen that no rigid elements are present at the roots, which is due to the presence of DOF-constraints at those positions.

---

[1] The chordwise spar locations were defined hardcoded in a (provided) MATLAB script as not all was defined directly in the CPACS model. For this reason, the rewrite model step is necessary for this specific chosen reference model

[2] The stiffness and mass matrices of the cantilever wing were developed for this thesis, they are not optimized and are a simple 3-part beam model with stiffness properties such that it had a roughly 10% tip displacement at an angle of attack of 5 degrees.

[3] That this location is the front spar can not be taken from the model but is known from the reference project

The wing root is constrained in all DOFs. For the SBW the strut root is constrained in translation but left free to rotate. This models the strut-braced wing as it attached to a wind tunnel wall with a rigid connection for the main wing but as a ball-joint at the strut root, for the cantilever only a rigid connection at the root is present. These wind tunnel wall connections are modeled in Nastran with SPC's (Single-Point Constraint) at the nodes that are located at the root. For the main wing root this SPC locks translation and rotation in all directions, for the strut root only the translations are locked and the rotations are free, as if there was a ball-joint at that position. For the full-scale strut-braced wing the mass and stiffness matrices define the connection between the upper strut node and the 13th wing node (which is where the wing-strut joint is located). Although non-deducible from the matrices, this is known to be a rigid connection in the original model [66].

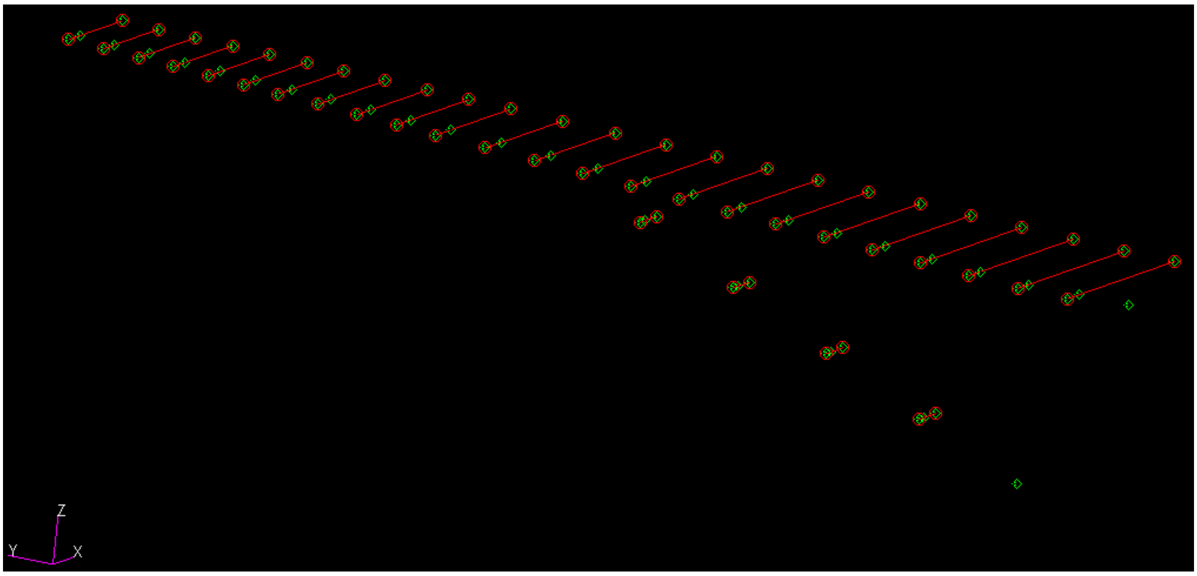

Figure 5.3: Full-scale Nastran model. Green shows the nodes. The green nodes that are not circled in red are the ones between which the mass and stiffness matrices are defined. Red lines show the rigid elements and the red circles show the nodes that were used to define these elements.

After defining the structural model, NASTRAN SOL103 is run, which is a real eigenvalue analysis solver. The natural frequencies and the corresponding mode shapes are provided as solutions to the problem which can be used for aeroelastic analysis. The theory used by NASTRAN can be found in their reference manuals [67].

5.1.2. Aerodynamic model

The aerodynamic model consists of airfoils that have been defined at the same span-wise locations as the original points. The airfoils are taken from the definitions in the CPACS model. Additionally, the flow conditions are defined, the Mach number, dynamic pressure, and angle of attack have to be supplied. Together with the structural model and the computed modes, a static aeroelastic solution can be found. See section 2.2.1.1 and the Zaero user manual [30], for a more detailed description of the theories used in the program. Figure 5.4 shows the aerodynamic model of the strut braced wing, the structural model grid is indicated by the red dots.

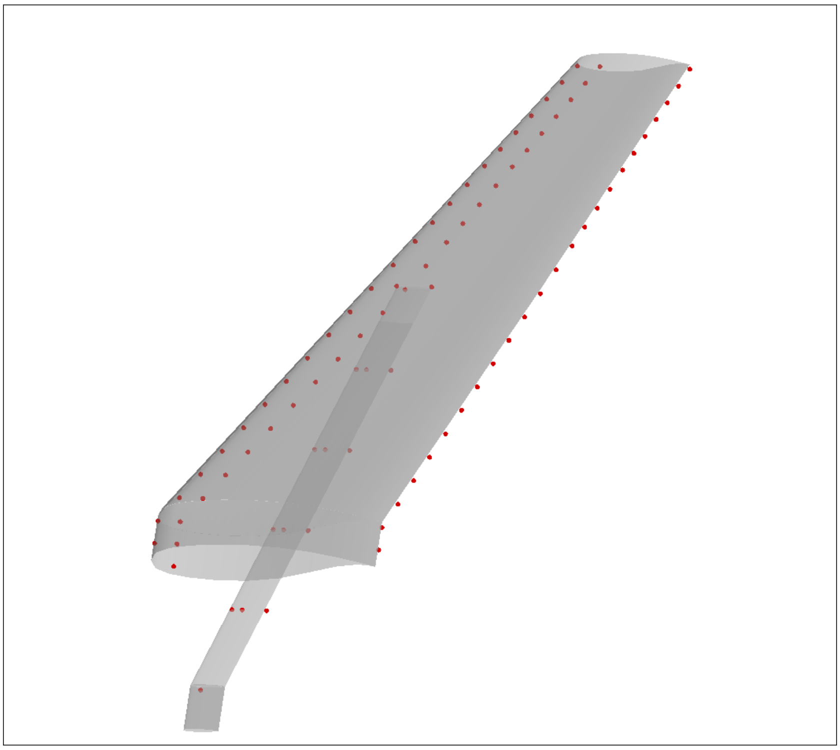

Figure 5.4: Full-scale Zaero model. The aerodynamic shape is shown, the red dots indicate the structural model as shown in figure 5.3

5.2. Results and Wind Tunnel Model Objectives

As mentioned in the research plan two main results are needed from the full-scale aeroelastic analysis, namely the deformed shape and the forces acting on the wing which resulted in this deformation. The analysis was performed for multiple angles of attack but the results in this section show the results for an angle of attack of 5 degrees. This angle was chosen since this is the highest angle that showed to give valid results in chapter 4. Additionally, higher angles result in higher deformations and forces and thus are easier viewed in figures.

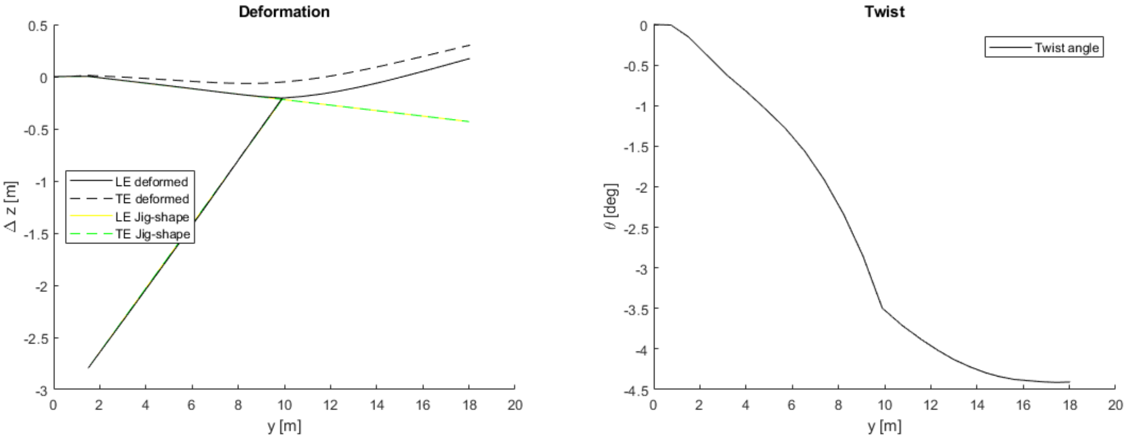

(a) Deformation

(b) Twist

Figure 5.5: Aeroelastic deformation and twist of full-scale strut-braced wing model in cruise at α = 5 degrees

Figure 5.5a show the deformation of the strut-braced wing. It shows the leading edge (solid line) and trailing edge (dashed line) while deformed and undeformed. It can be seen that there is no twist for the undeformed wing but there is negative dihedral. What can be seen is that the deformation of the full-scale wing results in a nose-down twist, which is beneficial for stability reasons and it can be seen that the wing barely bends up until the strut connection while it is already twisting in the inner section. Figure 5.5b shows the twist angle along the span for the deformed result.

Figure 5.6 shows the deformation of the wing from Zaero's aeroelastic output directly, the lower, blue, surface is the undeformed wing. In these it can also clearly be seen that there is nose down twist for the whole wing and that the upwards deformation of the wing starts to become stronger from the strut-wing-joint outwards.

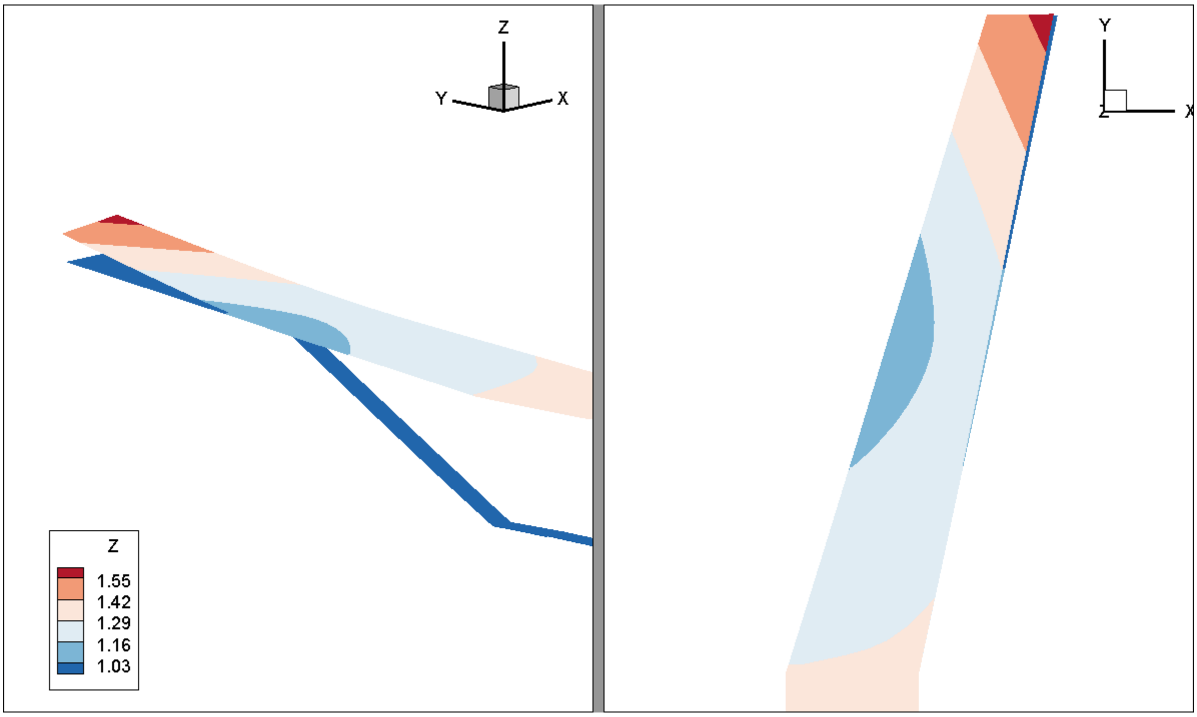

Figure 5.6: Deformation of full-scale strut-braced wing model in cruise at α = 5 degrees

Figure 5.7 shows the pressure distribution over the wing and strut from these results. These results can be used at the end of this thesis to evaluate how well the found designs match in terms of aeroelastic results.

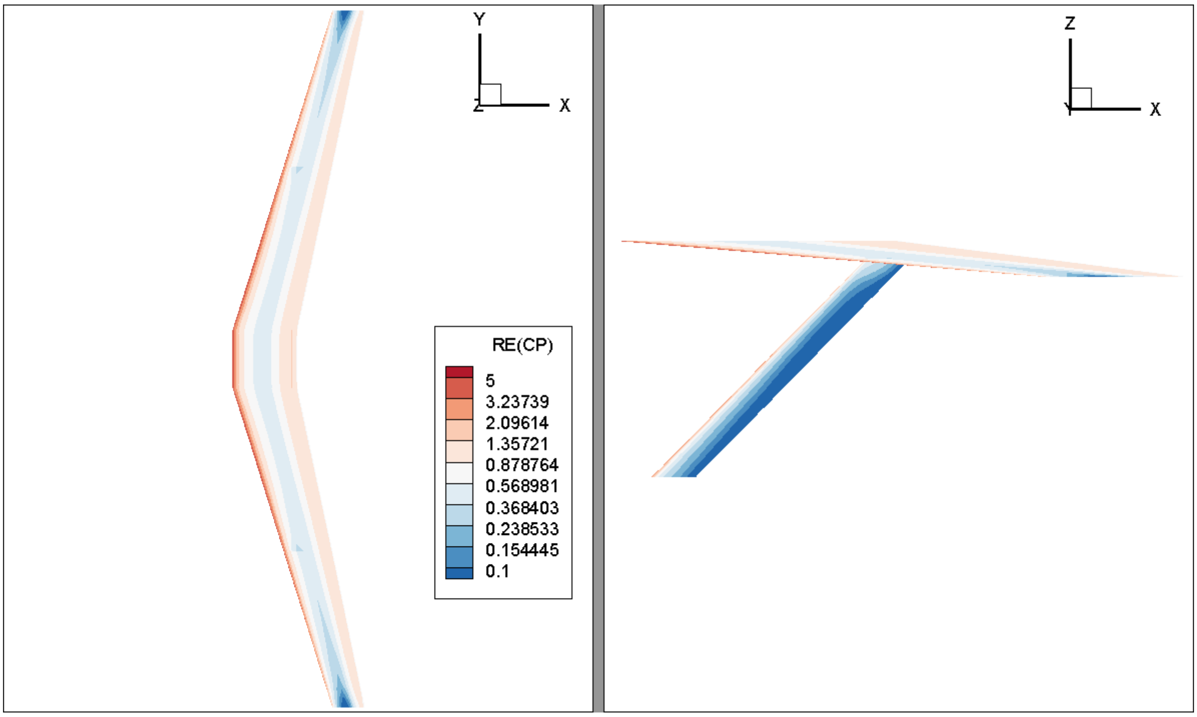

Figure 5.7: Aeroelastic pressure coefficients of full-scale strut-braced wing model in cruise at α = 5 degrees

The same analysis was done for the cantilever wing, these results are shown in figures 5.8 to 5.10. What is notable from figure 5.8, is that the twist clearly shows that the full-scale model was modeled as a beam with 3 different cross-sectional stiffnesses. Again, the cantilever wing used in this thesis does not come from a full-scale optimized model but was roughly designed.

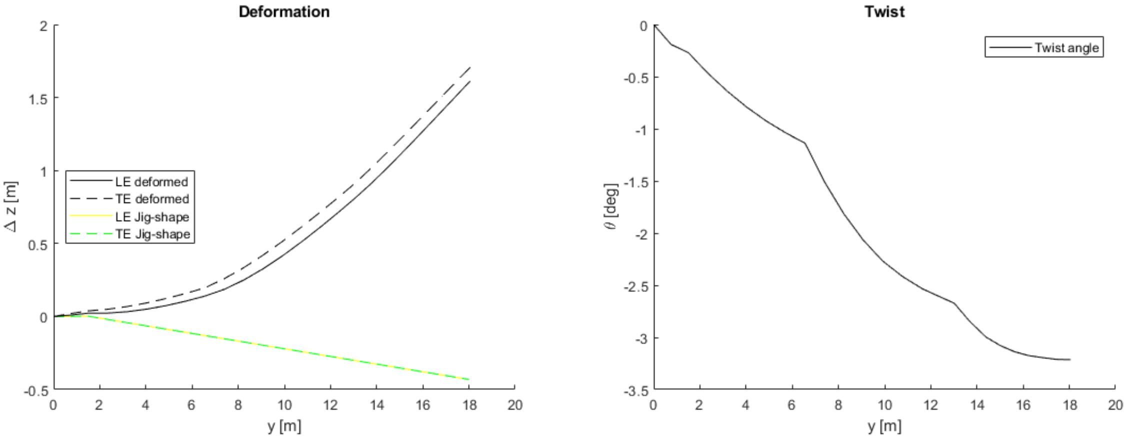

(a) Deformation

(b) Twist

Figure 5.8: Aeroelastic deformation and twist of full-scale cantilever wing model in cruise at α = 5 degrees

The deformation found directly from Zaero's aeroelastic results are shown for the cantilever wing in figure 5.9. The pressure coefficient results are shown in figure 5.10.

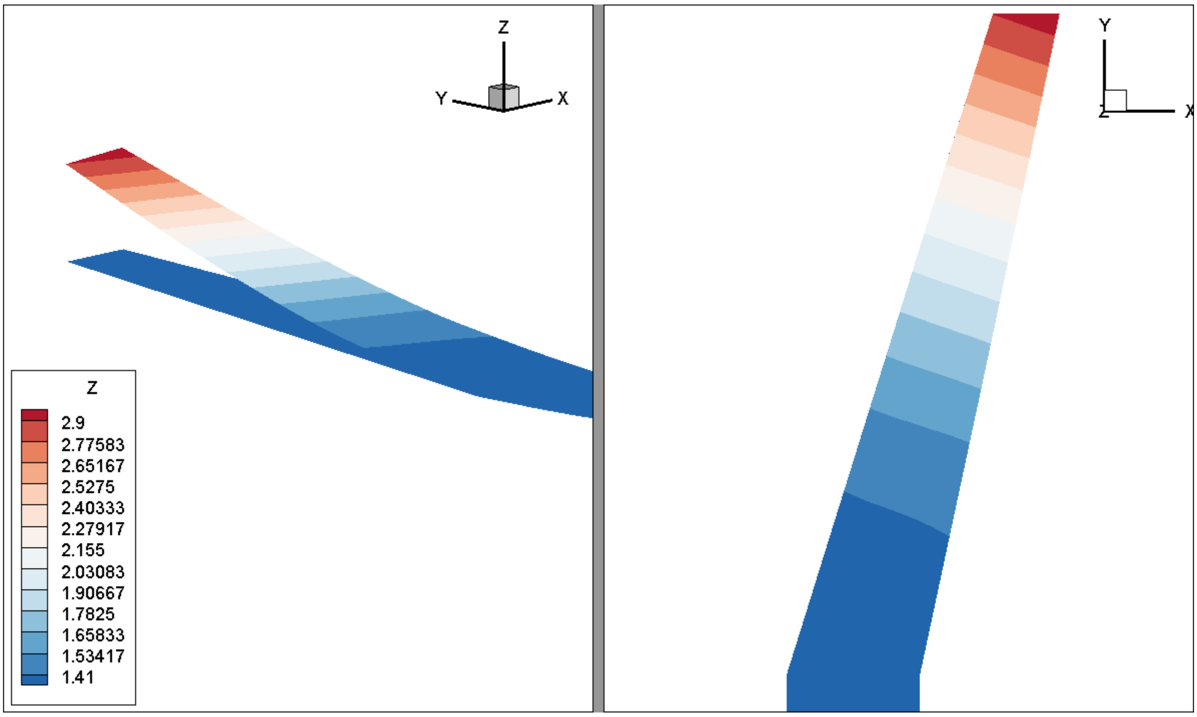

Figure 5.9: Deformation of full-scale cantilever wing model in cruise at α = 5 degrees

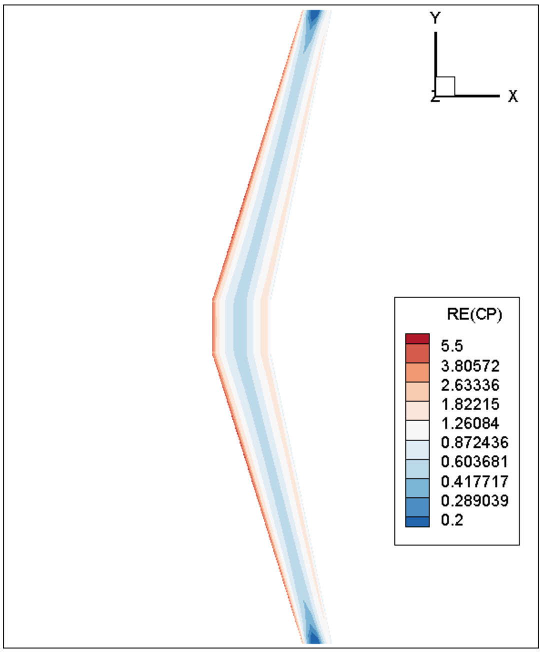

Figure 5.10: Aeroelastic pressure coefficients of full-scale cantilever wing model in cruise at α = 5 degrees

5.2.1. Scaling of Full-Scale Results

The results shown above are for the full-scale wings. But, fortunately, the literature review showed that both the geometry (thus the deformations) and the forces can be scaled by simple parameters. Equation (4.2) and equation (2.17) can be used to scale the results for the smaller scale wind tunnel model. The first of these equations already shows the geometric scaling factor (k_b) to be 0.07778. The force factor (k_F) is determined using the pressure scaling factor(k_p), the Mach scaling factor (k_{M_a}, which is 1 for similarity) and k_b. As discussed in the previous chapter, the pressure scaling factor ranges from 1.2 to 3.8. A higher pressure scaling factor causes a thicker laminate as the forces will be stronger, creating more design freedom for the layup. However, a too high force will make it hard for the wing to adhere to the strength requirements while not becoming too thick of a laminate, such that it does no longer fit in the wing. Equation (5.1) shows the resulting range of values for the force scaling factor.

$$\begin{aligned} k_F &= k_p k_{M_a} k_b^2 \\ k_{F_{min}} &= 1.2 \cdot 1 \cdot 0.07778^2 = 0.007259 \\ k_{F_{max}} &= 3.8 \cdot 1 \cdot 0.07778^2 = 0.022988 \end{aligned} \tag{5.1}$$

The wing deformations were mentioned in the research plan as the objective of the optimization framework. The deformed wing's x,y, and z coordinates of the leading and trailing edge define this objective. The results found by Zaero are scaled with a factor k_b to new x,y,z coordinates. A necessity for the optimization problem will be that the used points match exactly with these points so that they can be compared properly.

The force file that Zaero creates is in the format of Nastran's input files. This is a text file that contains forces in x, y, and z direction at each of the defined grid points. These forces are scaled with the chosen factor k_F for use by the static finite element analysis in the optimization framework, as was explained in the research plan.

5.2.2. Comparison Zaero and Nastran Results

Since the internal computations of Zaero and Nastran are slightly different, the found result was compared to a Nastran result using the output forces from Zaero and the original structural model. This is to confirm that both programs provide the same results and optimization using the static FEM solver is possible.

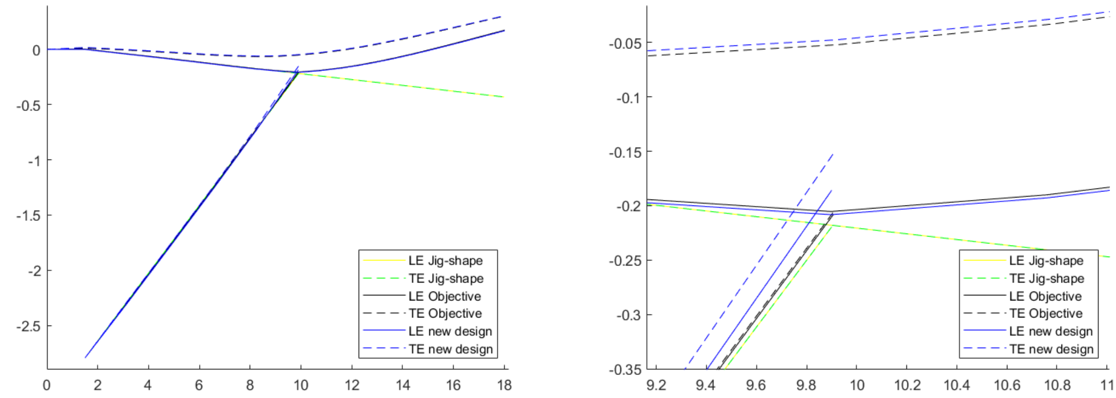

(a) Strut-braced wing

(b) Zoomed in on strut-wing-joint

Figure 5.11: Comparison of Zaero aeroelastic results and Nastran results

Figures 5.11a and 5.11b show the leading-edge and trailing-edge lines of the wing for the jig-shape, Zaero results and the Nastran results of the SBW. From figure 5.11a it seems a perfect match but from figure 5.11b it can be seen that there is a slight difference for the wing and a larger difference for the strut at the joint. Zaero sees the wing and strut as separate surfaces and therefore seems to not correctly model the twist of the strut at the joint. For the cantilever wing, the difference is small overall.

5.3. Aerodynamic Verification

To check whether Zaero gives an accurate prediction of the forces on the wing the results are compared to CFD results, which are discussed in more detail in section 4.2. Zaero gives a force file output that can directly be used in NASTRAN as input for the static structural sum, whereas with the found CFD results this is not directly possible. Using the Zaero results is also computationally less expensive than including CFD results.

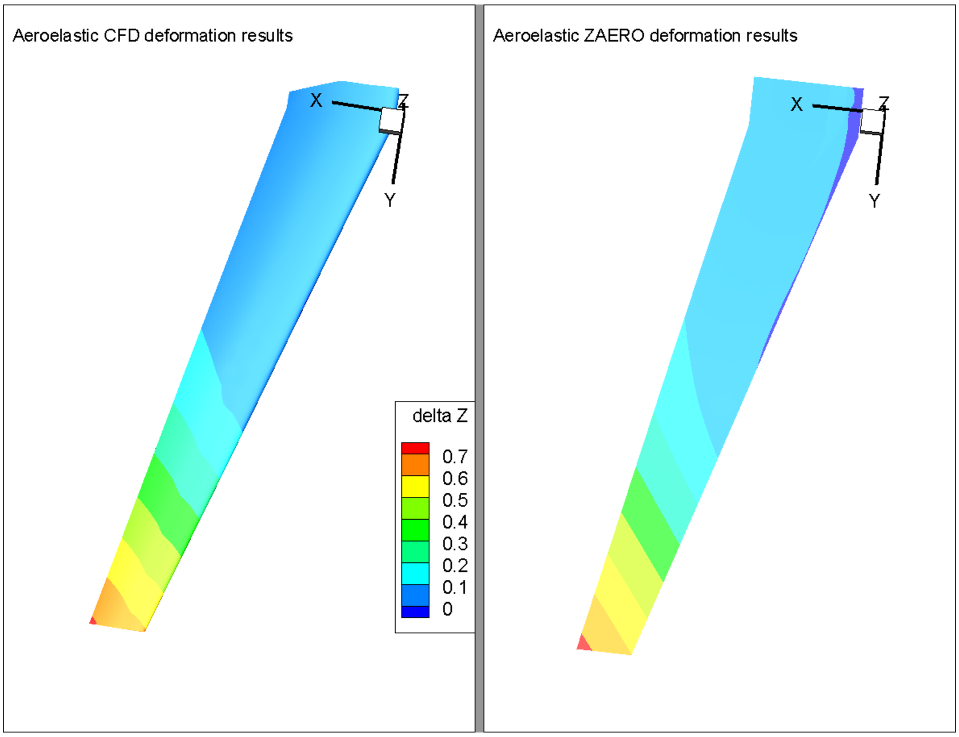

Figure 5.12: Comparison between CFD (left) and Zaero (right) deformation results

The aeroelastic CFD results use the same structural model, in which mass and stiffness matrices were supplied. Figure 5.12 shows the deformation results after a static aeroelastic analysis performed with both the higher fidelity panel method and with CFD. While the CFD results are known to be more accurate to predict the aerodynamics, it can be seen that both methods predict a similar deformation and thus lift force. This thus shows that using Zaero's force output as an input for the structural deformations should give accurate results when it comes to static aeroelastic behavior.

Unfortunately, the pressure field output given by Zaero and the CFD results do not match and can therefore not easily be compared. However, it is only important that Zaero correctly models the forces that cause the deformations, since the similarity between the two results, as seen in figure 5.12, verifies that the force output can be used for this research. It has to be noted that the actual flow that can be expected during testing would be more similar to that of the CFD results shown in chapter 4 and appendix A.

5.4. Verification of Scaling Parameters and Numerical Effects of Scaling in Zaero

This section covers a verification of what happens to the aeroelastic result when the model is scaled using the parameters found in the literature review. This is useful to verify the found scaling factors and will help identify possible numerical errors induced by Zaero on the aerodynamic forces when scaling. While the optimization will not run Zaero while optimizing, the final results will be verified with an aeroelastic analysis.

This verification cannot be performed directly using the input model, as only the mass and stiffness matrices are supplied and these cannot be scaled directly using the scaling parameters. For this reason, a beam model was created that consisted of bar elements, similar to the original model, with the same grid points and rigid body elements. These bar elements have a definable EI, EA, and GJ, which is what makes it simple to scale them using the found parameters.

The beam model for the full-scale wing consists of an aluminum box that changes cross-sectional dimensions based on the chord length at that span-wise position. This box was modeled such that it would give results comparable to the original wing but does not represent the structural properties of the actual full-scale model. The aerodynamic model is the same. The flow properties are defined with the angle of attack, the dynamic pressure, and the Mach number in the same way as was done in section 5.1.2. These were thus chosen, in this example, as the AGILE wing's cruise values with an angle of attack of 5 degrees.

For the smaller scale model all dimensions (including the material thickness) were scaled with a factor $k_b = 1.4/18$. The Mach number stays the same in both computations as well as the angle of attack. The dynamic pressure scaling in this example is a factor $k_q = 2$ larger for the small scale wing. As seen in equation (2.16) EI is scaled with $k_{EI} = k_p k_{Ma} k_b^4$ (and $k_p = k_q$). Since the moment of inertia I comes from the dimensions and thus provides the k_b^4 part, the Young's modulus E (and the shear modulus G) were scaled with the factor $k_q = 2$.

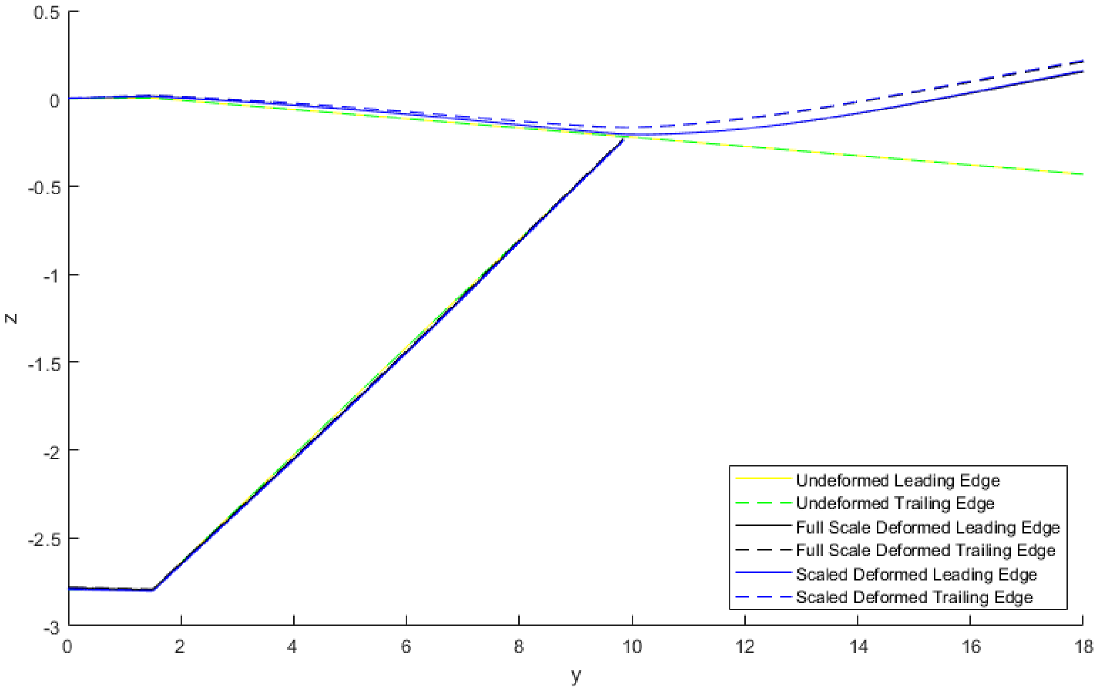

Figure 5.13: Deformed wing, full-scale and scaled result

After scaling the deformation back to full-scale (using k_b), the deformations can be seen in figure 5.13. It can be seen that there is a minor difference between the full-scale and scaled wing deformations but the lines almost lie on top of each other. Figure 5.14 shows that this difference is up to 1.2% of the total deformation, which is a maximum of 7.5mm difference on an 18m semi-span wing, or about 0.58 mm difference on the scaled model.

When considering the difference in forces in figure 5.15, scaled back using $k_F = k_q k_{Ma} k_b^2$ from equation (2.17), it can be seen that the scaled results differ up to ~0.6%. Towards the root the trailing edge difference is larger than the leading edge difference, therefore the nose-down twist is larger for the scaled wing, which indeed led to lower forces. Differences can be due to the fact that the scaled wing becomes rather small and Nastran and Zaero both work with input text files. For this, only 8-digit values are used which may lead to round-off errors and is likely the main cause of these small differences.

From this section, it can be concluded that the stiffness scaling factors derived in the literature review are correct since the deformations are approximately the same after scaling the stiffness of the wing.

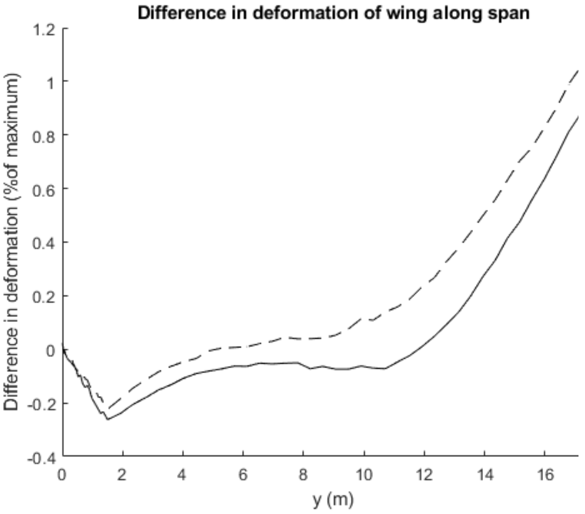

Figure 5.14: Difference in deformation as percentage of maximum deformation

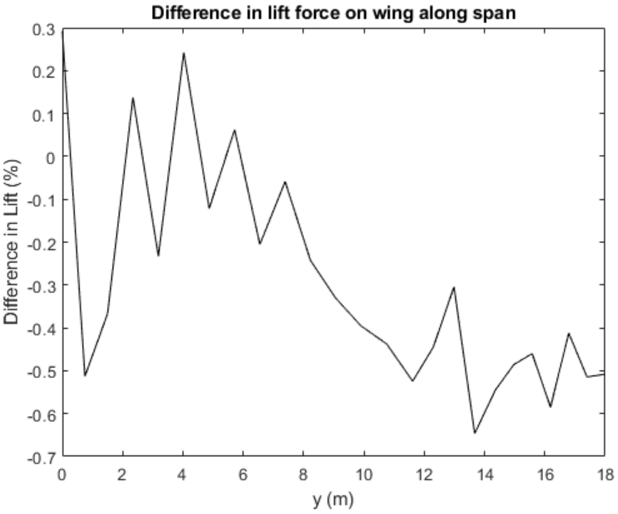

Figure 5.15: Difference in lift force on the wing as percentage of reference lift force

Additionally, there are no major effects of scaling down the wing in the aerodynamic part of the analysis. There will be some inaccuracies when scaling the wing but the differences are small and reasonable for the fidelity level of this research. Errors of ~1% may thus also be expected for the final scaled wing.

6

Wind Tunnel Model Set-up

The previous chapter discussed the models used for the full-scale aeroelastic analyses. These models contained mass and stiffness matrices, but since the aim of this research is to find a composite layup that will match these characteristics, the structural model has to be redefined to match the structural design.

As mentioned in the introduction of this thesis, the scaled model concept considered will be a composite shell with a foam core. Therefore the structural Finite Element Method model also has to be modeled as such. Optimization using other structural model options is outside the scope of this thesis.

The structural analysis is performed in NASTRAN, a FEM solver. NASTRAN takes care of the FEM computations but the structure, boundary conditions, and loads have to be defined properly to get a result. This chapter is split into four sections. Firstly, section 6.1 describes the elements used to model the structure and how the grid is defined, the additional elements that comprise the strut are discussed here as well. Next, the way the structure interacts with the wind tunnel wall is modeled, which is described in section 6.2. In section 6.3 it is shown how the forces from the force file are distributed on the structural model. Finally, section 6.4 discusses the mesh and the accuracy of the model.

6.1. Structural Elements and Grid

The structural model of the wing is constructed of defined grid-points that are connected. For modeling the composite, the outer grid-points are connected using several quadrilateral plate element connections (CQUAD4) with a shell property (PSHELL) that has a material defined using an anisotropic material card (MAT2). These CQUAD4 element connections define panels from four grid points. This is combined with six-sided solid element connections (CHEXA) with a solid property (PSOLID) that defines the foam material properties using an isotropic material card (MAT1). CHEXA element connections connect eight grid points to form a volume. The exact definitions of each mentioned Nastran card can be found in the Nastran documentation [68].

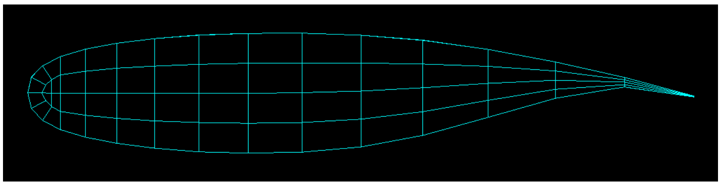

Figure 6.1: Cross-sectional mesh of wing.

Whereas these element connections and the property and material cards take care of defining the properties of the structure, the shape of the structure is defined by the grid points. The cross-sectional mesh is shown in figure 6.1. The airfoil is split into 16 sections, in order to keep the airfoil shape, while not using too many sections for computational reasons. Internally the same cuts are used for the solid, with an exception of the nose, where points were placed such that the shape could be followed roughly. The lines show the edges of the element connections, while each corner is a defined grid point.

Span-wise, the wing is split into the original 24 panels (from the full-scale model), that are further refined by adding additional grid points. Using the original full-scale span-wise node locations allows the comparison of the leading and trailing edge deformations to be more easily compared. Matching up these nodes is not a necessity, but, if they do not match, additional steps would be needed to compare the deformations. Figure 6.2 shows a mesh that has been refined 1 time (i.e., each original span-wise section has been cut in half). Section 6.4 discusses the mesh quality and the convergence of the mesh when refining the mesh further.

The global axis system can also be seen in the bottom-left corner in figure 6.2, x points towards the trailing edge of the wing, y points in the span direction, and z points upwards.

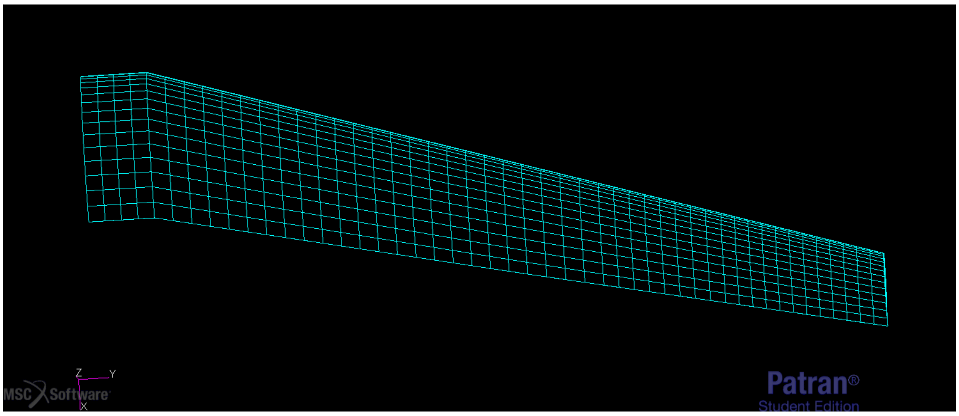

Figure 6.2: Shell mesh of the wing

Strut

For the strut-braced wing, the strut has to be added. The strut can be defined similarly to the wing, using a shell outside and a solid core. In this case, the strut was split into five original sections, which could be refined by splitting it into sections. In figure 6.3 this is shown again where the original y-locations were split once.

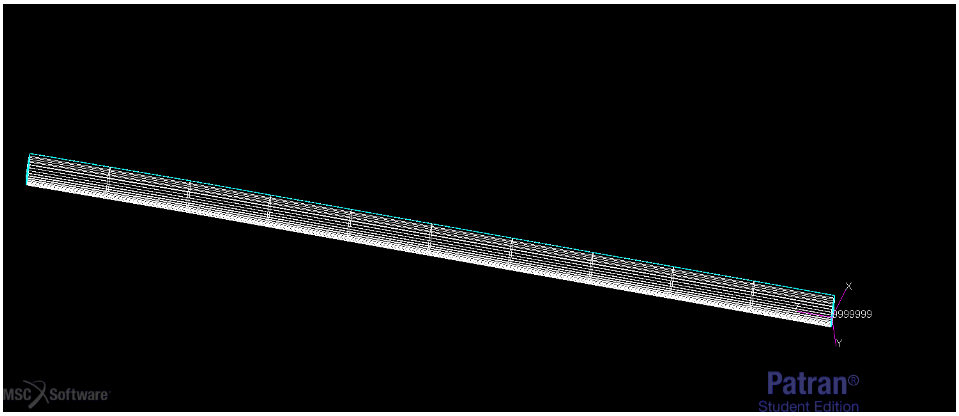

Figure 6.3: Shell mesh of the strut

6.2. Degrees of Freedom

The wind tunnel model would be connected to a wall in the wind tunnel, which would restrict the root from moving in any direction. Therefore, connections have to be defined that represent this case. The wing will be connected at the root with a rigid connection. In Nastran this is modeled as a set of SPC's (Single-Point Constraint) at the root that locks all degrees of freedom for the grid points at y=0. This models the wing as if it were connected to a wall, as it would be in the wind tunnel. This is the same for both the wing-part of the SBW and the cantilever wing.

The strut of the SBW model makes things more complicated and it can be modeled in a number of ways. The full-scale model is known to have a rigid strut-wing-joint and a ball-joint at the root which therefore would make sense for the scaled model also. The root can be modeled using a SPC, locking the translational degrees of freedom at the root. Since for a ball- (or hinge-) joint not all degrees of freedom are locked, it is not possible to again lock all strut grid points at the root, as was done for the wing. Therefore, a single SPC is used for the chosen degrees of freedom, located at the (scaled) original grid point, which is then connected to each other point of the root using a rigid body element (RBE2). This RBE2 can be seen in figure 6.4, the point in the middle is the point that is constrained by the SPC. This RBE2 thus makes sure the entire root twists the same as the rotation point, which is constrained with an SPC.

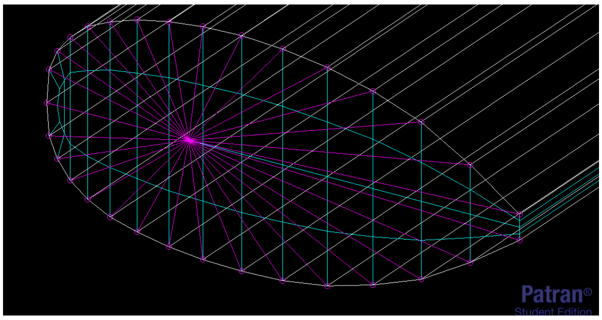

Figure 6.4: RBE2 from the rotation point (middle), to the rest of the airfoil

The wing-strut-joint must be modeled as well. In a real composite wind tunnel model, this would be done using some type of insert into the composite for the wing which attaches to the strut end. In this model, it was chosen to model this using a more singular approach. Thus, using a single point on the strut and wing that are connected using an RBE2, which locks the required degrees of freedom to make sure those degrees of freedom are the same for the wing and strut at that point. Again, this point is then connected to the rest of the structure at that cross-section, separate for wing and strut, using a separate RBE2 locking all degrees of freedom with respect to that singular point, similar to the RBE's that were shown in figure 6.4. This would model that cross-section as being infinitely stiff.

The design and sizing of an insert were deemed outside the scope of this thesis. Inserts are generally made of blocks of metal and are very strong and stiff. Modeling the cross-section at that point as being infinitely stiff therefore should not have a large effect. However, a small effect may be present and a more accurate model of the insert should be used in later stages when the actual wing is built. Figure 6.5 shows an example of such an insert for a Strut-Braced Wing, from an earlier project on the AGILE SBW at the NLR.

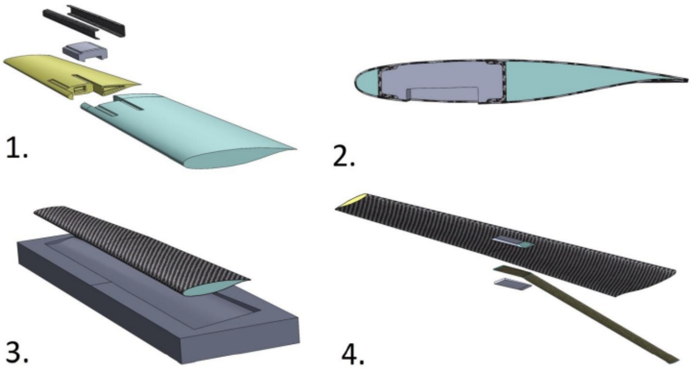

Figure 6.5: Example insert for strut-wing connection [69]

An implication of modeling the joint as a singular point is that there will be local stress concentrations in the FEM model near the joint due to the singularity[1]. This means that stress and strain values found near this singularity may be incorrect. Strength requirements will, therefore, be ignored in the area close to the joint, as it will in a later research stage be replaced by an insert and will have to be re-analyzed. Section 6.4 shows the implications of this singularity and the area that will be excluded.

During testing of the FEM model, it was found that the degrees of freedom used in the full-scale model (rigid joint and rotational freedom at the strut root) do not necessarily give the best matching results. The degrees of freedom can be changed before running an optimization and options can thus be compared. Options that can be considered do not only include a ball joint at the root and a rigid connection at the strut-wing-joint. It also includes using only rigid connections or using a ball joint at the strut-wing-joint while using a rigid connection at the root.

Degree of Freedom Variations

Three options were considered for the way the strut is attached to the wing and the wall and consist of combinations of rigid and ball joints. In this section's figure and table, the joints indicated with 123 are ball joints, whereas 123456 are rigid joints.

Figure 6.6 shows what happens to the RMSD for different designs. This was done by using various laminate thicknesses, for this the lamination parameters were kept the same. The Root Mean Square Deviation (RMSD) indicates how far the found deformation is from the objective (full-scale) deformation. These values show that the first and third option (both with a rigid strut-wing-joint) gave similar function values, while the second option with a ball joint at the strut-wing-joint and a rigid joint at root showed a larger difference. Since only the thickness was varied this however does not show anything about the best possible match once the optimization framework has optimized the laminates.

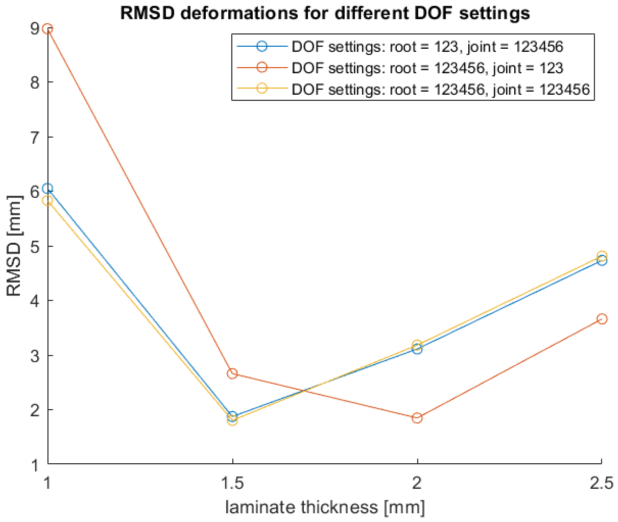

Figure 6.6: RMSD for degree of freedom variations at strut root and strut-wing-joint

Table 6.1 shows the RMSD after optimizing the structure[2]. In the next chapter, the optimization framework will be discussed, but optimization results are shown here to show the differences noticed between the different degree of freedom options after optimization. Within this thesis, the option with two rigid joints will be used as it showed to lead to better optima. Considering each option for different designs could however be beneficial as it may be model-specific which of these options works best.

---

[1] Even if multiple points would be connected at the same span-location this would be true. Without knowledge of the actual insert, a correct region for attachment cannot be defined to prevent this problem

[2] Values shown are for a specific run with similar starting points, but a pattern was noticed in which the model with two rigid joints performed best

Table 6.1: Degree of freedom options for the strut

DOF @ strut root	DOF @ strut-wing-joint	RMSD [mm]
123	123456	1.1353
123456	123	1.3191
123456	123456	1.0159

6.3. Load Distribution

The loads on the model come from the scaled force file of the deformed full-scale model, as was explained in section 5.2.1. They are distributed onto the new wing nodes using interpolation constraint elements (RBE3). These connect the locations at which the forces are applied, which are (scaled) locations from the full-scale model, to the shell of the structure and thus distribute the load. Which points are connected can be seen in figures 6.7a to 6.7c.

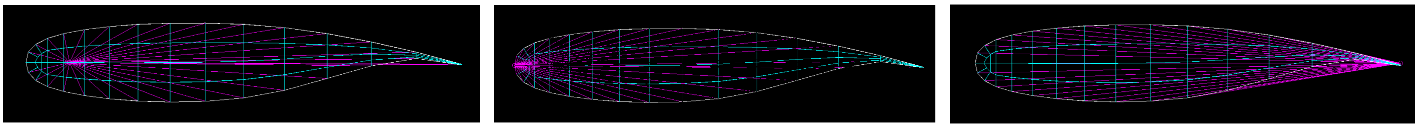

(a) RBE3 from original node location (b) RBE3 from leading edge (c) RBE3 form trailing edge

Figure 6.7: Visualisation of the interpolation constraint elements (RBE3)

6.4. Mesh Sensitivity

The structural grid was defined by splitting the airfoil shapes into sections, interpolating this airfoil shape along the span using the chord, and splitting the mesh span-wise. The number grid points of the airfoil and the number of span-wise splits define how refined the mesh is. A more refined mesh is generally more accurate, but also the shape of the elements matters. This section analyzes the mesh quality and its convergence in terms of displacement and strain results.

In general, for a structural grid, it is important that shapes are as ’square’ as possible (when using 4/8 corner elements), thus having an aspect ratio close to 1. It can be seen from figure 6.1 that near the trailing edge this criteria is not met very well as the elements are much wider than they are high. This is, however, only the case for the foam part of the model, which does not have a large influence on the results; the main reason for the presence of the foam is to prevent buckling and to keep the shape of the airfoil. The span-wise refinement has an influence on the aspect ratio of the shell elements, as a small refinement results in very slender elements near the nose of the airfoils. When refining the span-wise sections this can be reduced. However, when refining this too much the aspect ratio will be too far from 1 in the other direction.

Figure 6.8 shows a mesh quality analysis performed in Patran on the shell elements, which indicates when cell aspect ratios are too large. It can be seen that for figure 6.8b almost the entire wing is blue, indicating an aspect ratio close to 1, while for the coarsest grid the nose of the wing is red, which indicates an aspect ratio higher than 5 (which is deemed of low quality in the standard checks from Patran). The finest grid considered starts to become green near the trailing edge, which indicates an increasing aspect ratio in the other direction. For the strut on the SBW, the elements have to be split twice as often to get similar results in terms of mesh quality.

For the strut-braced wing, the convergence of the tip deformation and the strains for different mesh sizes were analyzed. This analysis was not performed for the wing, as the SBW consists of the same main wing with an additional strut and similar results are expected.

Before checking the convergence of the strain results for different mesh sizes, the area to exclude, to correct for the introduced singularity at the strut-wing-joint, needs to be addressed. As mentioned in section 6.2, an implication of modeling the joint as a singular point is that there will be local stress concentrations in the FEM model near the joint due to the singularity. These concentrations will increase in magnitude when refining the mesh. The area near this point should thus not be included when

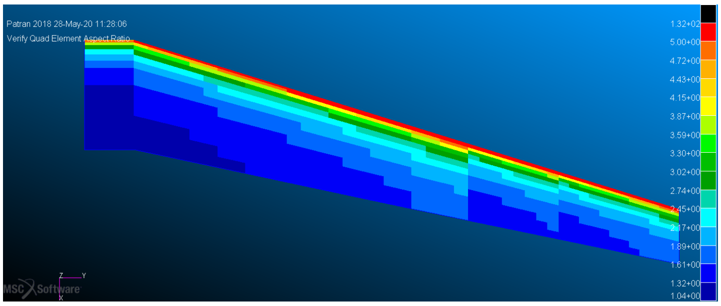

(a) Grid refinement level 1

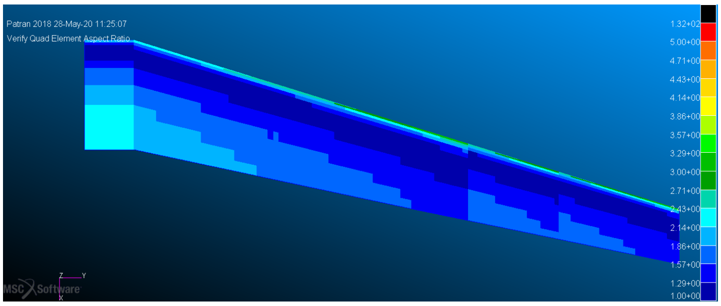

(b) Grid refinement level 4

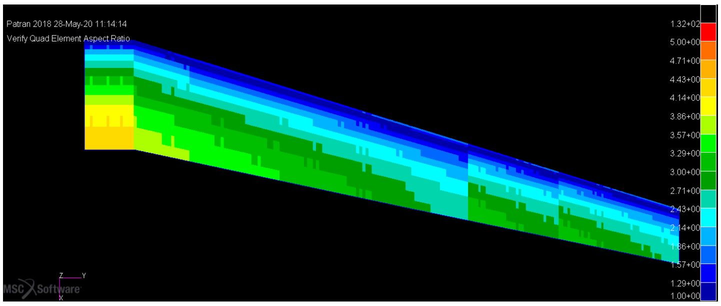

(c) Grid refinement level 8

Figure 6.8: Nastran element check for aspect ratio, blue indicates an aspect ratio close to 1, red indicates an aspect ratio >5

checking the safety factor as the stress concentrations will be higher than can actually be expected at this point when loads would have been properly distributed by an insert. Since these points would later be replaced by an insert the stresses of the composite do not have meaning, therefore skipping this area is deemed valid for this design level. Figure 6.9 shows the strain for a refined and more coarse mesh, where the color ranges are changed to have the same meaning. It can be seen that both results are similar but there is a stronger stress concentration near the strut-wing-joint (more red) for the more refined mesh.

The areas closest to the strut-wing-joint will be excluded, the excluded elements are highlighted in figure 6.10. When excluding this area, the results are more similar between different mesh sizes.

After defining the range to exclude it was checked if coarser and more refined meshes returned comparable deformation and strain results. Figure 6.11a shows the tip displacement for both the leading and trailing edge. While it can be seen that the mesh has not fully converged for the coarsest grid, the difference with the very refined grid is less than 0.1mm, which is smaller than the error experienced due to scaling in section 5.4. This error is therefore deemed acceptable.

Even when removing the area closest to the strut-wing-joint there is a difference between the strains of coarser and finer grids. This difference is substantial with the safety factor decreasing from 4.76 to 4.4. This value, however, quickly starts to converge when the mesh is more refined, as can be seen in

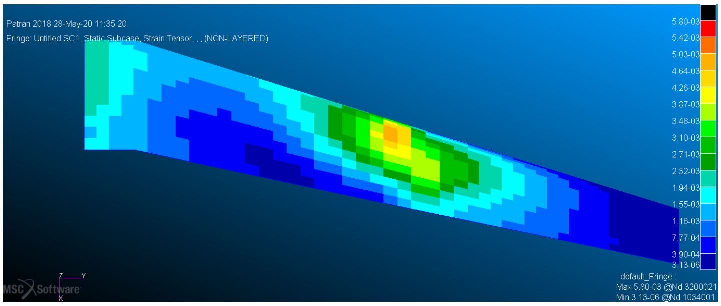

(a) Strains for a coarse mesh

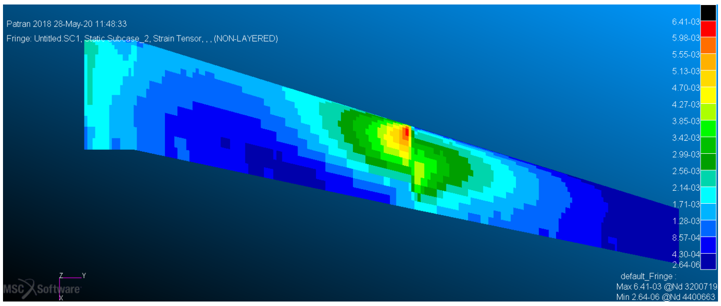

(b) Strains for a refined mesh

Figure 6.9: Visualisation of stress concentrations near strut-wing-joint

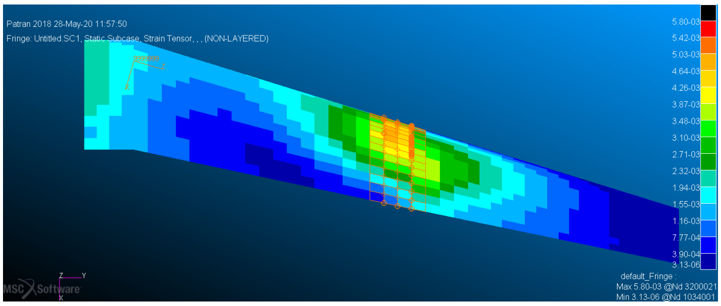

Figure 6.10: Area excluded for strain analysis due to singularities (highlighted)

figure 6.11b. When considering the safety factor that includes the excluded strut-wing-joint area, it can be seen that the strains converge much slower (and keep decreasing at the finest considered grid).

The time needed to perform a function evaluation and the constraint evaluations (for a further matching problem) linearly increases for these mesh refinement steps, as can be seen in figure 6.12. Using a grid refinement level of 3 or 4 thus seems to perform well and consistent in terms of deformation and safety factor (which is directly related to the strains), while not increasing the run time too much. A refinement level of 3 for the main wing and 6 for the strut seems to give results that would be similar to a more refined grid without adding too much additional computation time.

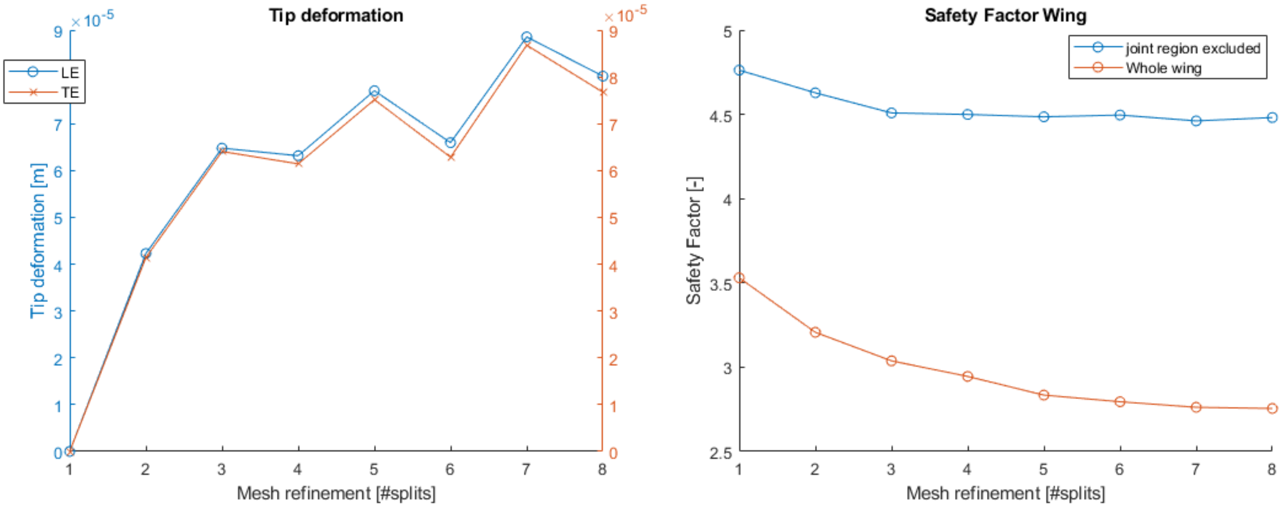

(a) Difference in tip displacement for mesh refinement factors. Blue: Leading edge. Red: Trailing edge

(b) Difference in safety factor for mesh refinement factors

Figure 6.11: Mesh Convergence

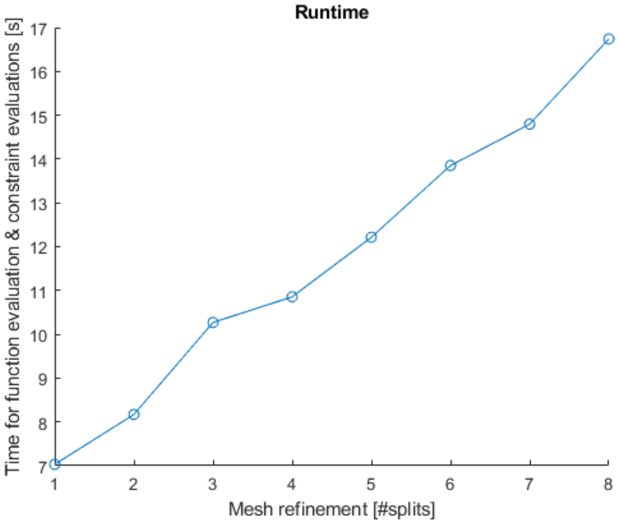

Figure 6.12: Time needed to complete one function evaluation and constraint evaluation

7

Optimization Framework

This chapter describes the optimization process to optimize the material properties of the model. As described in the research plan, the overall optimization will be a multi-step optimization. First, the optimal lamination parameters are found, which are then converted into a stacking sequence. This is done because continuous optimization is generally computationally much less expensive than discrete optimizers. As a single function evaluation takes multiple seconds (figure 6.12) reducing computational efforts is beneficial.

Section 7.1 describes the optimization problem for the lamination parameter optimization. The optimization routine of the lamination parameter optimization is described in section 7.2 and discusses the mathematical process of the optimization. Since the last step in the optimization process, the stacking sequence retrieval, is handled by an open-source genetic algorithm, this will only briefly be discussed in section 7.3.

7.1. Lamination Parameter Space Optimization

The optimization's objective is to find the lamination parameters and laminate thicknesses which form a wind tunnel model best capable of matching the deformations of the full-scale wing under load. Equation (7.1) shows the general optimization problem, where the function $f(\mathbf{x})$ is minimized for variables x such that the nonlinear inequality constraint values, $\mathbf{c}$, are smaller than zero within the bounds $\mathbf{lb}$ and $\mathbf{ub}$.

$$\min_{\mathbf{x}} \ f(\mathbf{x}) \qquad \text{such that:} \begin{cases} c(\mathbf{x}) \leq 0 \\ lb \leq \mathbf{x} \leq ub \end{cases} \tag{7.1}$$

where:

$$
\begin{aligned}
f(\mathbf{x}) &= \text{RMSD}(\text{deformations}(\mathbf{x})) \\
\Rightarrow f(\mathbf{x}) &= \sqrt{\frac{\sum(\text{deformations}(\mathbf{x}) - \text{deformations}_{\text{optimal}})^2}{\#\text{sections}}}
\end{aligned}
\tag{7.2}
$$

$$
\mathbf{x} = \begin{array}{l}
[(\xi_{1,2,3}^{[A,D]})_{[1:\#\text{sections}_{\text{wing}}]}, \cdots \\
\text{t}_{[1:\#\text{sections}_{\text{wing}}]}, \cdots \\
(\xi_{1,2,3}^{[A,D]})_{[1:\#\text{sections}_{\text{strut}}]}, \cdots \\
\text{t}_{[1:\#\text{sections}_{\text{strut}}]} \qquad\qquad]
\end{array}
\tag{7.3}
$$

$$
\mathbf{c} \leq 0 \Longrightarrow \begin{bmatrix}
\text{equation (2.33)}_{[1:\#\text{sections}]}, \cdots \\
\text{equation (2.34)}_{[1:\#\text{sections}]}, \cdots \\
\text{equation (2.35)}_{[1:\#\text{sections}]}, \cdots \\
\text{equation (2.36)}_{[1:\#\text{sections}]}, \cdots \\
\text{equation (2.37)}_{[1:\#\text{sections}]}, \cdots \\
\text{equation (2.38)}_{[1:\#\text{sections}-1]}, \cdots \\
\text{equation (2.39)}_{[\text{considered-grid-points}]}
\end{bmatrix}
\tag{7.4}
$$

7.1.1. Objective Function

The objective function ($f(\mathbf{x})$) (equation (7.2)) is defined as the Root Mean Square Deviation (RMSD) of the computed deformations compared to the objective deformations, which are the deformations of the full-scale reference model scaled with k_b. In the Nastran model, the locations where these deformations are considered are leading and trailing edge locations that match the original full-scale model grid. The leading and trailing edges are chosen since this incorporates the twist of the wing. For the SBW this includes the leading and trailing edge points along the strut to make sure that the strut does not bend or twist very differently. A RMSD objective function is minimizing and when this function is zero the deformations perfectly match the scaled full-scale result. This function is chosen as it is a proven method to determine the overall error at multiple locations. Also, a larger difference gets penalized more than a small error due to the nature of the RMSD. The number of points in the developed framework is set at the number of nodes of the full-scale model, as these points were simple to extract. The number of points, due to the averaging in the RMSD, does not matter but using more points checks the wing's difference at more points, thus being more accurate, but it also takes more time to compute.

7.1.2. Design Vector

The design vector, $\mathbf{x}$, consists of the variable lamination parameters and the laminate thicknesses of the wing. If the wing would consist of one single laminate throughout the whole span this would then consist of 7 parameters for the wing, $\xi_{1,2,3}^{[A,D]}$ and the thickness. $\xi_4^{[A,D]}$ and $\xi_{1,2,3,4}^{B}$ are ignored since they will always be zero for a symmetrical laminate consisting of only -45,0,45,90 plies, as discussed in section 2.3.2.2. If the wing consists of n panels, the number of variables is $7 \cdot n$. For the SBW, the same goes for the strut, again 7 variables are added per panel and are added at the end of the design vector as in equation (7.3). For the cantilever wing that part of the design vector does not exist.

7.1.3. Constraints

The constraint equations, equation (7.4), earlier described in equations (2.33) to (2.36), (2.38) and (2.39) can be applied by adding a nonlinear inequality constraint function that returns a vector, $\mathbf{c}$, which contains the constraint function values.

The lamination parameter feasibility constraints (equations (2.33) to (2.37)) are applied for each composite section, as each section has its own laminate for which the parameters should be feasible. The blending constraints (equation (2.38)) are applied for each section minus one, since blending only occurs for multiple laminate panels. For the strut-braced wing, the feasibility constraints are also present for each panel. Additionally, the blending constraints are analyzed for the strut separately and are, thus, present for the number of wing panels minus one and the number of strut panels minus one.

The strength constraints (equation (2.39)) are computed for each considered grid-point, which is independent of the number of optimized sections. While a single value could be returned for every single grid point that is part of the shell, it was chosen to summarize this and return a worst-case value for an area to reduce matrix sizes. Additionally, since the strut-wing-connection causes a singularity, as discussed in section 6.2, it was chosen to ignore the strains near this point for the SBW. Summarizing the strains at the grid points into areas could cause non-convexities of the constraint function when the worst-case grid point would change. The worst-case point, however, is generally at the same location for each area and adding all points would result in thousands of constraint parameters (just over 10.000 nodes when using the 3-times refined grid from section 6.4). It was therefore decided to group all nodes in the original sections into one worst-case value, for each direction (compression and tension in x, y, and xy direction).

7.1.4. Bounds

The design variables are bounded by upper (ub) and lower (lb) bounds. For the lamination parameters these are 1 and -1 respectively due to their nature, see equations (2.29) to (2.31).The lower bound for the thickness is set to the thickness of 4 plies and the upper bound is related to the available space inside the wing. The latter is determined by the thinnest airfoil thickness for each panel, which is always at the most outboard cross-section. The upper bound for the laminate thickness is then set to 1/3 of the airfoil thickness to allow space for the curvature and for foam inside.

7.2. Optimization Routine

This section shows the chosen optimizer settings and shows an overview of the developed framework program. Matlab's gradient-based nonlinear constraint optimizer fmincon is used to optimize this problem. Lamination parameters result in a continuous design space (rather than using ply angles), which allows for the use of such solvers.

Figure 7.1 shows a layout of the lamination parameter optimization script. The darker box shows the tasks performed within the optimization while the outer items show inputs, outputs, and functions that are performed only one time. The structural model consists of the scaled rigid geometry which is translated into grid points and element connections in the 'create Nastran SOL101 files' function. This creates all the BDF-files needed by Nastran SOL 101 except for the file containing MAT and PSHELL cards which are defined by the design vector within the optimization as these contain laminate information.

The material properties of a single-ply are needed as an input, as they are used to determine the material properties from the design vector. They are, together with the geometric shape of the model, also used to determine the bounds. The minimum thicknesses (lb) were defined as at least four times the ply thickness. The maximum thicknesses (ub) are determined from the crossectional airfoil thicknesses, see section 7.1.4.

There are several optimization settings that can be defined for fmincon such as the algorithm used, the finite difference step size, and tolerances. It was found that the default fmincon algorithm 'interior-point' performed poorly when near a nonlinear constraint boundary and often stopped prematurely while a better (also feasible) optimum could be found. The 'sqp' (sequential quadratic programming) algorithm was found to perform better although it often returned a (very slightly) infeasible point. While the constraints are necessary to bound the problem to a feasible result, a very slight break of these constraints is not a major concern as it involves an initial design. The finite difference step size was changed from its default to make sure Nastran would return a different answer when a small change was made to any of the design variables. Before changing this value, the design vector is normalized so that each variable has roughly the same magnitude. The laminate thicknesses are approximately three orders of magnitude smaller than the lamination parameters. Equation (7.5) shows the normalized design vector, which is, within the optimization, scaled back to the actual lamination parameter values

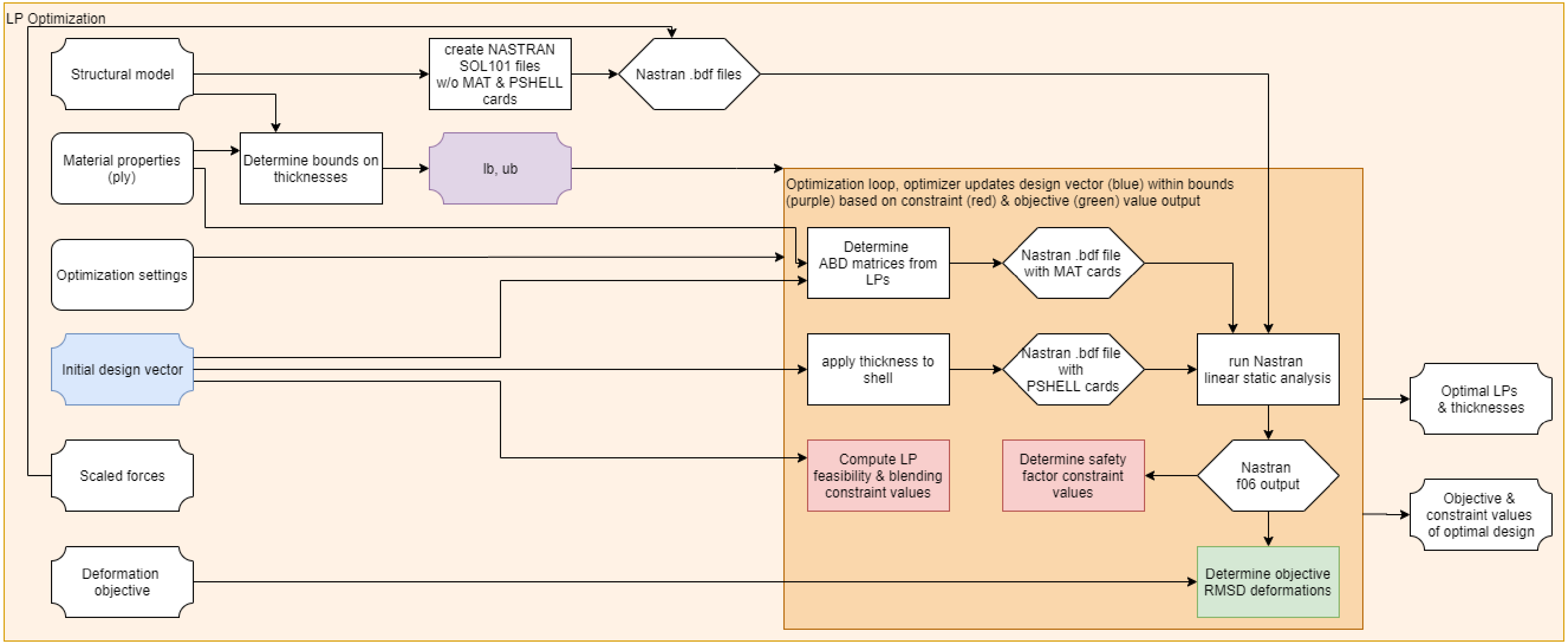

Figure 7.1: Lamination parameter optimization function overview

and thicknesses. The finite difference step size is set to 10^{-5}, as it was found that a step of 10^{-6} would not result in a difference to the Nastran results, for a step in all design variables. This is due to the limited number of characters used in Nastran's in and output files. The other settings, such as tolerances for stopping criteria, were kept at their original settings as these proved to yield sufficient results.

$$\mathbf{x_{normalized}} = \begin{array}{l} [0.1 \cdot (\xi_{1,2,3}^{[A,D]})_{[1:\#\text{sections}_{\text{wing}}]}, \dots \\ 100 \cdot \text{t}_{[1:\#\text{sections}_{\text{wing}}]}, \dots \\ (0.1 \cdot \xi_{1,2,3}^{[A,D]})_{[1:\#\text{sections}_{\text{strut}}]}, \dots \\ 100 \cdot \text{t}_{[1:\#\text{sections}_{\text{strut}}]} \qquad\qquad] \end{array} \tag{7.5}$$

An initial design vector is required by fmincon. The sqp algorithm does not require this initial point to be feasible, so nearly any design vector will work. Using a feasible (or near feasible) starting point can prevent Nastran from crashing, as an infeasible lamination parameter choice may lead to excessive pivot ratios in the stiffness matrices, resulting in a NaN result for the objective function. While the algorithm is able to recover when a NaN result is found after taking a step, starting with such a result does not work.

The final input needed is the deformation objective, which is the scaled deformation found from the full-scale aerodynamic analysis in section 5.2.1.

The optimization itself consists of a few steps. To determine the objective, first, the lamination parameter parts from the design vector are converted to ABD matrices and printed in a Nastran input bdf file with MAT2 cards. The PSHELL cards are added to a bdf file as well, which contains the laminate thicknesses. Nastran's linear static analysis is then performed and it returns an output file. This file contains the deformations and the strains at the nodes. The deformations are extracted and the RMSD is determined by comparing these deformations to those of the deformation objective, which gives the objective function value.

The constraints are in part directly computed from the design vector (LP feasibility constraints and blending constraints). The strength constraints are determined by extracting the strains from the Nastran output. These strains are compared to the maximum ply material strains and the safety factor.

Fmincon updates the initial design vector during optimization while staying within the bounds and stops when the stopping criteria are met. The optimal design vector and its accompanying objective function value and constraint values are then returned.

7.3. Stacking Sequence Retrieval Using SST and OptiBless Integration

The found optimization results are in the continuous lamination parameter space and while analyzing the structure is possible, building a physical model using those parameters is not without converting it back to a stacking sequence.

This Stacking Sequence Retrieval (SSR) step is performed by using an open-source tool, OptiBless [63], which tries to find a laminate for which the lamination parameters are closest to the lamination parameters set as the objective. It uses a genetic algorithm. This tool was chosen since it is Matlab-based and it was most easily integrated. Another open-source tool, pyTLO [62], was considered, as it has some added functionalities, such as performing the optimization multiple times and updating the genetic algorithm population during optimization. Both tools showed similar results when testing them as long as larger population sizes were used. OptiBless' benefit of easier integration into the larger framework outweighed the additional options of pyTLO.

Since OptiBless uses a genetic algorithm and uses random mutations, finding the global optimum is not guaranteed. However, by using a large population and many generations, a large portion of the design space can be searched and finding the global optimum becomes more likely. OptiBless is expected to work better for optimizations with a smaller number of varying lamination panels, as the number of design variables is smaller, compared to using many.

The tool works using stacking sequence tables. This means that the thinner panels contain plies that are an (ordered) subset of the thicker laminates. Several manufacturing constraints can be turned on and off in the settings, such as symmetrical and balanced laminates only, the discrete steps in angles. Other manufacturing constraints include design rules that are aimed at improving damage tolerances, by using ± 45 plies as the outer plies, or disorientation guidelines, where 2 consecutive plies may not have an angle change larger than 45 degrees. As this step was considered to be more of a validation for possible laminates to exist that can form a design to match the deformations of the full-scale wing, most of these options were turned off. Only the symmetry requirement was turned on and the discrete angle settings were set to 45 degrees, as the lamination parameter optimization was done with these requirements in mind.

The blending constraints, equation (2.38) should aid OptiBless in finding possible stacking sequences, as was found by Macquart et al. [61]. The genetic algorithm settings that have been used in this thesis are found in table 7.1. More detailed descriptions of OptiBless and what these settings do can be found in the user manual [63].

Table 7.1: OptiBless genetic algorithm settings used in this thesis

Population size	200
Minimum # stalled generations	1000
Elitism	0.02
Crossover	0.8

8

Optimization Results

This chapter discusses the results found with the optimization framework for different settings. The developed optimization framework was used to try to find initial composite wind tunnel model designs for both a strut-braced wing and a cantilever wing. This was done for various options to test the robustness of the framework and to assess how well the chosen methodology works for both a conventional and non-conventional design. First, section 8.1 discusses the results for a changing number of laminate panels. Next, the robustness of the optimization results are analyzed in section 8.2 by running both wings for multiple starting points. Section 8.3 shows the capabilities of the developed framework and verifies the accuracy at other angles of attack.

8.1. Laminate Panel Number Variations

It was hypothesized that increasing the number of variations in laminate panels would decrease the error between the found model design and the deformation objective. This is because when the laminate can change more this allows for more directional stiffness variation, which is thus more likely to match those of the full-scale design. Increasing the number of panels, however, will increase the complexity of the design that is to be produced. The optimization time will also increase significantly. This is because the gradient determination, that is performed within fmincon, will have to perform one function evaluation per design variable to find the gradient. Without counting possible additional steps required, the gradient determination time will thus double when doubling the number of laminate panels. As each function evaluation takes roughly 10 seconds the gradient determination alone will take over a minute for one panel. Therefore, if the number of panels increases the computational efforts can increase significantly. While changing from one panel to two will likely have a large impact on the objective function, adding panels at some point may not decrease the objective function further and will only add complexity.

For both the strut-braced wing and the cantilever wing three different pressure scaling factors were considered, 1.25, 2.5, and 3.75, as these cover the possible range discussed in section 4.3. It is expected that for the lamination parameter space the optima may be slightly different but should follow a similar pattern. For the stacking sequence retrieval step it is expected that the higher the pressure scaling factor is the better OptiBless's results will be, as a thicker laminate will have more layers and thus more design freedom. The stacking sequence retrieval step is shown, but since this introduces discrete steps there is some randomness in how well the result matches, as the found optimum can be close or far from a possible existing blended laminate which is found by OptiBless. It is expected that the stacking sequence retrieval step will cause the deformation to deviate further from the objective and thus that the objective value will increase.

Each of these runs was run from the same starting point for each option. Optimizing all these points took roughly 8.5 days for the strut-braced wing. The cantilever's runs were cut-off due to time restrictions after also running for over 6 days, which is the reason for the missing data points compared to the strut-braced wing. The numbers of panels tried are 1,2,3,4,6,8,12 and 24, as this allows splitting the panels at the original node locations.

8.1.1. Cantilever Wing

The results of the first part, those of the developed optimization framework in the lamination parameter space, can be seen in figure 8.1. It can be seen that the function values drastically improve when changing the number of panels from one to two and from two to three, after this point, the function values do not improve much or even increase slightly. The full-scale beam model consisted of a modeled beam with three different properties, which may explain why the 3-panel wing performs notably better than the 4-panel wing for the two higher pressure scaling factors. A good performance for the 6-panel wing would however also be expected in this case.

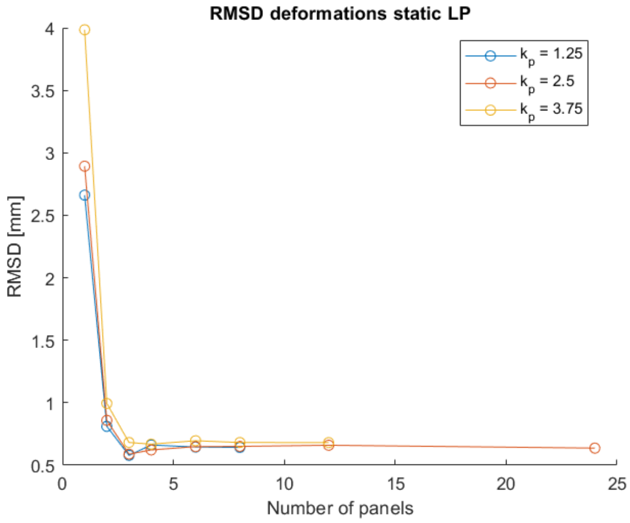

Figure 8.1: Function values found for different numbers of panels and pressure scaling factors for the cantilever wing. In the lamination parameter space for static results.

The optimization framework uses a static sum in which the scaled aeroelastic forces of the reference design are used as input. Since the found optima are not perfectly matching those deformations some deviations are expected when the force would be updated to the actual aerodynamic loads. The aeroelastic results of the found optima in the lamination parameter space can be found in figure 8.2. It can be seen that the aeroelastic results follow a similar trend, if the result in the lamination parameter space was good it will also give good aeroelastic results, but some deviations can be seen.

The deviation between the aeroelastic results, seen in figure 8.2, for the 6-panel wing for $k_p = 2.5$, for example, can be explained when considering the twist angles that correspond to this result. Figure 8.3 shows the deformation (top) and twist (bottom) results for both the static (left) and aerodynamic (right) results. While the static deformation result matches the objective very well, it can be seen that the twist angle is slightly more negative at all locations. This slightly more nose down twist causes the wing to deform less as the local angle of attack is smaller. This explains the larger deviation for the aeroelastic results. The RMSD, which determines the fitness in the optimization, does a good job in matching both the leading and trailing edge in figure 8.3a, however, the leading edge is slightly lower than the objective and the trailing edge is slightly higher. Since the sign of the deviations is not included this leads to a deviation in the twist, which, once converted to an aeroelastic result, causes extra deviations.

Naturally, the stacking sequence retrieval step can also cause a deviation from the objective as the actual thickness and lamination parameters will change slightly from the found objective. The discreteness of stacking sequences causes this step to be irregular in size, as a found optimum can either be close or far from an actually possible laminate. Figure 8.4 shows the RMSD found after the SSR tool OptiBless was used. It can be seen that the lowest pressure scaling parameter performs poorly, as expected. This is due to the lower thickness, thus a lower amount of plies in the laminate, which causes a more limited design space. The other two scaling parameters perform much better but all RMSDs are

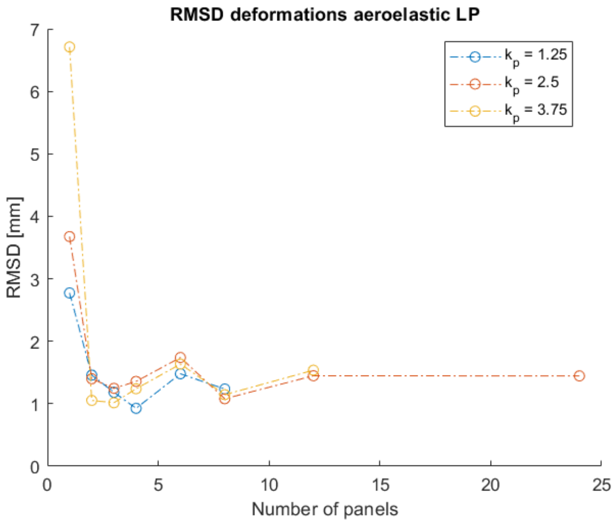

Figure 8.2: Function values found for different numbers of panels and pressure scaling factors for the cantilever wing. In the lamination parameter space for aeroelastic results.

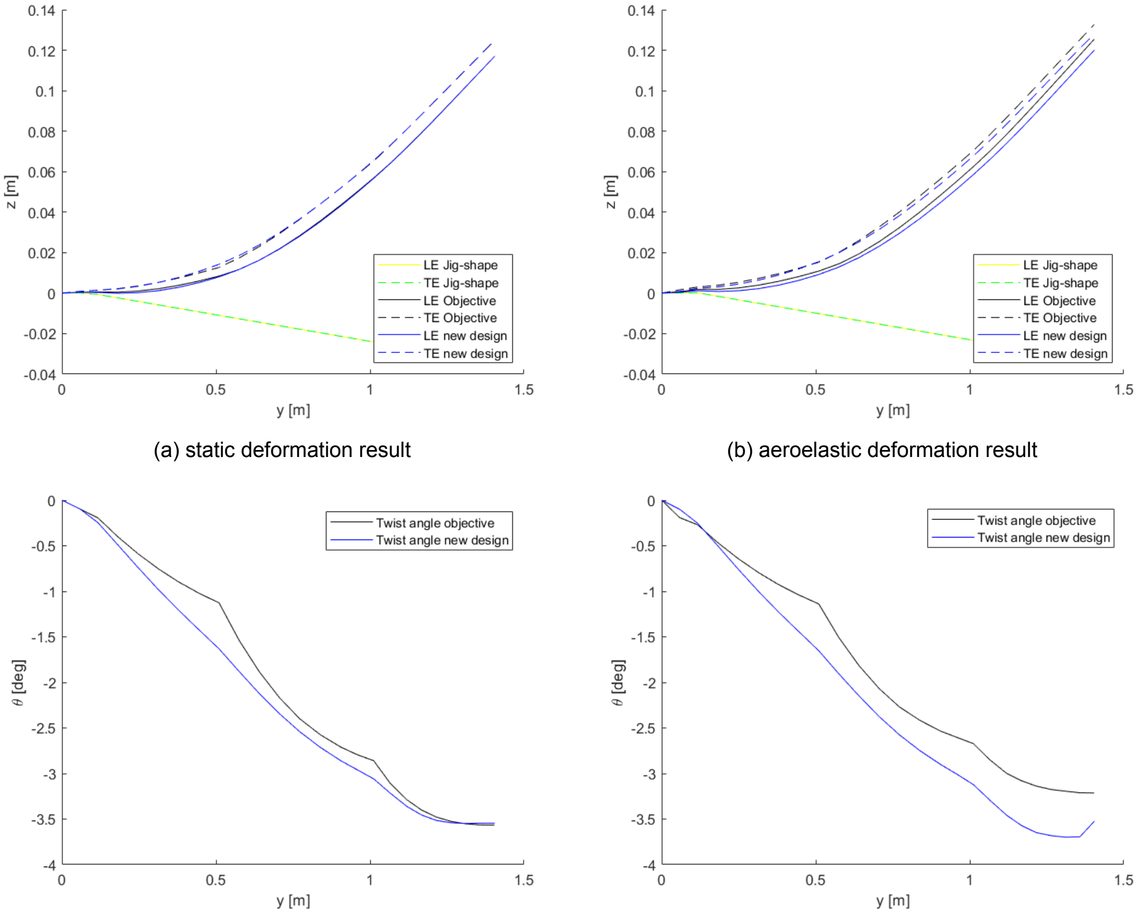

(a) static deformation result

(b) aeroelastic deformation result

(c) static twist result

(d) aeroelastic twist result

Figure 8.3: Lamination parameter results for 6-panel cantilever wing with $k_p = 2.5$. Showing the effect of twist on the progression from the static to aeroelastic result.

higher than those from the Lamination Parameter (LP) optimization results. These results have larger differences between the panels than found by the lamination parameter optimizations, which is likely due to the discreteness of the problem that also causes the graph to show less smooth results.

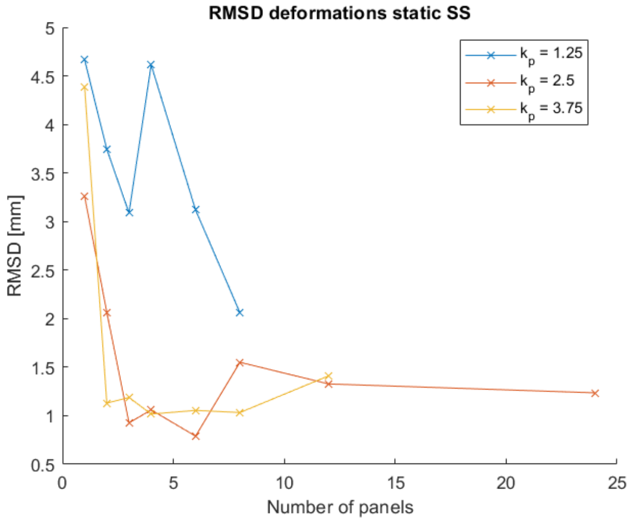

Figure 8.4: Function values found for different numbers of panels and pressure scaling factors for the cantilever wing. Static results for retrieved stacking sequence.

When considering the aeroelastic results for the retrieved stacking sequences, seen in figure 8.5, the higher deviations from the optimum found cause the aeroelastic results to become less smooth as well, when compared to figure 8.2. Not only can the difference in twist in the static result cause the aeroelastic result to deviate away from the objective, but it may also cause it to deviate towards the objective and become a better fit. When the static results closely match the objective results, the aeroelastic results will also be a close match. However, once the static results start to deviate from the objective the aeroelastic results can either improve or hinder the results.

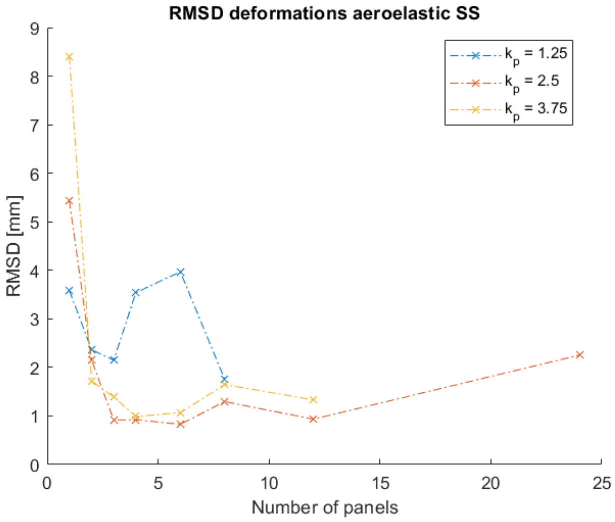

Figure 8.5: Function values found for different numbers of panels and pressure scaling factors for the cantilever wing. Aeroelastic results for retrieved stacking sequence.

Figure 8.6 shows the deformation and twist results for the static and aeroelastic results of the retrieved stacking sequence with 12 panels for $k_p = 2.5$. It can be seen in figures 8.4 and 8.5 that the objective actually improves after the aeroelastic result. In figure 8.6 it can be seen why. The deformation for the static result is slightly lower than the objective, at the same time there is less nose down twist. As less nose down twist causes higher local angles of attack the deformation increases for the aeroelastic result.

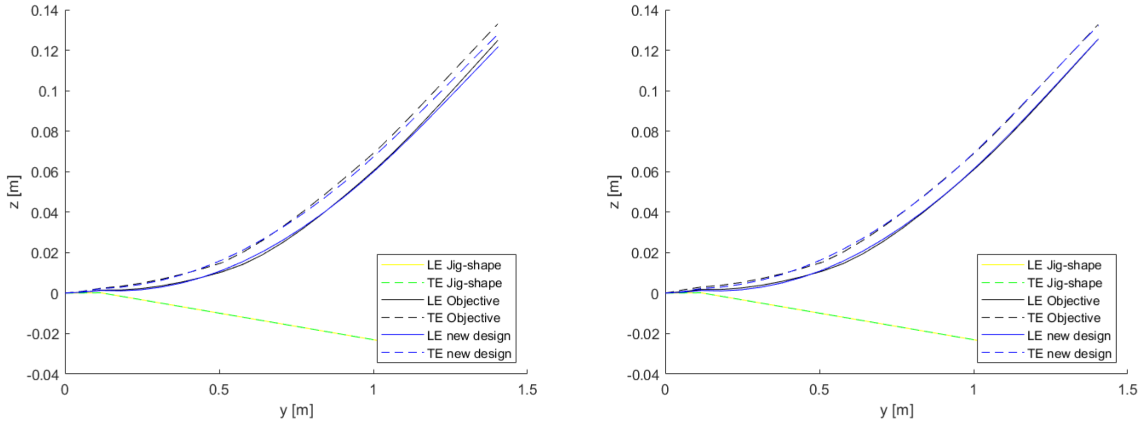

(a) static deformation result

(b) aeroelastic deformation result

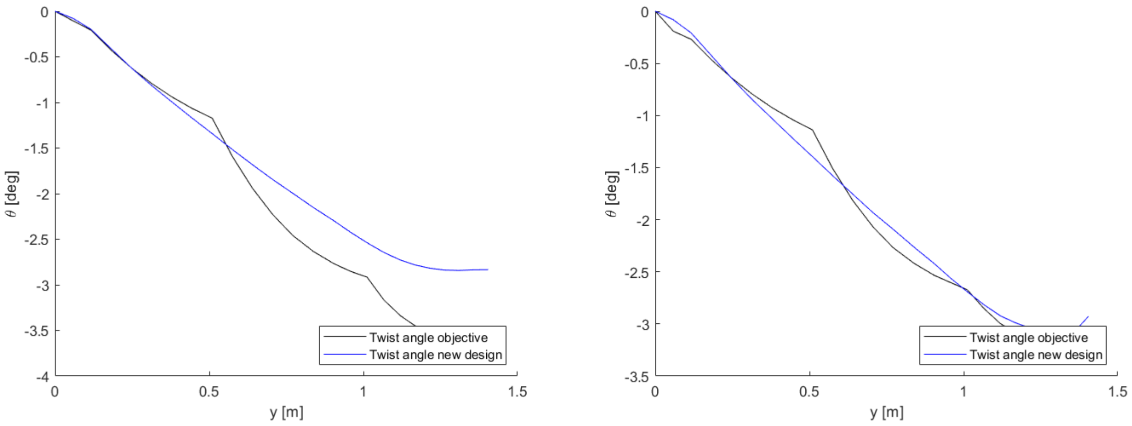

(c) static twist result

(d) aeroelastic twist result

Figure 8.6: Lamination parameter results for 12-panel cantilever wing with $k_p = 2.5$. Showing the effect of twist on the progression from the static to aeroelastic result.

Overall, the created optimization framework performs well for the cantilever wing. Improvements could be made by, for example, including the twist angle in the objective function. Another option to consider is to include the aeroelastic sum in the optimization routine. This would increase the computational efforts needed for the optimization.

8.1.2. Strut-Braced Wing

For the strut-braced wing, the optimization framework was also evaluated for varying panels and pressure scaling factors. It was quickly found that the optimization framework struggled with finding designs that matched the objective deformations under load. Figure 8.7 shows the RMSD after optimizing in the lamination parameter space. While some of the optima are certainly performing well (the RMSD is of similar value as those found for the cantilever wing) it can be seen that the optimizer does not give consistent results. The clearest point for this is the 8-panel wing for $k_p = 3.75$, which found an optimum far away from the other panel options. It is suspected that the optimizer gets stuck in local optima due to the non-convexity of the problem. This is further explored in section 8.2. For $k_p = 1.25$, it seems that the optimizer got stuck in similar optima for 6, 8 and 12 panels. As mentioned before, there is no reason for the optimizer to find very different results for the different pressure scaling factors while in the lamination parameter space. It is therefore likely that the optimizer was unable to find the global optimum for many of the shown runs. What is also seen is that the single-panel SBW performs notably better than the cantilever wing. This is due to the fact that, the strut holds the center of the wing down.

This restriction on the wing's deformation causes the average differences in deformations to be much smaller.

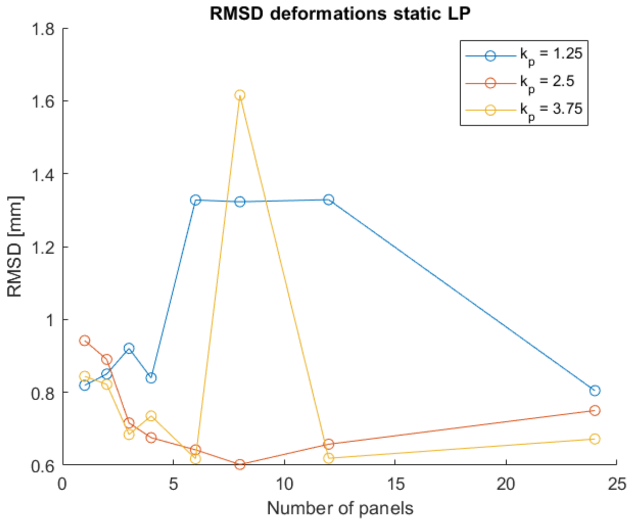

Figure 8.7: Function values found for different numbers of panels and pressure scaling factors for the strut-braced wing. In the lamination parameter space for static results.

When looking at the aeroelastic results for the found optima in the lamination parameter space similar results can be seen, as was shown in the previous section for the cantilever wing. Designs that are a good match in the static evaluation are indeed also doing well when checking the aeroelastic result. Again some deviations can be seen, which can be explained by the effect of the twist on the aeroelastic results as explained by figures 8.3 and 8.6. What is notable, however, is that the function value roughly doubles when comparing the static and aeroelastic results, which was (on average) much smaller for the cantilever wing.

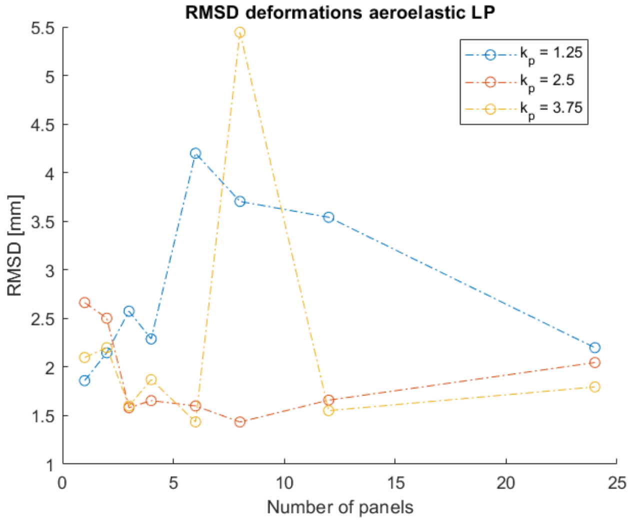

Figure 8.8: Function values found for different numbers of panels and pressure scaling factors for the strut-braced wing. In the lamination parameter space for aeroelastic results.

When considering one of the better points, the 8-panel $k_p = 2.5$ result, for example, shows that found optimum is a good match, except for the area near the strut-wing-joint. For the rest of the wing, the twist is also less, which causes the increased deformation for the aeroelastic result. When checking the found optimum, it was seen that the strut thickness is slightly thinner than the set upper bound. This means the differences at the strut-wing-joint would not be able to improve much.

A similar pattern is seen for all of the results that perform well. The strut in the optimization never seems stiff enough to keep the wing down enough. This causes higher local angles of attack, at least near the strut-wing-joint, but also slightly overall. This in turn causes a higher lift force in the aeroelastic analysis which gives rise to higher deformations near the tip.

The full-scale strut seems to be very stiff already, leading to issues when scaling. Equation (2.16) showed that the bending rigidity scaling is related to the pressure scaling, Mach scaling and length scaling: $k_{EI} = k_p k_{M_a} k_b^4$. While it does not transfer one to one since different structural concepts are used, it means, in general, that if the pressure scaling increases the rigidity has to increase. This means, that either the Young's modulus (E) or the moment of inertia (I) should increase. Since material properties can not change by large amounts this will result in a necessary increase in the I, which, since the airfoil shape does not change, will nearly always require a larger material volume. Thus, if the material for the full-scale design was on its upper limit of fitting in the structure it may become impossible to fit a feasible structure for a scaled wing.

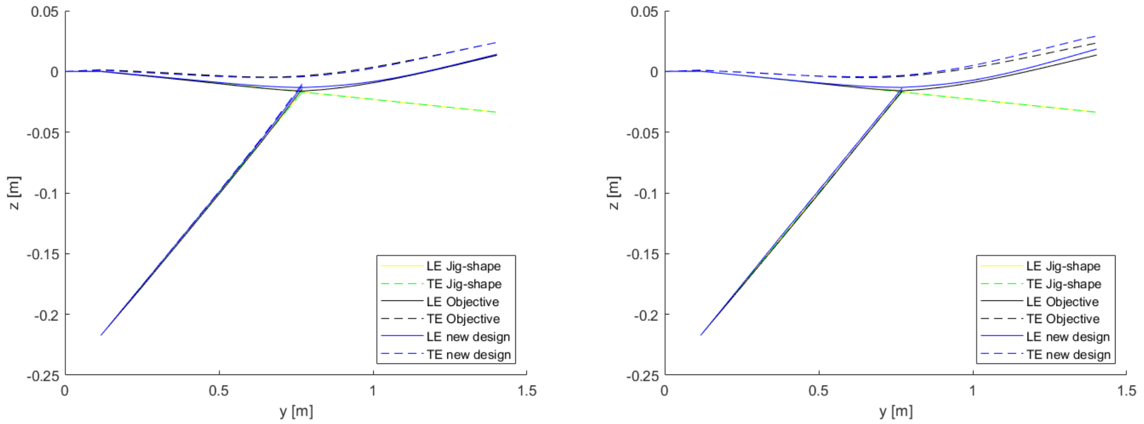

(a) static deformation result

(b) aeroelastic deformation result

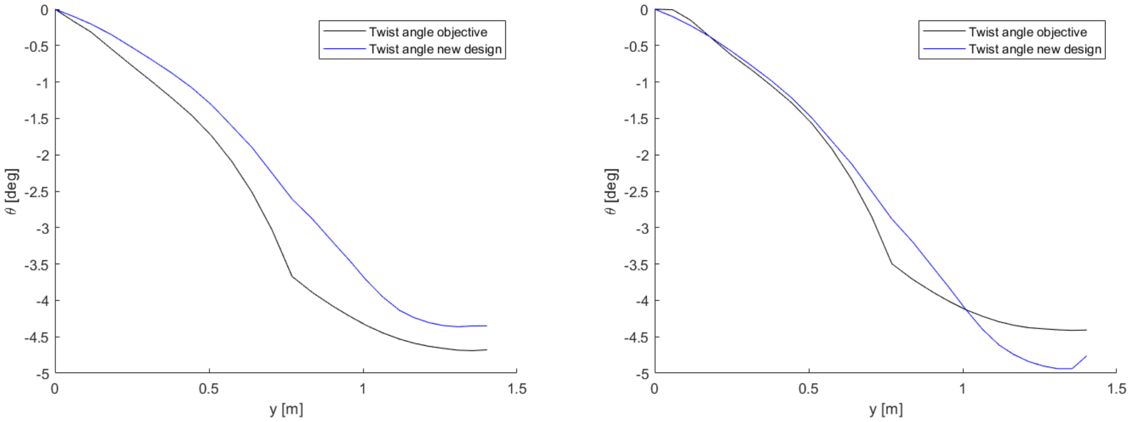

(c) static twist result

(d) aeroelastic twist result

Figure 8.9: Lamination parameter results for 8-panel strut-braced wing with $k_p = 2.5$. Showing the effect of twist on the progression from the static to aeroelastic result.

After SSR, there, again, is a deviation from the objective. Since the strut and wing are not considered together in the SSR step there is no difference in how OptiBless works between the cantilever and strut-braced wing. Again, this step shows large fluctuations in how well the newfound laminate performs after this step. The lowest pressure scaling factor again gives the biggest fluctuations.

The final aeroelastic results are shown in figure 8.11. It is clear, once more, that there is a large deviation between the static and aeroelastic results after SSR. Some points are significantly better, such as the $k_p = 1.25$ single-panel wing, which becomes the best overall design.

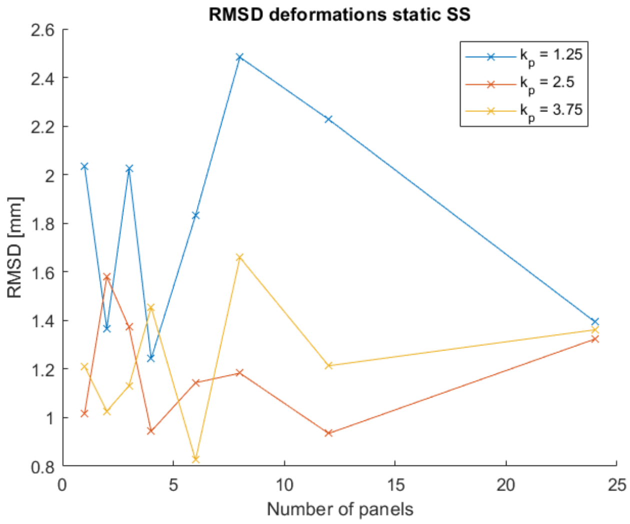

Figure 8.10: Function values found for different numbers of panels and pressure scaling factors for the strut-braced wing. Static results for retrieved stacking sequence.

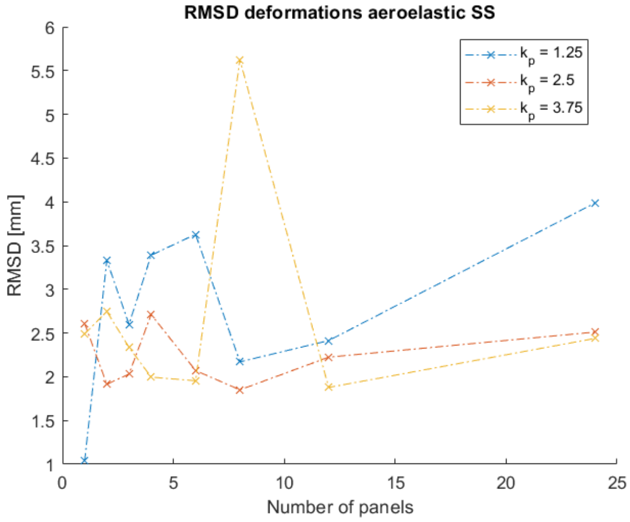

Figure 8.11: Function values found for different numbers of panels and pressure scaling factors for the strut-braced wing. Aeroelastic results for retrieved stacking sequence.

It can be seen that for the strut-braced wing the developed optimization framework performs much less robustly. While some designs may be considered good enough for wind tunnel testing (see section 8.3, for an analysis of the best results), the lamination parameter optimization shows strongly varying results. It is suspected that a composite shell structure for the strut-braced wing is highly non-convex, causing the wing to get stuck in local optima. Also the specific use-case, the AGILE H2020 SBW seems to have a strut so stiff that it is impossible to create a scaled design with a stiff enough strut.

8.2. Initial Value Variations

It was suspected that the optimization results for the strut-braced wing may be stopping in local optima. A similar pattern as seen for the cantilever wing, where more panels result in a better optimum, was expected but not seen. To confirm the suspicion a multiple start point optimization was performed. Changing the optimization framework slightly to incorporate a global search method can simply be done, using the Global Optimization toolbox, but, for research purposes, this task was performed manually by defining multiple start points and running the optimization for each of these start points.

8.2.1. Cantilever Wing

Figure 8.12a shows the deformation results for a single-panel cantilever wing for eleven different start points[1]. These points span ten equally spread points between the lower and upper bounds and the initial start point used in the previous section. Each of the found designs is shown in blue and whereas the lines show slightly thicker than the objective, which indicates some variation, the lines overlap nearly perfectly. When looking at the twist results it can be seen more clearly that some differences are present. From figure 8.13 it becomes clear that indeed, most optima are close together. Only very small differences are present and a change in RMSD of 0.1mm is expected to lie within the margin of error of manufacturing the wind tunnel model.

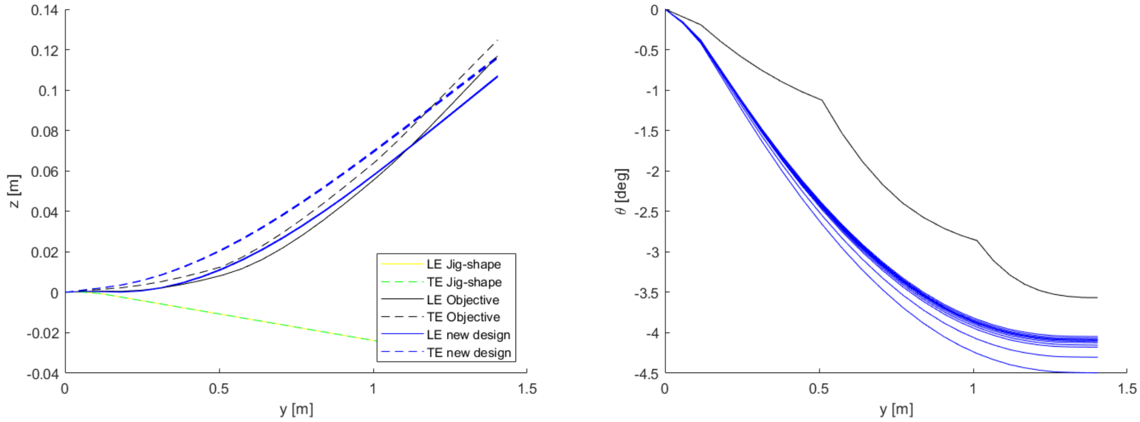

(a) Deformations

(b) Twists

Figure 8.12: Results for optima from eleven different start points, for a single-panel wing for $k_p = 2.5$

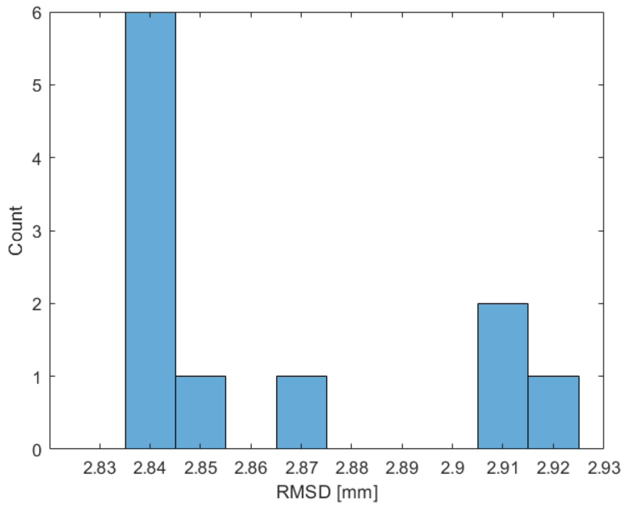

Figure 8.13: Histogram of the objective value after optimization from eleven different start points

8.2.2. Strut-Braced Wing

For the strut-braced wing, the results were not as robust. By just looking at the deformations, shown in figure 8.14a, without zooming in it can already be seen that the found optima are different. This is even more visible when looking at the twist plot in figure 8.14b. The histogram in figure 8.15, which has bars with the same width as seen for the cantilever version, clearly shows a much wider variation. This

---

[1] Since it is a single-panel wing the results are quite poor overall, this section is purely to test the robustness of the developed framework

indicates that the optimization is non-convex, getting stuck in local optima. While this is the case for both the cantilever and strut-braced wing the cantilever wing was able to get close to the same (very likely to be global) optimum in all cases. The strut-braced wing showed a great variety, indicating many local optima, which were often far away from the global optimum.

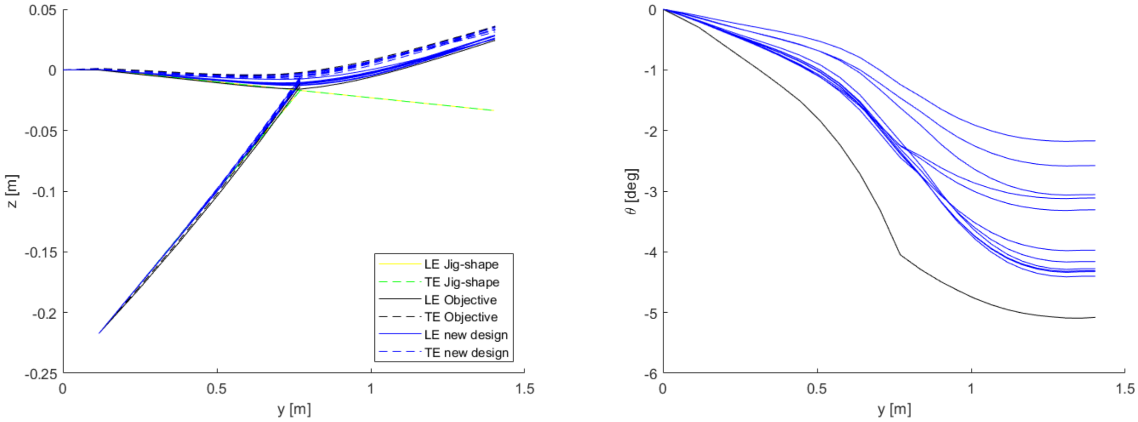

(a) Deformations (b) Twists

Figure 8.14: Results for optima from eleven different start points, for a single-panel wing for $k_p = 2.5$

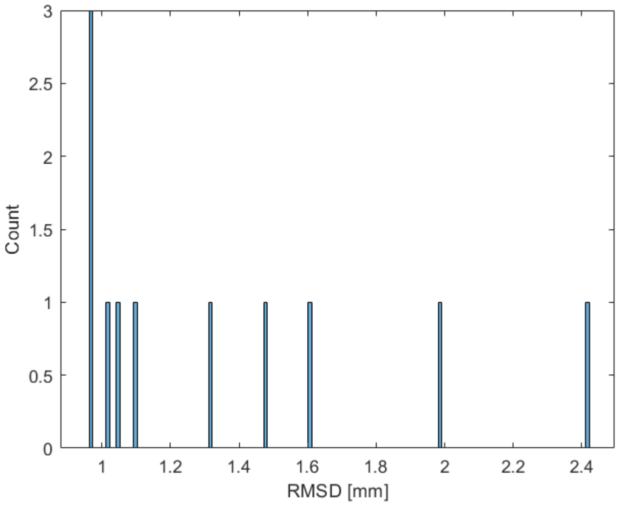

Figure 8.15: Histogram of the objective value after optimization from eleven different start points

The amount of iterations the optimizer uses to get to the optimum value differs a lot. For the two points of the strut-braced wing that actually did find the same optimum, one took nearly twice as long as the other. Figure 8.16 shows the function value at every iteration of the optimizer for the two best points, which converge to the best value, in blue and yellow. It also shows, in red, an optimization run that had a better starting value, which converged to a local optimum.

The blue line corresponds to one of the optimizations that started with an initial design very far away from the optimum. It quickly found a much better design but then progressed very slowly. The red optimization run started at the best initial design but eventually got stuck after slowly progressing for many iterations.

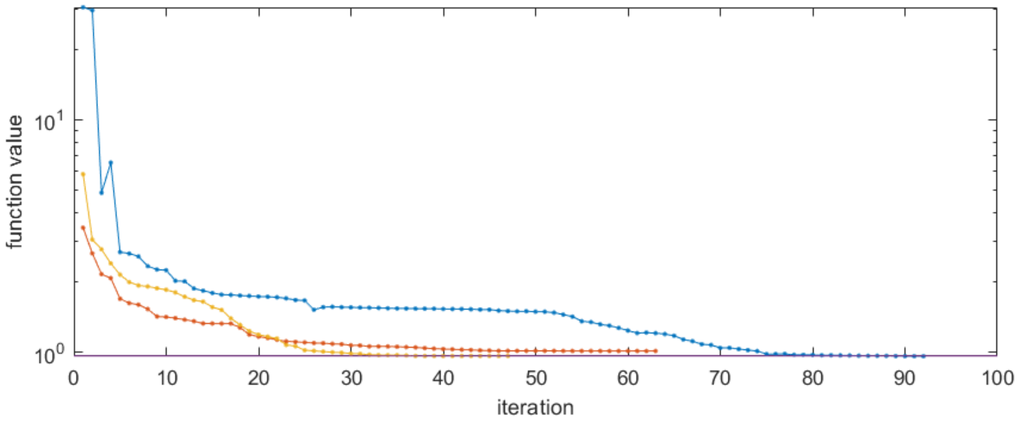

Figure 8.16: Function value at each iteration for three different start point optimization runs

8.3. Framework Capabilities and Aeroelastic Verification

This section considers some of the better results for both wings to show how well the optimization framework is capable of finding a design with static aeroelastic similarity. This is done by analyzing not only the angle of attack at which the optimization was performed but by also considering other angles in the test envelope.

8.3.1. Cantilever Wing

For the cantilever wing, a few promising designs were found, as was seen in figure 8.5. The $k_p = 2.5$ 4-panel cantilever wing was one of the options that showed a low objective value for the aeroelastic analysis with the retrieved stacking sequences. Figures 8.17 and 8.18 show the deformation and twist of the aeroelastic result for the found stacking sequence. It can be seen that these indeed have a close match with the objective deformations.

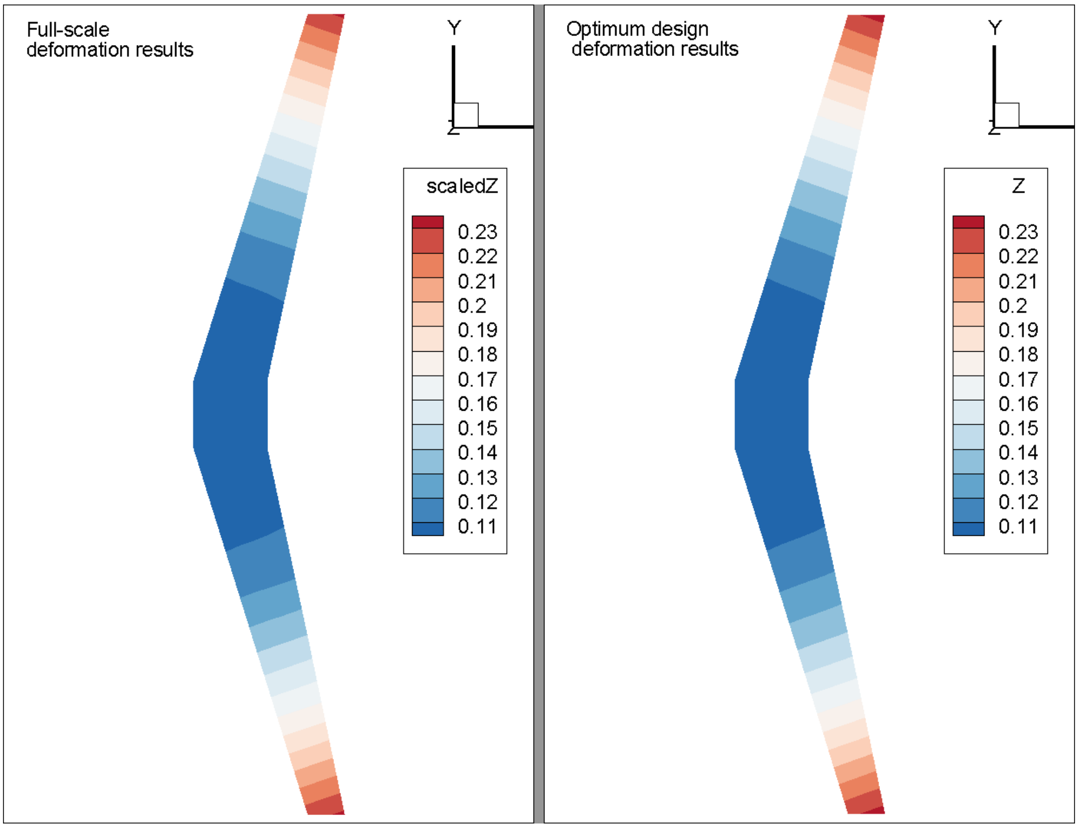

Figure 8.17: Comparison between aeroelastic deformations of full-scale and stacking sequence found after optimizing with a 4-panel cantilever wing for $k_p = 2.5$, for α = 5 degrees

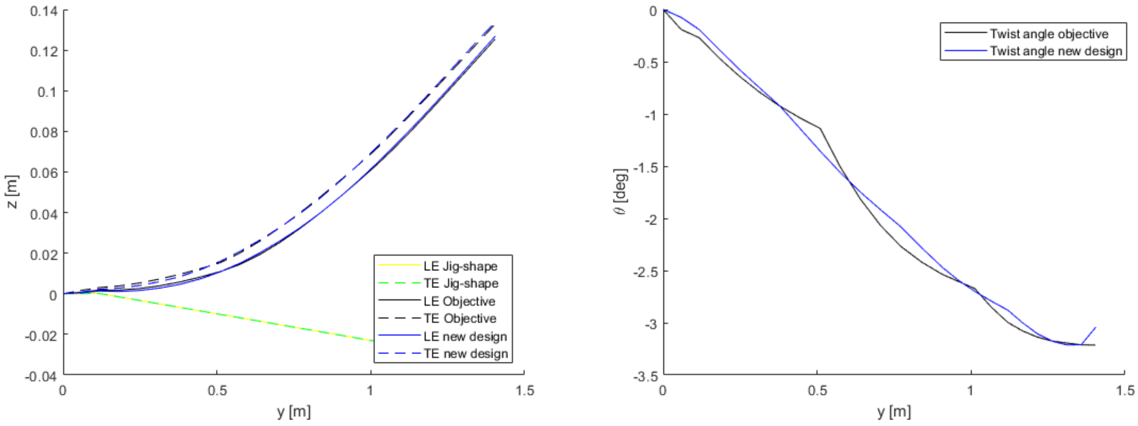

(a) Deformations (b) Twist

Figure 8.18: Aeroelastic results for the stacking sequence found after optimizing with a 4-panel cantilever wing for $k_p = 2.5$ for α = 5 degrees

Figure 8.19 shows the pressure distribution found by ZAERO for the full-scale and the scaled optimum design. It can be seen that, in general, they match very well. From table 8.1 it can be seen that there are small differences between the full-scale and scaled aerodynamic results. The rigid results are shown as these give an indication of the error introduced due to scaling (as discussed in section 5.4). A difference of 1.8% in the computed lift is shown for the aeroelastic (flexible) results.

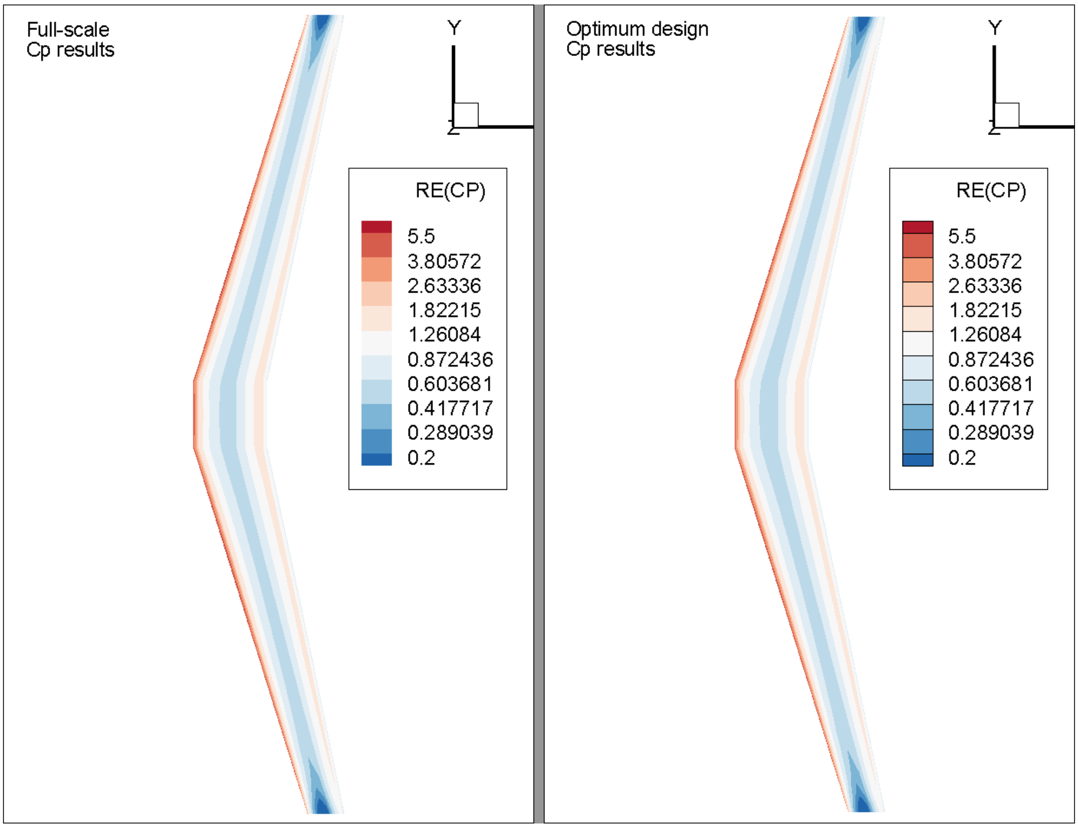

Figure 8.19: Comparison between pressure coefficients of full-scale and found optimum with the stacking sequence found after optimizing with a 4-panel cantilever wing for $k_p = 2.5$, for α = 5 degrees

Table 8.1: ZAERO results for the optimized 4-panel cantilever wing for $k_p = 2.5$ for α = 5 degrees

	Full-scale		Optimized design	
COEFFICIENTS	FLEXIBLE	RIGID	FLEXIBLE	RIGID
INDUCED DRAG(CDL):	0.11398	0.10495	0.11369	0.10457
DRAG AT TRIM(CD0):	0.02149	0.02149	0.02142	0.02142
LIFT(CL):	1.01280	1.20261	0.99371	1.19827
PITCH MOMENT(CM):	-0.35559	-0.44179	-0.39717	-0.49467

The differences in lift stay roughly the same for other angles of attack, as can be seen in figure 8.20. Since the total lift coefficient changes the percentage difference does increase for lower angles of attack. The difference in deformation actually decreases for this found design for slightly lower angles. This is partly inherent to the fact that the total deformations are lower but this was not seen for all close optima, for example, the 6-panel final optimized design also showed a good fit but the function values increase for all other angles of attack. See appendix C.1, for how this optimum behaves for other angles of attack. This is likely due to the fact that the twist of the wing was very slightly more negative over the entire wing. This effect is increased by changing the angle. For the design shown in this section, the mean twist was very comparable to that of the objective.

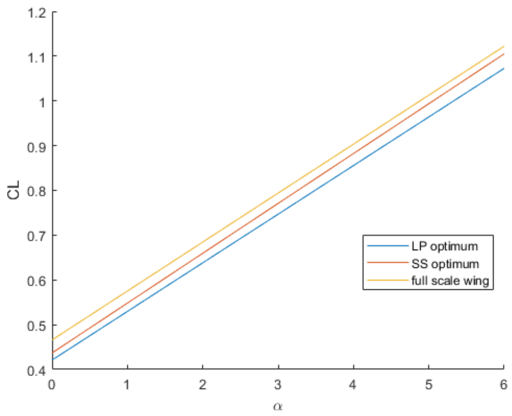

Figure 8.20: Lift polar for full-scale and found optima (LP and SS) after optimizing with a 4-panel cantilever wing for $k_p = 2.5$

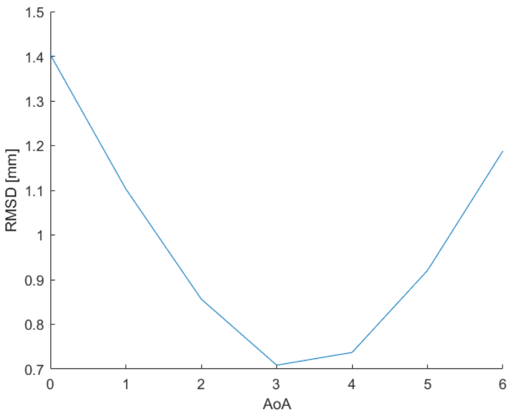

Figure 8.21: RMSD with full-scale deformation for best optimization result with a 4-panel cantilever wing for $k_p = 2.5$

The deformations shown before were those at the angle of attack for which was optimized (5 degrees). Figures 8.22 to 8.24 show the deformation, twist and pressure coefficient results for an angle of attack of 3 degrees. These show a very good match overall with the full-scale reference wing.

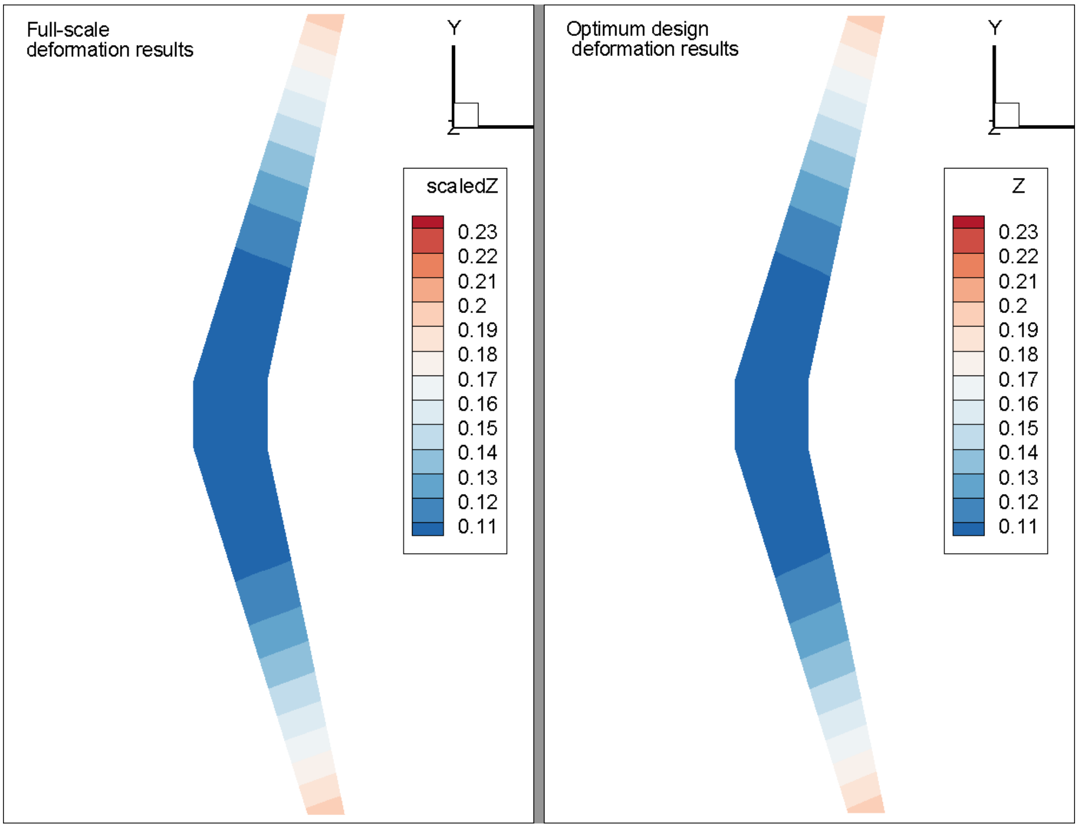

Figure 8.22: Comparison between deformations of full-scale and found optimum with the stacking sequence found after optimizing with a 4-panel cantilever wing for $k_p = 2.5$, for α = 3 degrees

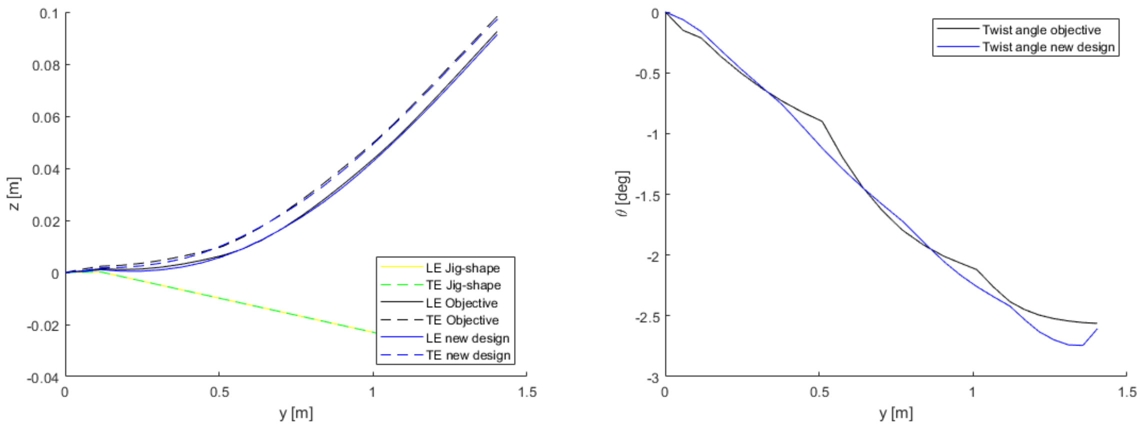

(a) Deformations

(b) Twist

Figure 8.23: Aeroelastic results for the stacking sequence found after optimizing with a 4-panel cantilever wing for $k_p = 2.5$ for α = 3 degrees

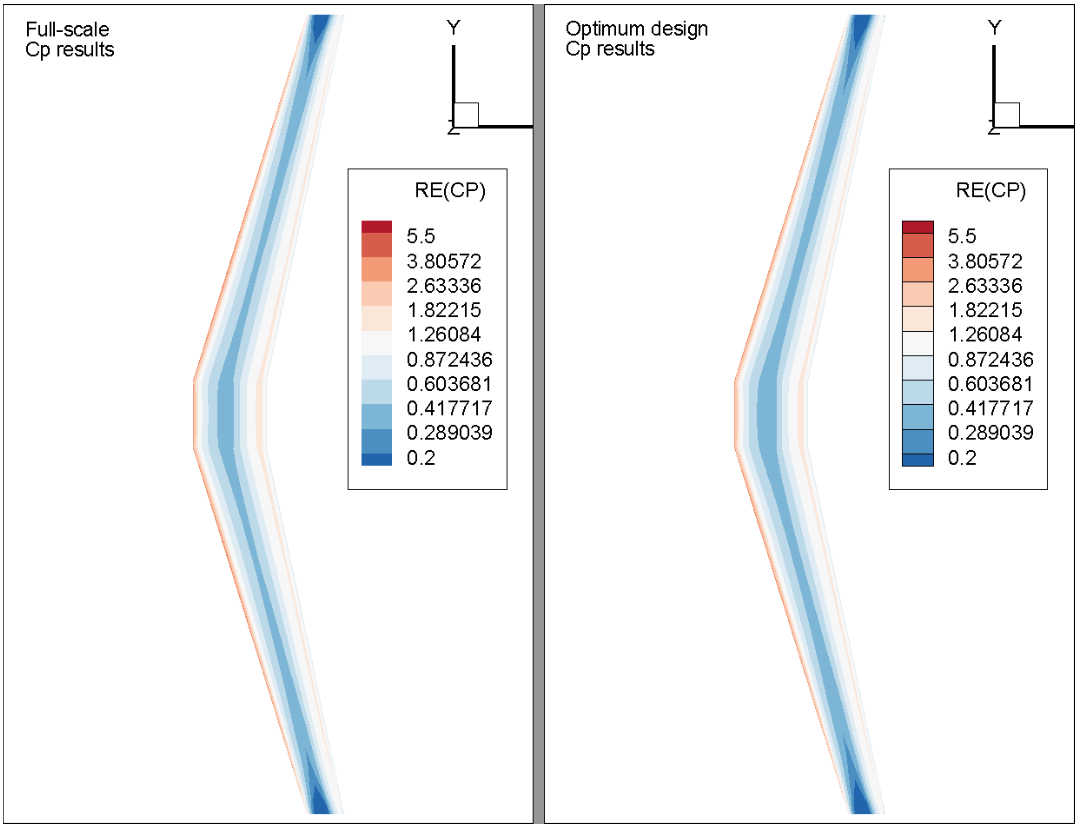

Figure 8.24: Comparison between pressure coefficients of full-scale and found optimum with the stacking sequence found after optimizing with a 4-panel cantilever wing for $k_p = 2.5$, for α = 3 degrees

For an even larger difference in angle of attack the deviations from the full-scale become larger. Figures 8.25 to 8.27 show the deformations, twist and pressure coefficients for an angle of attack of 1 degree.

The optimization was run for an angle of attack of 5 degrees. While this was necessary to check the strength requirements directly, as it was the test-case with the highest forces, it may be better to add a low angle as well and use two angles for a multi-objective optimization. While more likely to give good results throughout the test envelope, it would add computational efforts.

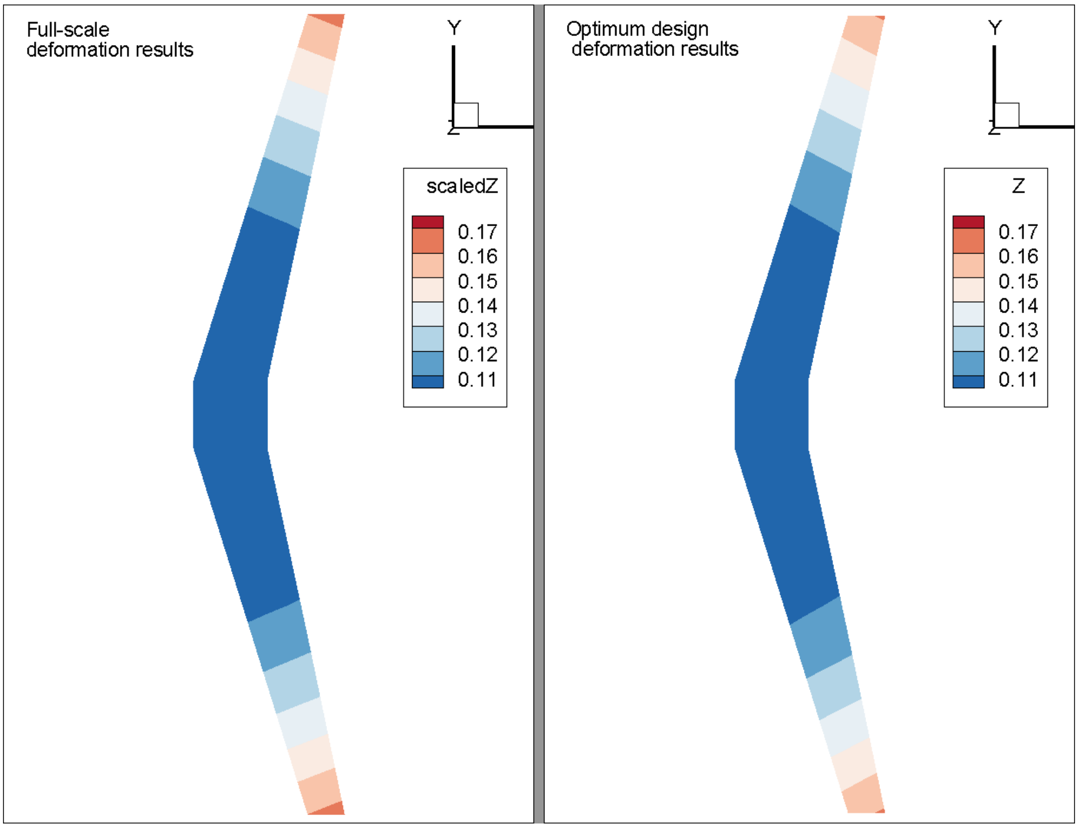

Figure 8.25: Comparison between deformations of full-scale and found optimum with the stacking sequence found after optimizing with a 4-panel cantilever wing for $k_p = 2.5$, for α = 1 degrees

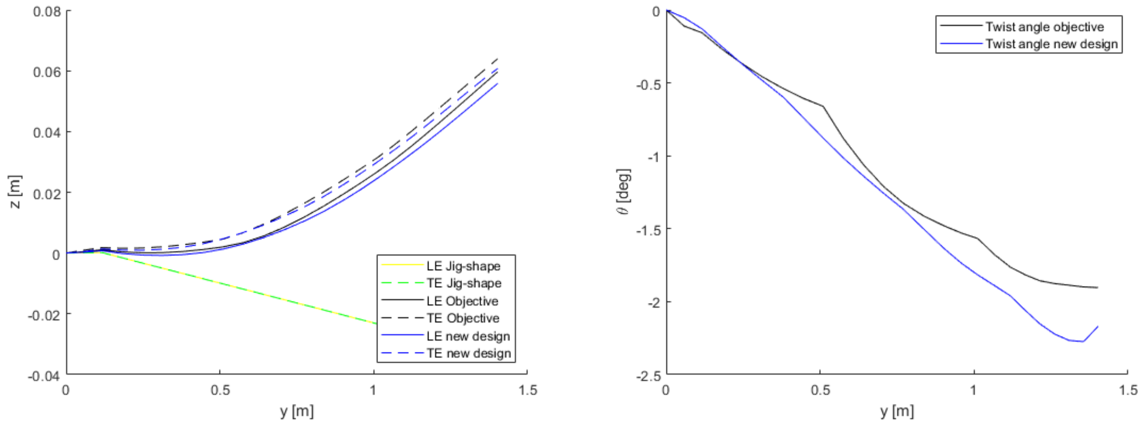

(a) Deformations (b) Twist

Figure 8.26: Aeroelastic results for the stacking sequence found after optimizing with a 4-panel cantilever wing for $k_p = 2.5$ for α = 1 degrees

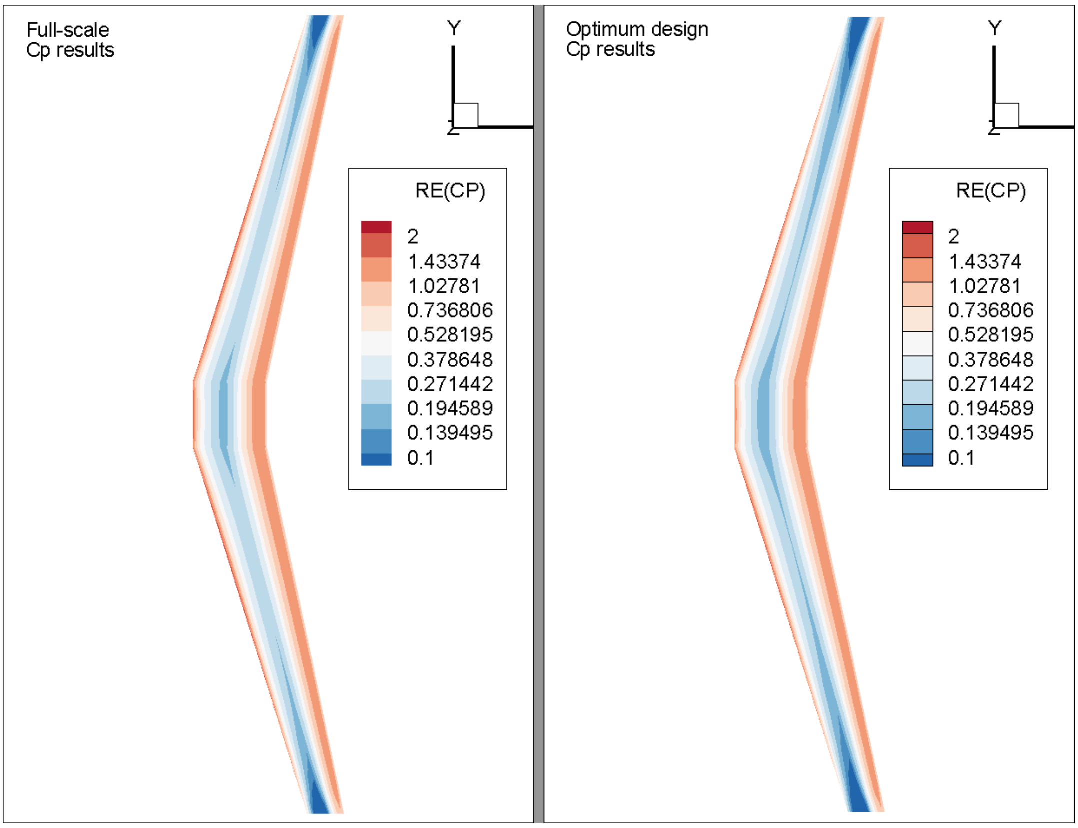

Figure 8.27: Comparison between pressure coefficients of full-scale and found optimum with the stacking sequence found after optimizing with a 4-panel cantilever wing for $k_p = 2.5$, for α = 1 degrees

8.3.2. Strut-Braced Wing

For the strut-braced wing the aeroelastic results were overall much poorer, thus finding a good structural match for all angles of attack is expected to also perform less well. The best design found was for a single panel wing at $k_p = 1.25$, as was seen in figure 8.11. This section shows how this design performs throughout the test envelope.

From figures 8.28 and 8.29 it can be seen that, even though the main wing is in general a good match for the deformations, the strut bends a lot. The strut was incorporated in the objective function but a smaller density of points was used than for the main wing, making it of lesser importance for the overall function value. From figure 8.28 it can be seen that at the joint the original wing had more nose down twist, while at the tip the optimized design had slightly more deformation.

Figures 8.30 and 8.31 show the pressure coefficients over the main wing and the strut. While the main wing seems to be a reasonable match, the strut shows significant differences. These can be explained by the fact that the strut bends and twists very differently. When zooming in on the strut in figure 8.32a, this twist difference seems small but since the chord length is also very small the change in twist is actually on average $0.45°$. Figure 8.32b shows the twists for the objective and optimum design along the span. Here it can also clearly be seen that in the middle part of the strut the difference in twist is largest, roughly $1°$, which is also where the pressure coefficient shows the largest difference in figure 8.31.

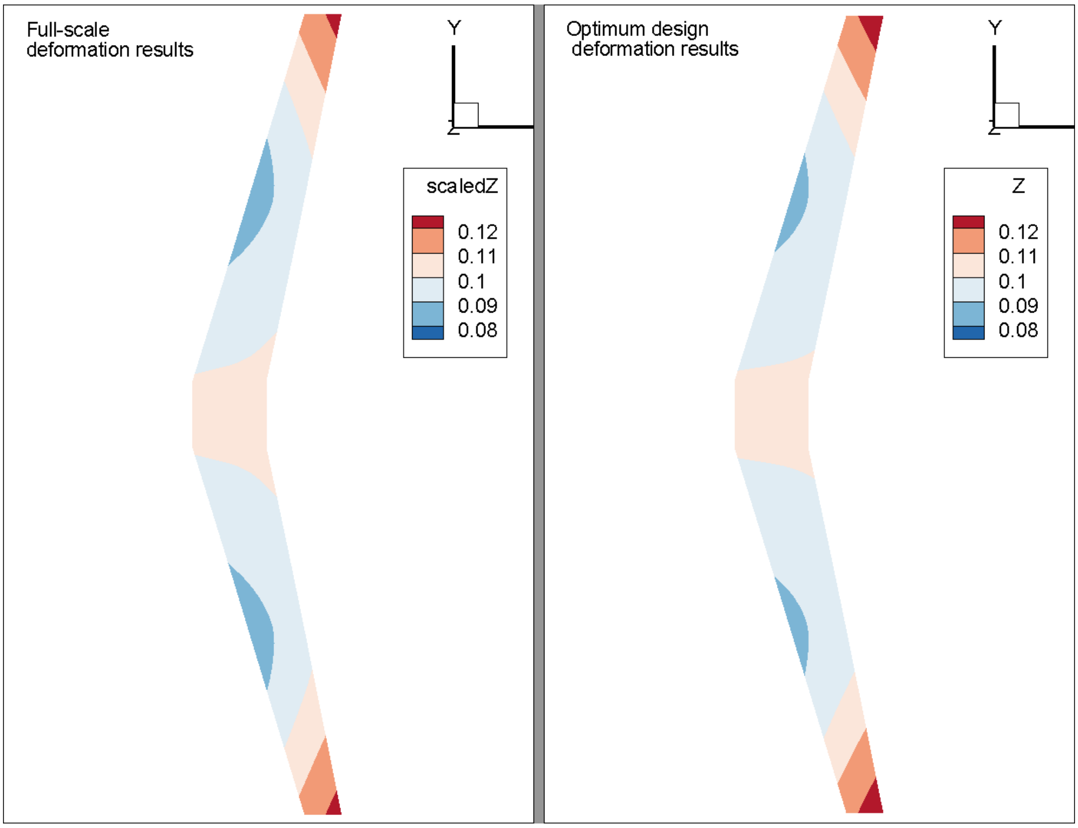

Figure 8.28: Comparison between deformations of full-scale and found optimum with the stacking sequence found after optimizing with a 1-panel strut-braced wing for $k_p = 1.25$, for α = 5 degrees

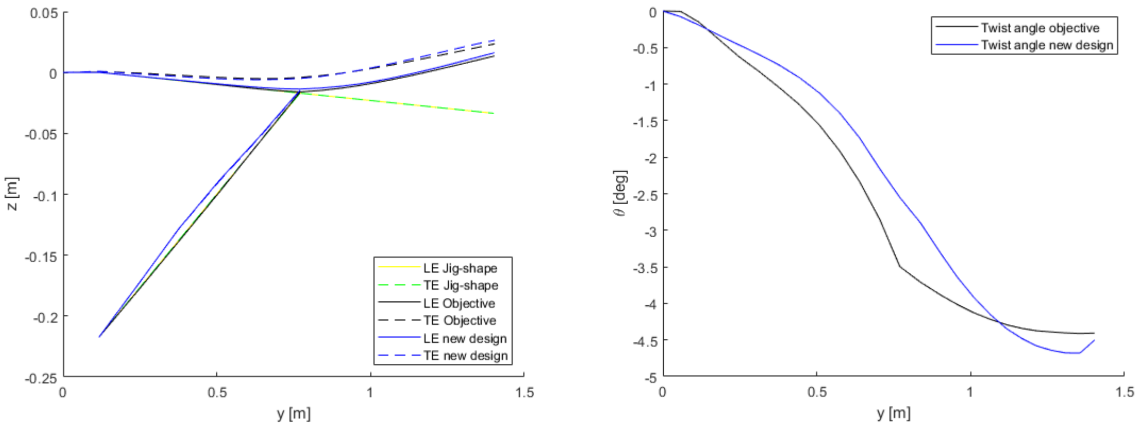

(a) Deformations (b) Twist

Figure 8.29: Aeroelastic results for the stacking sequence found after optimizing with a 1-panel strut-braced wing for $k_p = 1.25$ for α = 5 degrees

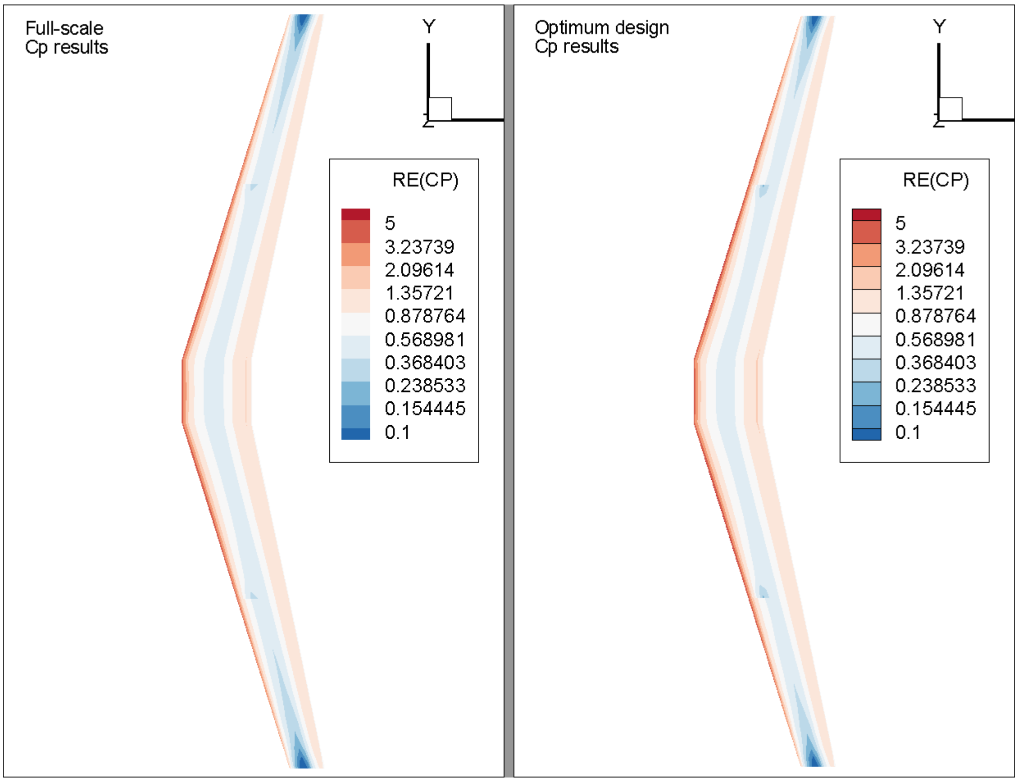

Figure 8.30: Comparison between pressure coefficients of full-scale and found optimum with the stacking sequence found after optimizing with a 1-panel strut-braced wing for $k_p = 1.25$, for α = 5 degrees

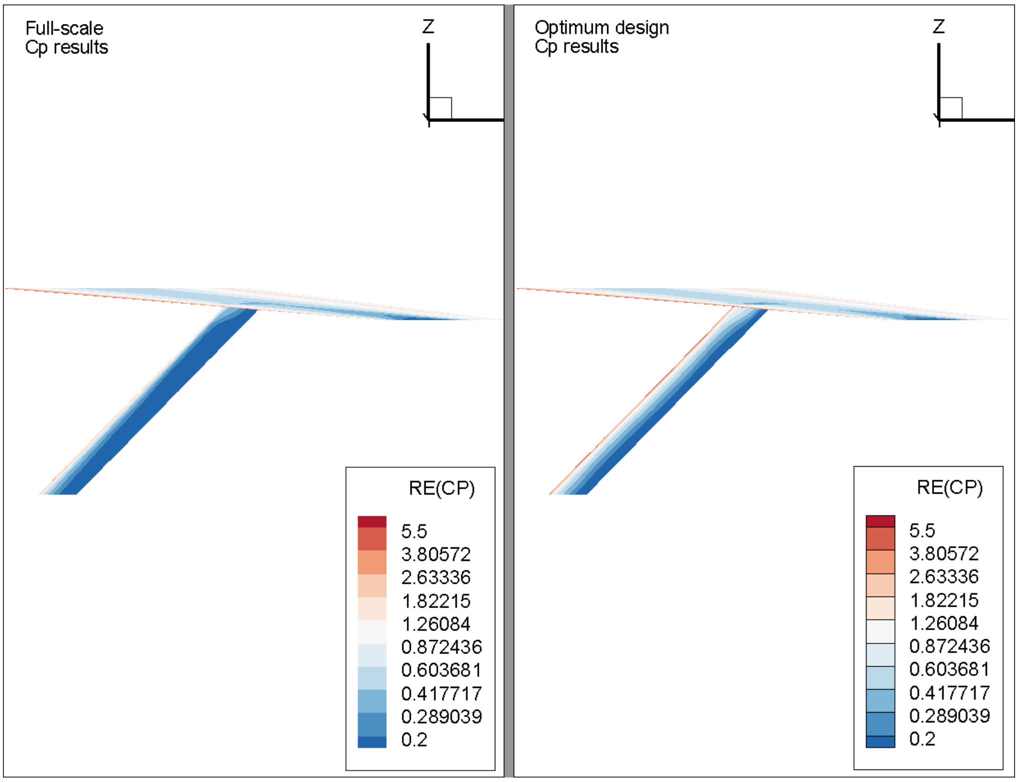

Figure 8.31: Comparison between pressure coefficients of full-scale and found optimum with the stacking sequence found after optimizing with a 1-panel strut-braced wing for $k_p = 1.25$, for α = 5 degrees. Side view of strut

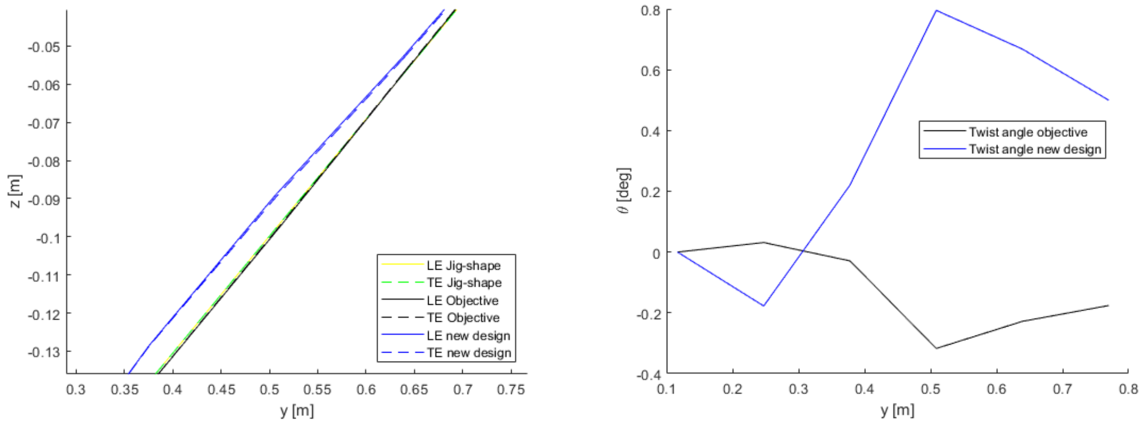

(a) Zoomed in deformations on strut

(b) Strut twist[1]

Figure 8.32: Aeroelastic results for the stacking sequence found after optimizing with a 1-panel strut-braced wing for $k_p = 1.25$ for α = 5 degrees

The overall wing aerodynamic coefficients do differ too, even though only major differences were seen on the strut and not on the main wing, which is the main contributor to the overall aerodynamics. The lift coefficient changes with 6.6% between the full-scale and optimized design results. Again, the magnitude of this difference stays roughly the same for different angles as can be seen in figure 8.33. Relatively the difference does increase for lower angles of attack.

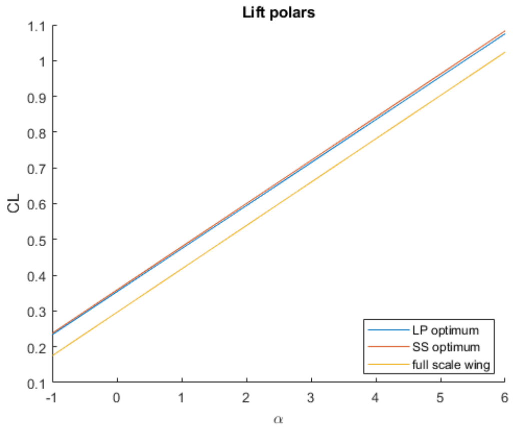

Figure 8.33: Lift polar for full-scale and found optima (LP and SS) after optimizing with a 1-panel strut-braced wing for $k_p = 1.25$

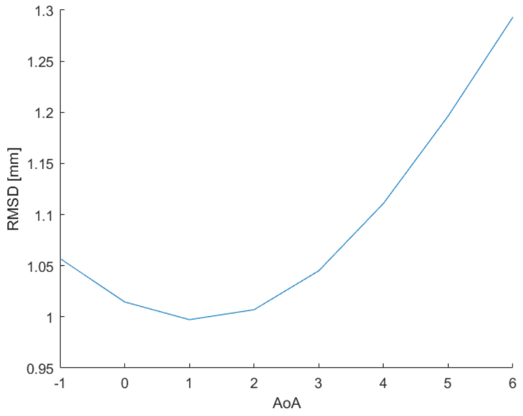

Figure 8.34: RMSD with full-scale deformation for best optimization result with a 1-panel strut-braced wing for $k_p = 1.25$

The difference in deformations for the various angles is shown in figure 8.34, which shows that the function value actually decreases for most of the other (lower) angles. While this was also the case for the specific case shown in the previous section, this also seems more inherent to the strut-braced wing design. Since the wing is held down by the strut halfway along the span this point will always be a relatively good match. For lower angles of attack, the total deformations are lower which results in smaller differences between designs. This has not been tested for all found strut-braced wing designs but the ones that were checked all showed this pattern. As an example, appendix C.2 shows the results for the 8-panel $k_p = 2.5$ results, this point had a significantly higher function value than the one shown in this section but was one of the lowest other results, the same pattern was seen here.

---

[1] Only a few points (the original node location leading and trailing edges) were considered for this plot which is why it is very coarse.

Table 8.2: ZAERO results for the optimized 1-panel strut-braced wing for $k_p = 1.25$ for α = 5 degrees

	Full-scale		Optimized design	
COEFFICIENTS	FLEXIBLE	RIGID	FLEXIBLE	RIGID
INDUCED DRAG(CDL):	0.11436	0.10641	0.11362	0.10631
DRAG AT TRIM(CD0):	0.02148	0.02148	0.02147	0.02147
LIFT(CL):	0.90256	1.21933	0.96251	1.21827
PITCH MOMENT(CM):	-0.34195	-0.48610	-0.35406	-0.48662

Again multiple angles of attack are considered to show how well the wing would match in the rest of the test envelope. Figures 8.35 to 8.38 show the deformation, twist and pressure coefficients at this angle. The deformations are still a very close match, as the bending of the strut is reduced in this case due to the lower load. It can be seen that overall there is again a slightly lower nose down twist, resulting in slightly higher forces and pressure coefficients.

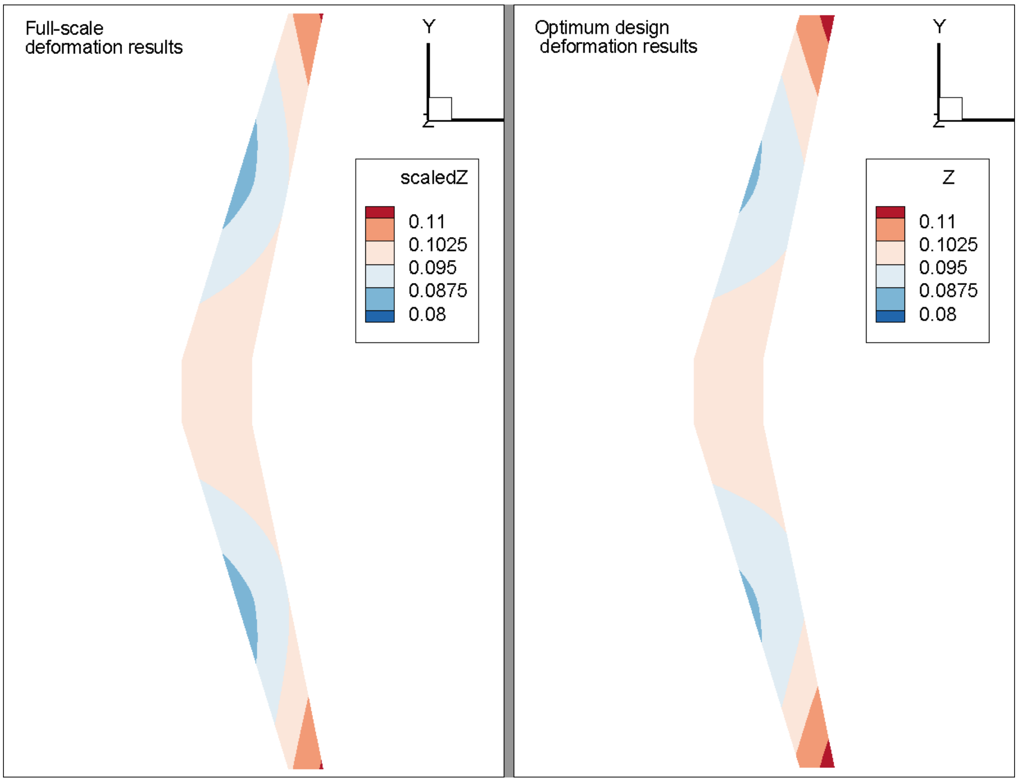

Figure 8.35: Comparison between deformations of full-scale and found optimum with the stacking sequence found after optimizing with a 1-panel strut-braced wing for $k_p = 1.25$, for α = 3 degrees

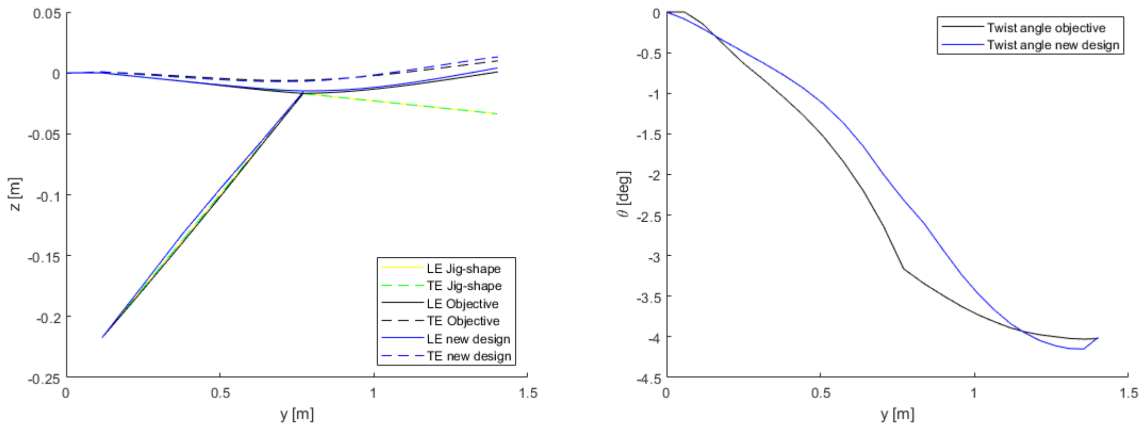

(a) Deformations (b) Twist

Figure 8.36: Aeroelastic results for the stacking sequence found after optimizing with a 1-panel strut-braced wing for $k_p = 1.25$ for α = 3 degrees

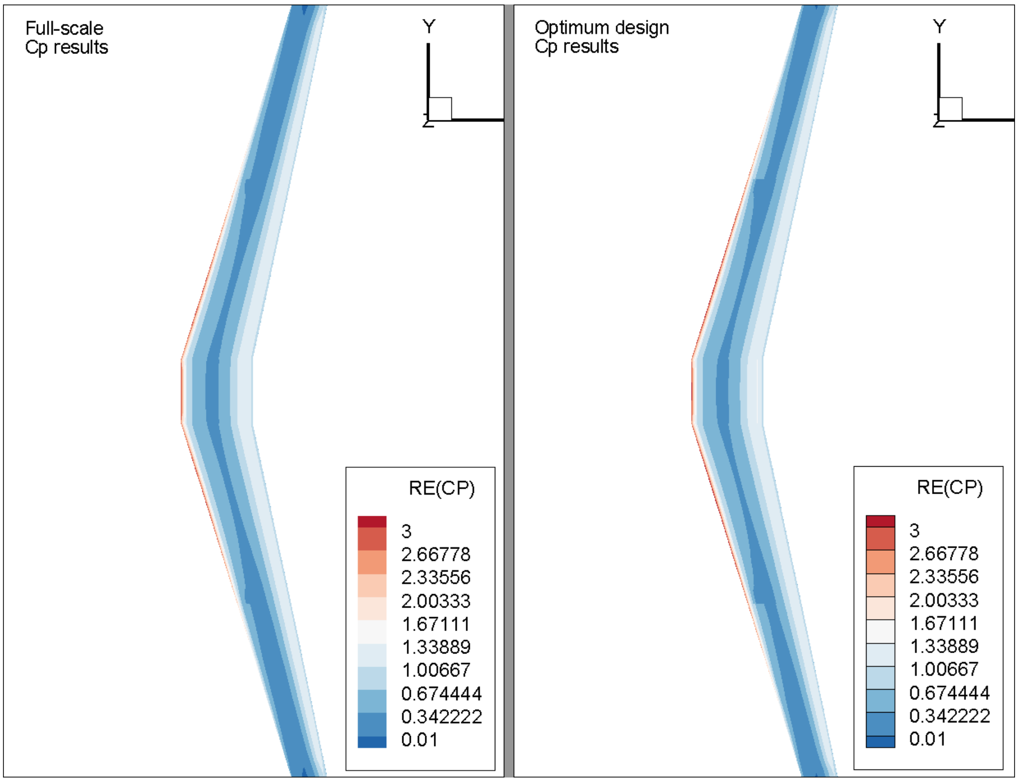

Figure 8.37: Comparison between pressure coefficients of full-scale and found optimum with the stacking sequence found after optimizing with a 4-panel strut-braced wing for $k_p = 1.25$, for α = 3 degrees

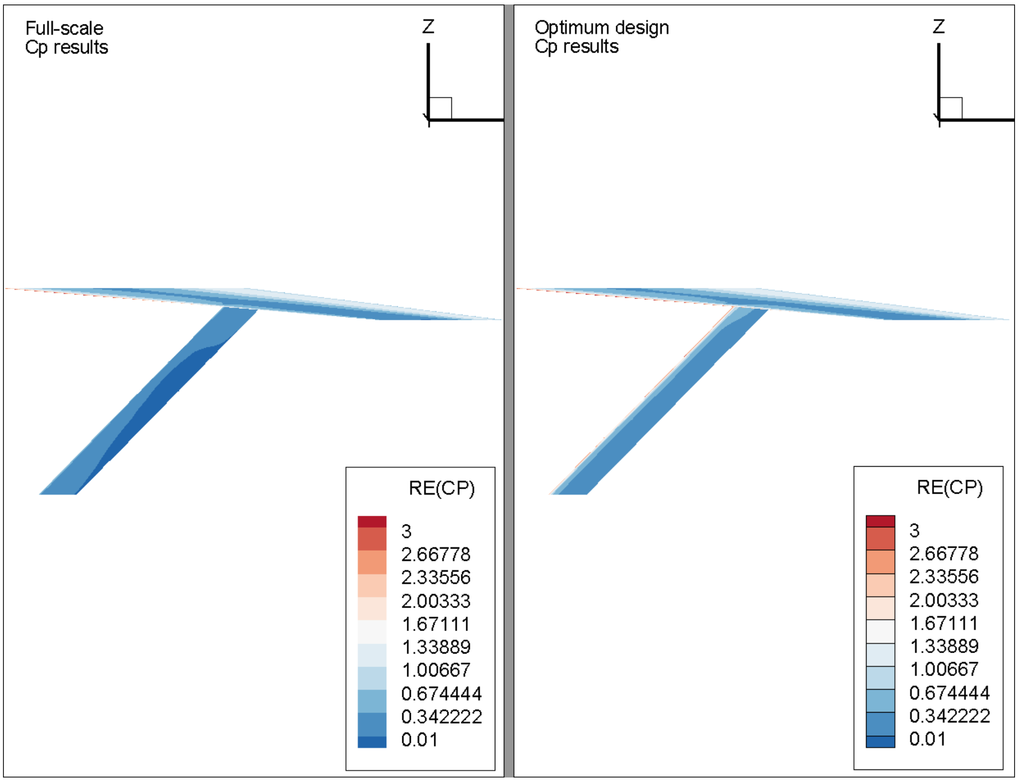

Figure 8.38: Comparison between pressure coefficients of full-scale and found optimum with the stacking sequence found after optimizing with a 4-panel strut-braced wing for $k_p = 1.25$, for α = 3 degrees. Side view of strut

For an angle of attack of 1 degree, as seen in figures 8.39 to 8.42, the results are also still matching quite closely. Still, the overall negative twist is smaller, resulting in slightly higher forces and pressure values. The lower loads result in a better matching strut.

Overall this optimum design for the strut-braced wing showed good results in the entire test envelope. Because the twist was less negative than the objective the deformations were slightly higher. This was the case for all optimized designs. Updating the objective function to include the twist may help to improve this as the strut tries to prevent further twist, especially near the strut-wing-joint.

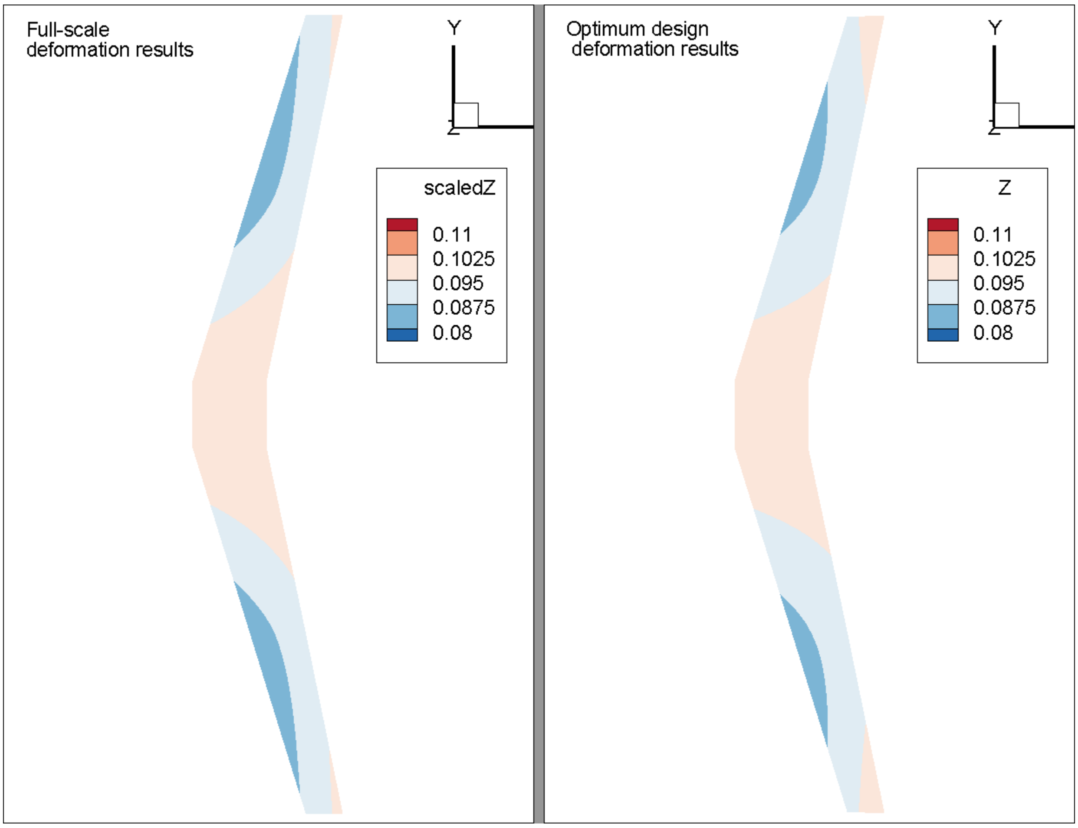

Figure 8.39: Comparison between deformations of full-scale and found optimum with the stacking sequence found after optimizing with a 1-panel strut-braced wing for $k_p = 1.25$, for α = 1 degree

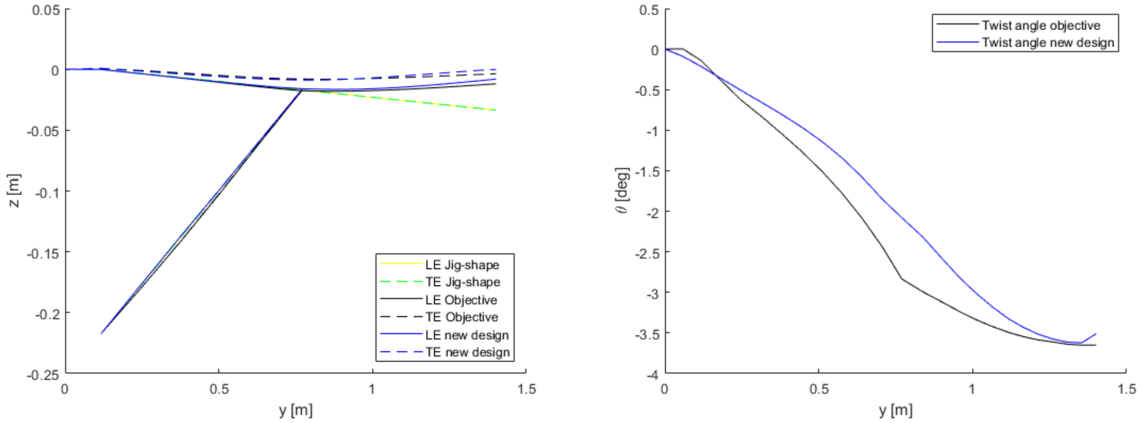

(a) Deformations

(b) Twist

Figure 8.40: Aeroelastic results for the stacking sequence found after optimizing with a 1-panel strut-braced wing for $k_p = 1.25$ for α = 1 degree

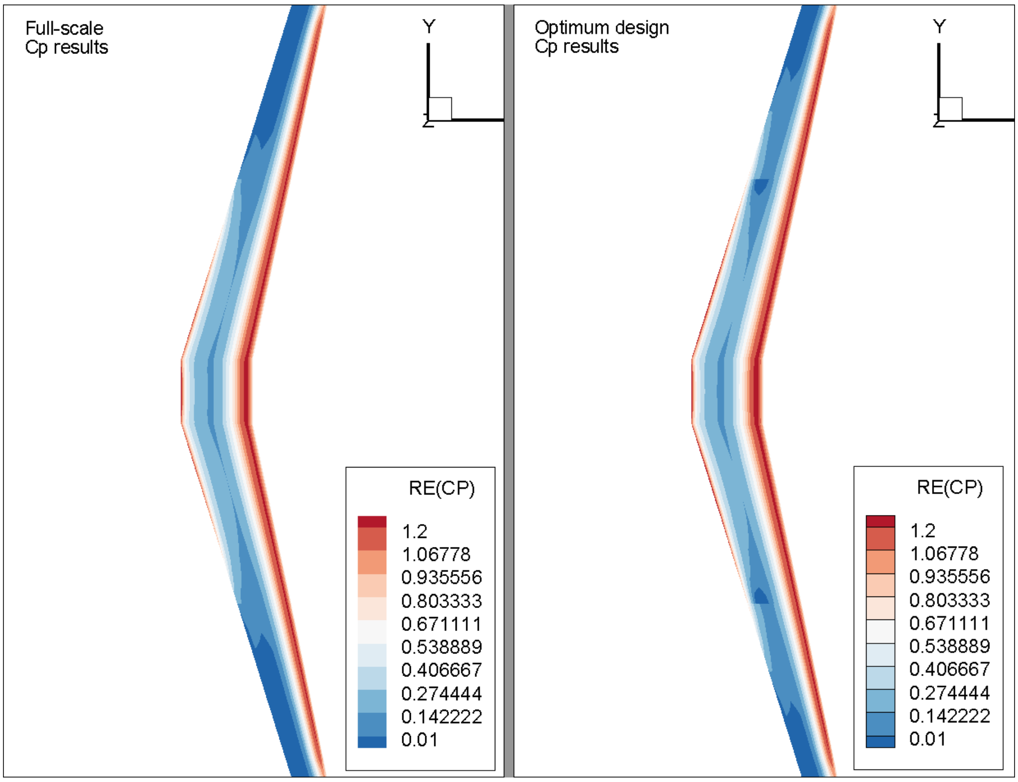

Figure 8.41: Comparison between pressure coefficients of full-scale and found optimum with the stacking sequence found after optimizing with a 4-panel strut-braced wing for $k_p = 1.25$, for α = 1 degree

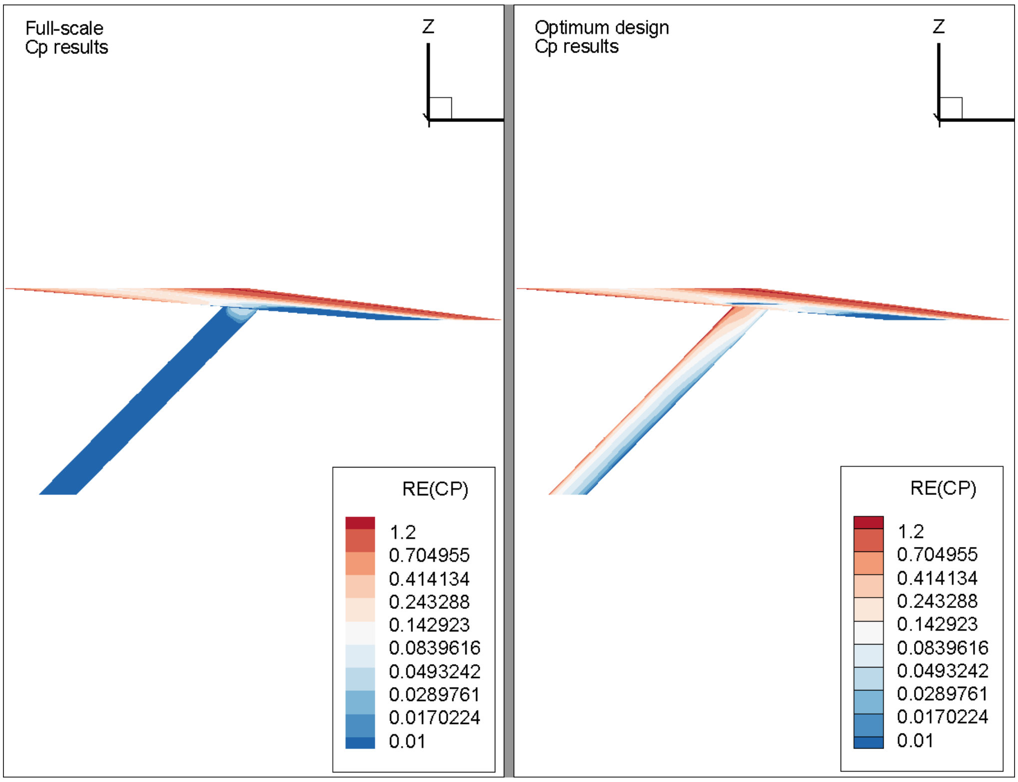

Figure 8.42: Comparison between pressure coefficients of full-scale and found optimum with the stacking sequence found after optimizing with a 4-panel strut-braced wing for $k_p = 1.25$, for α = 1 degree. Side view of strut

9

Conclusions

This thesis developed an optimization framework for the design of a composite shell static aeroelastically scaled wind tunnel model which represents the aeroelastic characteristics of a full-scale reference model. Such models are needed for the aeroelastic wind tunnel testing of flexible wings, as this allows the aerodynamic performance to be evaluated in the actual flight shape rather than for a jig shape only. Two wing concepts were analyzed, the non-conventional strut-braced wing from the H2020 AGILE project and a cantilever version of the same wing. This wing is very slender and thin, leaving little room for structural components, which was the reason for the composite shell concept. A bi-step optimization framework was chosen, where the first step optimizes the laminate in the continuous lamination parameter space and the second step retrieves a stacking sequence that most closely matches the found parameters. The lamination parameter optimization is done for a single angle of attack and by using a static FEM analysis in the optimization loop. This was done as it greatly reduces the computational effort required, as opposed to using a multi-objective (multi angle of attack) and/or aeroelastic analysis. If a proper match is found, the static and aeroelastic result should become the same and should then also match for all angles. The second optimization step was performed using an open-source tool, OptiBless, which uses a genetic algorithm to find laminates that best match the found lamination parameters. The optimization framework was analyzed for varying numbers of laminate panels and for varying starting points.

9.1. Conclusions

It was found that the optimization framework performed well for the cantilever wing. The optimal designs found in the continuous lamination space were matching very closely in terms of deformation when multiple laminate panels were used. The optimization framework was consistent in finding matching designs in the lamination parameter space for the cantilever wing.

The twist difference that is present after optimization using a static force has a large influence on the aeroelastic result found with that optimized design. If the leading edge was slightly higher and the trailing edge slightly lower this would increase the deformation of the wing for the aeroelastic sum. A result with the same RMSD of the deformations in which both the leading and trailing edge were very slightly more upwards would not see this change in the aeroelastic step.

For the cantilever wing, the biggest variations were caused by the stacking sequence retrieval step. A feasible laminate can either be close or far from the found lamination parameters. Still, the optimization framework was capable of finding stacking sequences that resulted in a good overall match. For the stacking sequence retrieval step, it was found useful that thicker laminates are used as this creates a larger design space. Thus, using higher pressure scaling factors is favorable for this reason. The stacking sequence retrieval step was handled by an open-source tool and was not specifically altered for the purpose of this research. Not all manufacturing design rules were turned on in OptiBless. This means some retrieved stacking sequences may not adhere to all design rules, such as having a maximum number of plies in the same direction in a row. At the same time, the ply angles were restricted to only 45 degree steps, this could be lowered and still be relatively easy to manufacture.

For the strut-braced wing, it was found that the continuous lamination parameter optimization step was inconsistent in finding matching designs. It was found that this was due to non-convexities in the objective function. While these were also present in the cantilever wing, those optimizations converged to the same optimum much more often. Furthermore, those runs that were unable to find the global optimum were very close to it. A multi-start optimization could make it much more likely the global optimum is found, however, it would significantly increase the computational costs. In this thesis, eleven different starting points were chosen manually and two converged to the same minimum point for the strut-braced wing, it is, however, unknown whether this point is the global optimum. Using more than eleven starting points would be even better to make sure a global optimum is found.

For the strut-braced wing a matching design was still found after stacking sequence retrieval but finding it with the developed framework is not guaranteed and can take a lot of time.

It was also found that the strut of the strut-braced wing had to be incredibly stiff in order to hold the wing down enough, which caused the thickness of the strut's laminate to converge towards the upper bound. This might, however, be inherent to the chosen reference wing, which had an already very stiff full-scale strut. In the general sense, however, a full-scale reference wing that already uses a lot of material volume in its design may not be fit for static aeroelastic scaling.

9.2. Recommendations

Based on the results of this thesis several recommendations can be made. Recommendations are made in this section for changes in the optimization framework and future research related to this topic.

A clear requirement on how well a design has to elastically match to be sufficient in wind tunnel testing was not found. Investigations into this and the incorporation of correction models in the wind tunnel testing will have to be analyzed and validated in future research.

It should be investigated whether incorporating the twist angle in the objective function leads to designs that will have a better match between the static and aeroelastic results. Incorporating an aeroelastic sum directly within the optimization loop may also be beneficial if computation-time is not a large concern. Using a multi-objective optimization, to incorporate multiple angles of attack within the optimization loop, will also lead to better the results but would increase computation time.

The stacking sequence step caused large differences between the optimum designs found in the lamination parameter optimizations and the final designs with retrieved stacking sequences. The tool was run only once to get the results shown in this thesis, while, due to the random nature of the genetic algorithm, it was found that a better point is sometimes found when running again. For larger panel numbers in particular this could make a difference. Furthermore, the settings used by the stacking sequence retrieval step should be investigated, many manufacturing constraints were turned off at this point. Increasing the ply angle possibilities, however, may aid this step, as in this thesis 45 degree steps were used.

The strut-braced wing optimizations seemed to get stuck in local optima. It would be interesting to investigate if this is inherent to the strut-braced wing design for other types of optimization studies as well. Another possible cause is the specific combination of a composite shell and the strut-braced wing, it therefore would be interesting to investigate different model concepts.

Since the strut-braced wing optimizations are highly non-convex, investigating the use discrete optimizers to optimize strut-braced wing designs could be of interest. Investigations into different optimization strategies not priorly used for these types of optimizations, such as using surrogate models, could also be an interesting topic for future research.

Varying the degrees of freedom while doing the multiple start point analysis may be useful to confirm the best option. It is possible that the ball-joint options are even more convex and therefore seemed to perform worse than the completely rigid design, while actually capable of being better if the true global optimum would be found.

References

[1] J. Heeg, C. Spain, and J. Rivera, “Wind Tunnel to Atmospheric Mapping for Static Aeroelastic Scaling,” in *45th AIAA/ASME/ASCE/AHS/ASC Structures, Structural Dynamics & Materials Conference*, (Palm Springs, California), American Institute of Aeronautics and Astronautics, Apr. 2004.

[2] AGILE-Project, “Strut Braced Wing Design.” `https://i2.wp.com/www.agile-project.eu/wp-content/uploads/2018/11/4.1_sbw_trans-e1543484092443.png`.

[3] R. Michele, “Nasa is studing Truss-Braced Wings | Aerospace Engineering.” http://www.aerospacengineering.net/nasa-is-studing-truss-braced-wings/, Apr. 2016.

[4] H. Schlichting and J. Kestin, *Boundary-layer theory*. McGraw-Hill, Inc., 1979.

[5] H. Blasius, “The boundary layers in fluids with little friction,” *Zeitschrift fuer Mathematik und Physik*, no. 56, pp. 1–37, 1950.

[6] L. Prandtl, “The mechanics of viscous fluids,” *Aerodynamic theory*, vol. 3, pp. 155–162, 1935.

[7] L. Prandtl and H. Schlichting, “Das widerstandsgesetz rauher platten,” *Werft, Reederei, Hafen*, vol. 15, no. 1, p. 4, 1934.

[8] F. Schultz-Grunow, “Neues Reibungswider-staandsgesetz fur Glatte Platten,” *NACA TM 986*, 1941.

[9] P. H. Park, “Fuel Consumption of a Strutted vs Cantilever-Winged Short-Haul Transport with Aeroelastic Considerations,” *Journal of Aircraft*, vol. 17, pp. 856–860, Dec. 1980.

[10] T. Allen, B. Sexton, and M. J. Scott, “SUGAR Truss Braced Wing Full Scale Aeroelastic Analysis and Dynamically Scaled Wind Tunnel Model Development,” in *56th AIAA/ASCE/AHS/ASC Structures, Structural Dynamics, and Materials Conference*, (Kissimmee, Florida), American Institute of Aeronautics and Astronautics, Jan. 2015.

[11] M. K. Bradley and C. K. Droney, “Subsonic Ultra Green Aircraft Research: Phase I Final Report,” *NASA STI*, p. 207, Apr. 2011.

[12] M. K. Bradley, “Subsonic Ultra Green Aircraft Research: Phase II Final Report,” *NASA STI*, p. 87, Apr. 2014.

[13] C. K. Droney, “SUGAR sweetens the deal with Phase 3 results, Phase 4 underway.” http://www.boeing.com/features/innovation-quarterly/aug2017/feature-technical-sugar.page, Aug. 2017.

[14] F. H. Gern, A. H. Naghshineh-Pour, E. Sulaeman, R. K. Kapania, and R. T. Haftka, “Structural Wing Sizing for Multidisciplinary Design Optimization of a Strut-Braced Wing,” *Journal of Aircraft*, vol. 38, pp. 154–163, Jan. 2001.

[15] N. Wood, “Strut Braced Wings - A challenge or an opportunity?.” `https://www.scipedia.com/wd/images/6/6d/Draft_Pons_Prats_410517650-4080-document.pdf`, Nov. 2017.

[16] I. Lee, “Aeroelasticity Research and Development Activities in Korea,” in *50th AIAA/ASME/ASCE/AHS/ASC Structures, Structural Dynamics, and Materials Conference*, (Palm Springs, California), American Institute of Aeronautics and Astronautics, May 2009.

[17] F. Afonso, J. Vale, E. Oliveira, F. Lau, and A. Suleman, “A review on non-linear aeroelasticity of high aspect-ratio wings,” *Progress in Aerospace Sciences*, vol. 89, pp. 40–57, Feb. 2017.

[18] R. C. Scott, T. Allen, M. Castelluccio, B. Sexton, S. Claggett, J. R. Dykman, C. Funk, D. Coulson, and R. E. Bartels, “Aeroservoelastic Wind-Tunnel Test of the SUGAR Truss Braced Wing Wind-Tunnel Model,” in *56th AIAA/ASCE/AHS/ASC Structures, Structural Dynamics, and Materials Conference*, (Kissimmee, Florida), American Institute of Aeronautics and Astronautics, Jan. 2015.

[19] J. M. Coggin, R. K. Kapania, J. A. Schetz, H. Vijayakumari, and W. Zhao, “Nonlinear Aeroelastic Analysis of a Truss Based Wing Aircraft,” in *55th AIAA/ASME/ASCE/AHS/ASC Structures, Structural Dynamics, and Materials Conference*, (National Harbor, Maryland), American Institute of Aeronautics and Astronautics, Jan. 2014.

[20] J. Ran, “Aeroelastic Tailoring of Strut-Braced Wings,” tech. rep., Delft University Of Technology, May 2017.

[21] E. Sulaeman, *Effect of Compressive Force on Aeroelastic Stability of a Strut-Braced Wing*. PhD thesis, Virginia Polytechnic Institute and State University, Blacksburg, Virginia, USA, Jan. 2002.

[22] M. Bhatia, R. K. Kapania, and R. T. Haftka, “Structural and Aeroelastic Characteristics of Truss-Braced Wings: A Parametric Study,” *Journal of Aircraft*, vol. 49, pp. 302–310, Feb. 2012.

[23] I. Chakraborty, T. Nam, J. R. Gross, D. N. Mavris, J. A. Schetz, and R. K. Kapania, “Comparative Assessment of Strut-Braced and Truss-Braced Wing Configurations Using Multidisciplinary Design Optimization,” *Journal of Aircraft*, vol. 52, pp. 2009–2020, Nov. 2015.

[24] A. H. Naghshineh-Pour, *Structural Optimization and Design of a Strut-Braced Wing Aircraft*. PhD thesis, Virginia Tech, Nov. 1998.

[25] “AGILE.” https://www.agile-project.eu/.

[26] AGILE-Project, “Use Case – Strut-Braced Wing – AGILE.” https://www.agile-project.eu/use-case-strut-braced-wing/.

[27] R. L. Bisplinghoff, H. Ashley, and R. L. Haltman, *Aeroelasticity*. Cambridge, MA. USA: Addison-Wesley Publishing Company, Inc., 1955.

[28] A. R. Collar, “The expanding domain of aeroelasticity,” *The Aeronautical Journal*, vol. 50, no. 428, pp. 613–636, 1946.

[29] S. Hulshoff, “AE4930 Aeroelasticity (course reader),” 2012.

[30] “ZAERO Version 9.2 Theoretical Manual,” Nov. 2016.

[31] D. Mook and A. Nayfeh, “Numerical simulations of dynamic/aerodynamic interactions,” *Computing Systems in Engineering*, vol. 1, pp. 461–482, Jan. 1990.

[32] C. Xie, Y. Liu, C. Yang, and J. E. Cooper, “Geometrically Nonlinear Aeroelastic Stability Analysis and Wind Tunnel Test Validation of a Very Flexible Wing,” *Shock and Vibration*, vol. 2016, pp. 1–17, 2016.

[33] J. Hooker, A. Burner, R. Valla, J. Hooker, A. Burner, and R. Valla, “Static aeroelastic analysis of transonic wind tunnel models using finite element methods,” in *15th Applied Aerodynamics Conference*, (Atlanta,GA,U.S.A.), American Institute of Aeronautics and Astronautics, June 1997.

[34] M. Baker, R. Mendoza, and P. Hartwich, “Transonic aeroelastic analysis of a high speed transport wind tunnel model,” in *40th Structures, Structural Dynamics, and Materials Conference and Exhibit*, (St. Louis,MO,U.S.A.), American Institute of Aeronautics and Astronautics, Apr. 1999.

[35] Z. Wan and C. E. Cesnik, “Geometrically Nonlinear Aeroelastic Scaling for Very Flexible Aircraft,” in *54th AIAA/ASME/ASCE/AHS/ASC Structures, Structural Dynamics, and Materials Conference*, (Boston, Massachusetts), American Institute of Aeronautics and Astronautics, Apr. 2013.

[36] E. Ting, S. Lebofsky, N. T. Nguyen, and K. V. Trinh, “Static Aeroelastic Scaling and Analysis of a Sub-Scale Flexible Wing Wind Tunnel Model,” in *55th AIAA/ASME/ASCE/AHS/ASC Structures, Structural Dynamics, and Materials Conference*, (National Harbor, Maryland), American Institute of Aeronautics and Astronautics, Jan. 2014.

[37] R. C. Hibbeler, *Mechanics of materials*. Upper Saddle River, N.J.: Pearson Education, 2003.

[38] Kallog, “TorsionConstantBar.png.” `https://en.wikipedia.org/wiki/Torsion_constant`.

[39] M. H. Shirk, T. J. Hertz, and T. A. Weisshaar, “Aeroelastic tailoring - Theory, practice, and promise,” *Journal of Aircraft*, vol. 23, pp. 6–18, Jan. 1986.

[40] M. M. Munk, “Propeller containing diagonally disposed fibrous material,” US Patent 2,484,308, Oct. 1949.

[41] G. Wang, J. Zeng, and J.-D. Lee, “Preliminary Design of a Truss-Braced Natural-Laminar-Flow Composite Wing via Aeroelastic Tailoring,” *Journal of Aeroelasticity and Structural Dynamics*, pp. 1–17, Sept. 2015.

[42] D. Rajpal, R. D. Breuker, H. Timmermans, W. F. Lammen, and F. Torrigiani, “Including aeroelastic tailoring in the conceptual design process of a composite strut braced wing,” in *Proceedings of the 31st Congress of the International Council of the Aeronautical Sciences*, (Belo Horizonte, Brazil), p. 12, Sept. 2018.

[43] S. Guo, W. Cheng, and D. Cui, “Aeroelastic Tailoring of Composite Wing Structures by Laminate Layup Optimization,” *AIAA Journal*, vol. 44, pp. 3146–3150, Dec. 2006.

[44] C. Kassapoglou, *Design and Analysis of Composite Structures : With Applications to Aerospace Structures*. Somerset, UNITED KINGDOM: John Wiley & Sons, Incorporated, 2013.

[45] R. Creemers, “Personal Interview,” Aug. 2019.

[46] “Design Guidelines.” http://www.ist.edu.pk/downloads/amss/lecturers/design-guidelines.pdf.

[47] J. van Campen, O. Seresta, M. Abdalla, and Z. Gürdal, “General Blending Definitions for Stacking Sequence Design of Composite Laminate Structures,” in *49th AIAA/ASME/ASCE/AHS/ASC Structures, Structural Dynamics, and Materials Conference
 16th AIAA/ASME/AHS Adaptive Structures Conference
 10t*, (Schaumburg, IL), American Institute of Aeronautics and Astronautics, Apr. 2008.

[48] D. B. Adams, L. T. Watson, Z. Gürdal, and C. M. Anderson-Cook, “Genetic algorithm optimization and blending of composite laminates by locally reducing laminate thickness,” *Advances in Engineering Software*, vol. 35, pp. 35–43, Jan. 2004.

[49] S. Tsai and N. Pagano, *Invariant Properties of Composite Materials*. Defense Technical Information Center, 1968.

[50] C. G. Diaconu, M. Sato, and H. Sekine, “Feasible Region in General Design Space of Lamination Parameters for Laminated Composites,” *AIAA Journal*, vol. 40, pp. 559–565, Mar. 2002.

[51] M. Bloomfield, C. Diaconu, and P. Weaver, “On feasible regions of lamination parameters for lay-up optimization of laminated composites,” *Proceedings of the Royal Society A: Mathematical, Physical and Engineering Sciences*, vol. 465, pp. 1123–1143, Apr. 2009.

[52] M. Kameyama and H. Fukunaga, “Optimum design of composite plate wings for aeroelastic characteristics using lamination parameters,” *Computers & Structures*, vol. 85, pp. 213–224, Feb. 2007.

[53] J. L. Grenestedt and P. Gudmundson, “Layup optimization of composite material structures,” *Optimal design with advanced materials*, pp. 311–336, 1993.

[54] G. Georgiou, G. A. Vio, and J. E. Cooper, “Aeroelastic tailoring and scaling using Bacterial Foraging Optimisation,” *Structural and Multidisciplinary Optimization*, vol. 50, pp. 81–99, July 2014.

[55] J. K. S. Dillinger, M. M. Abdalla, Y. M. Meddaikar, and T. Klimmek, “Static aeroelastic stiffness optimization of a forward swept composite wing with CFD-corrected aero loads,” *CEAS Aeronautical Journal*, May 2019.

[56] T. A. Dutra and S. F. M. de Almeida, “Composite plate stiffness multicriteria optimization using lamination parameters,” *Composite Structures*, vol. 133, pp. 166–177, Dec. 2015.

[57] H. T. Hahn and S. W. Tsai, *Introduction to Composite Materials*. Taylor & Francis, 1980.

[58] C. G. Diaconu and H. Sekine, “Layup Optimization for Buckling of Laminated Composite Shells with Restricted Layer Angles,” *AIAA Journal*, vol. 42, pp. 2153–2163, Oct. 2004.

[59] H. Fukunaga and H. Sekine, “Stiffness design method of symmetric laminates using lamination parameters,” *AIAA Journal*, vol. 30, pp. 2791–2793, Nov. 1992.

[60] T. Macquart, M. T. Bordogna, P. Lancelot, and R. De Breuker, “Derivation and application of blending constraints in lamination parameter space for composite optimisation,” *Composite Structures*, vol. 135, pp. 224–235, Jan. 2016.

[61] T. Macquart, N. Werter, and R. De Breuker, “Aeroelastic Tailoring of Blended Composite Structures using Lamination Parameters,” in *57th AIAA/ASCE/AHS/ASC Structures, Structural Dynamics, and Materials Conference*, (San Diego, California, USA), American Institute of Aeronautics and Astronautics, Jan. 2016.

[62] F. Vicente, “Stacking Sequence Retrieval of Large Com- posite Structures in Bi-step Optimization Strategies Using Mechanical Constraints,” tech. rep., Delft University Of Technology, Delft, 2019.

[63] T. Macquart, “User Manual optiBless,” 2015.

[64] A. Schumacher, T. Vietor, S. Fiebig, K.-U. Bletzinger, and K. Maute, eds., *Advances in Structural and Multidisciplinary Optimization*. Cham: Springer International Publishing, 2018.

[65] E. U. A. S. A. (EASA), “CS-25 Certification Specifications and Acceptable Means of Compliance for Large Aeroplanes.”

[66] D. Rajpal, “Personal Interview,” Jan. 2020.

[67] MSCSoftware, “Dynamic Analysis User’s Guide,” *MSC Nastran 2018.2*, p. 857, 2018.

[68] A. Moosfeld, “NASTRAN 2019 Aeroelastic Analysis User’s Guide,” 2019.

[69] M. Koobs, “Topology optimized design of a strut- braced wing for fibre reinforced additive manufacturing,” tech. rep., Netherlands Aerospace Centre, June 2019.

A

CFD Plots

This appendix shows additional angles of attack, that where computed to show the effect of a change in Reynolds number, as discussed in section 4.2. All figures are for M=0.78 at cruise conditions for the full-scale results and same mach number but scaled Reynolds number flow for lowered Reynolds number results. The mesh between both CFD results was the same as only the flow conditions and not the grid was scaled.

Top figures show lowered Reynolds number, **bottom** shows full scale results. **Left** figures show pressure distribution over top surface in Pascals, **middle** shows the pressure distribution over the bottom surface in Pascals and the **right** figure shows the deformations in meters.

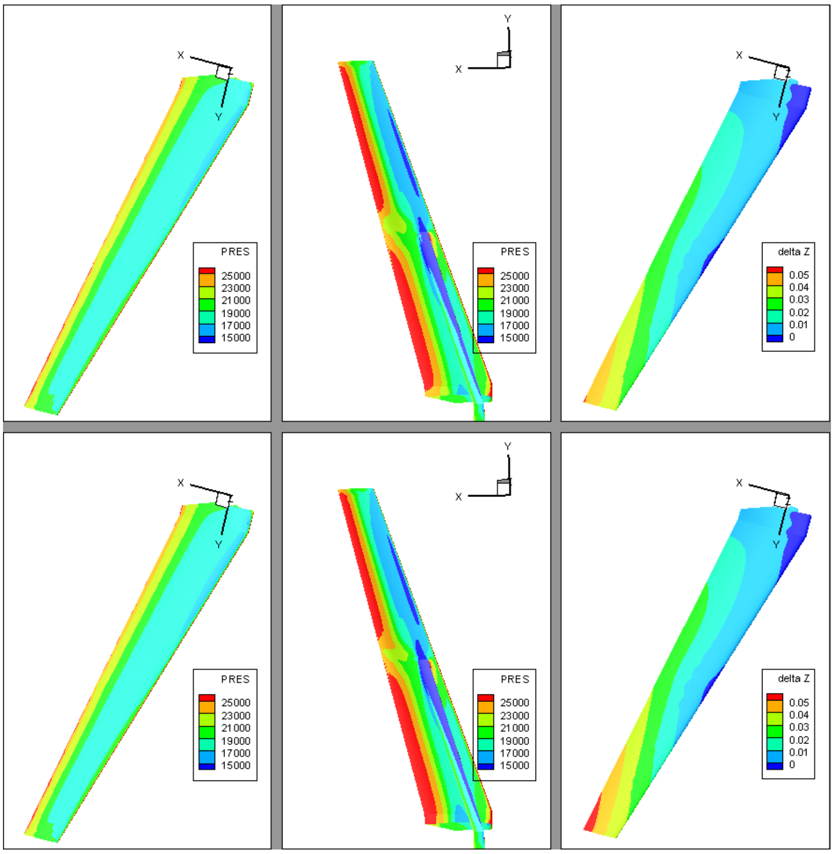

Figure A.1: CFD results for $\alpha = -2.5°$

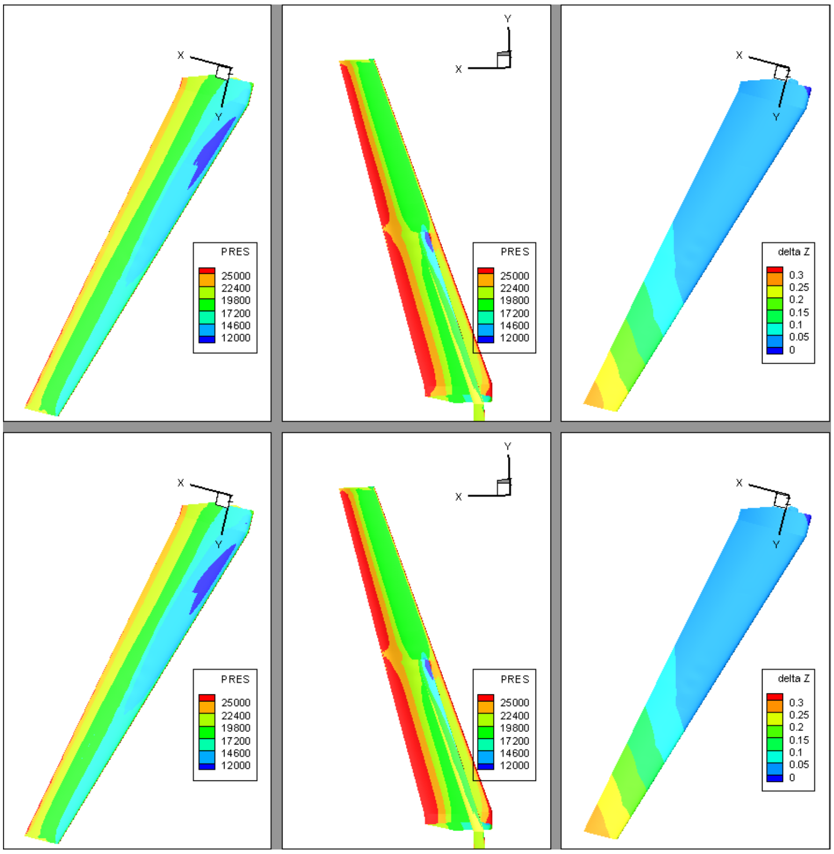

Figure A.2: CFD results for $\alpha = 0^\circ$

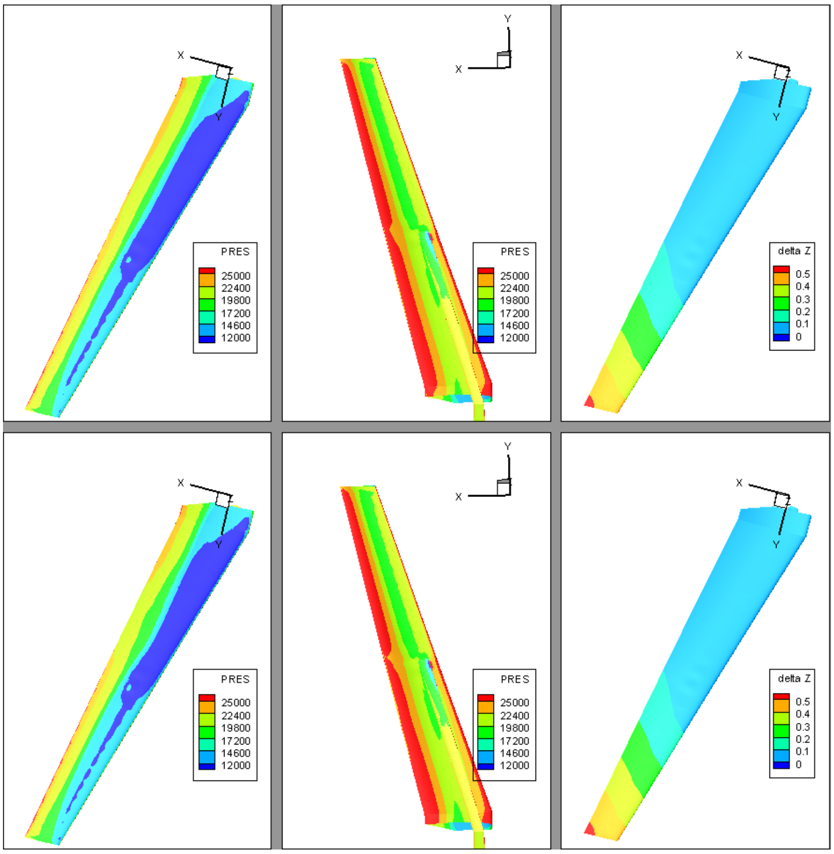

Figure A.3: CFD results for $\alpha = 2.5^\circ$

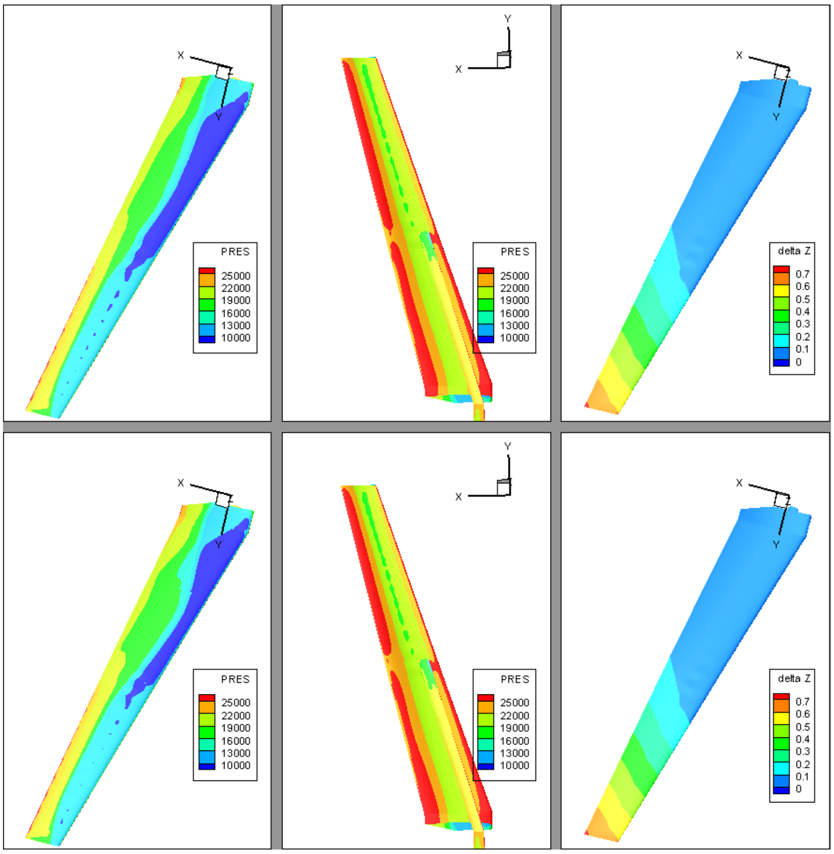

Figure A.4: CFD results for $\alpha = 5^{\circ}$

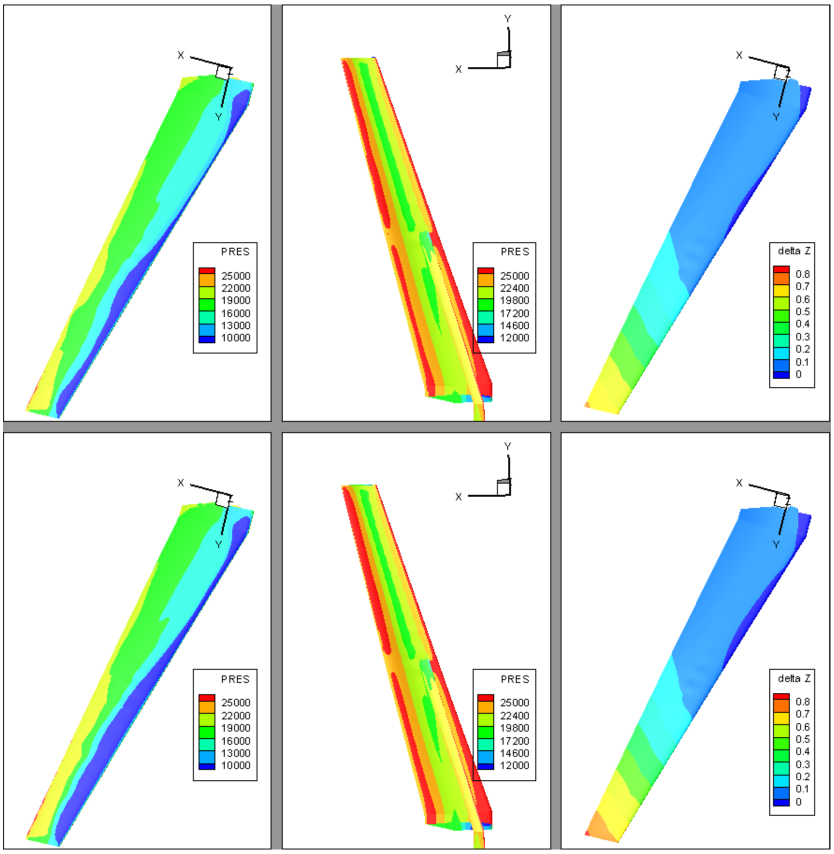

Figure A.5: CFD results for $\alpha = 7.5^{\circ}$

B

Program Diagrams

This appendix shows diagrams that contain the structure of the MATLAB program(s) used in this thesis research. The legend, in figure B.1, shows the meaning of each type of box; input, functions, intermediate data and output and also text files that are used by the solvers used in this thesis. The orange boxes in the general overview, seen in figure B.2, correspond to the separate diagrams that explain that specific function further.

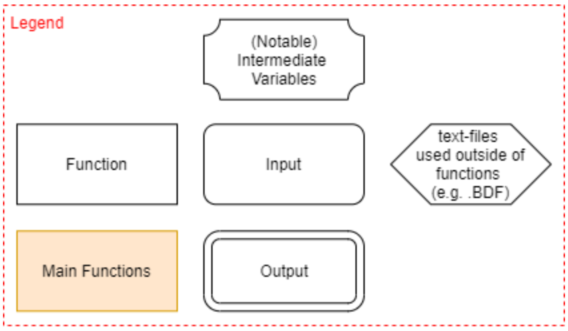

Figure B.1: Legend for the program overview figures

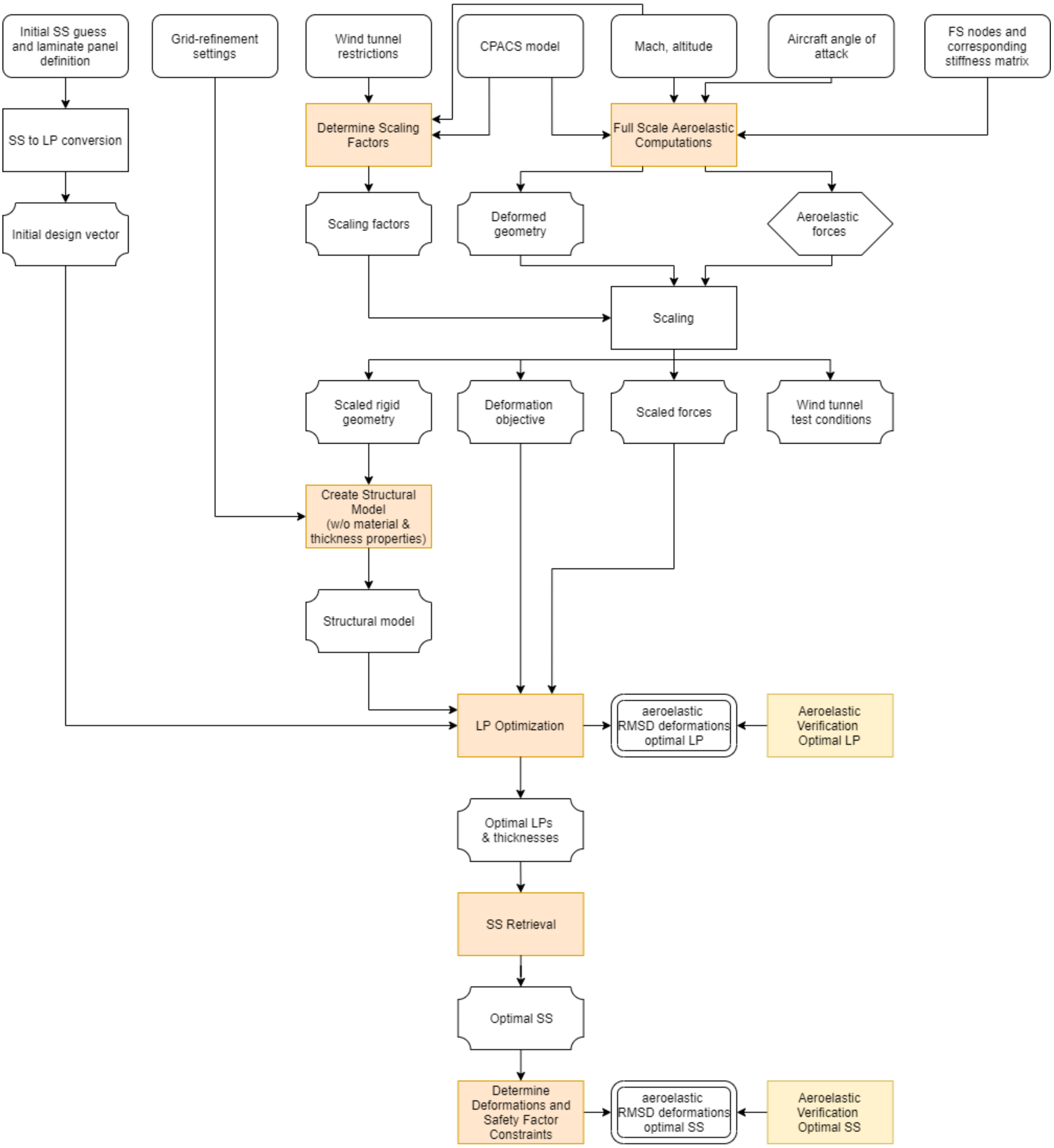

Figure B.2: General overview of the steps

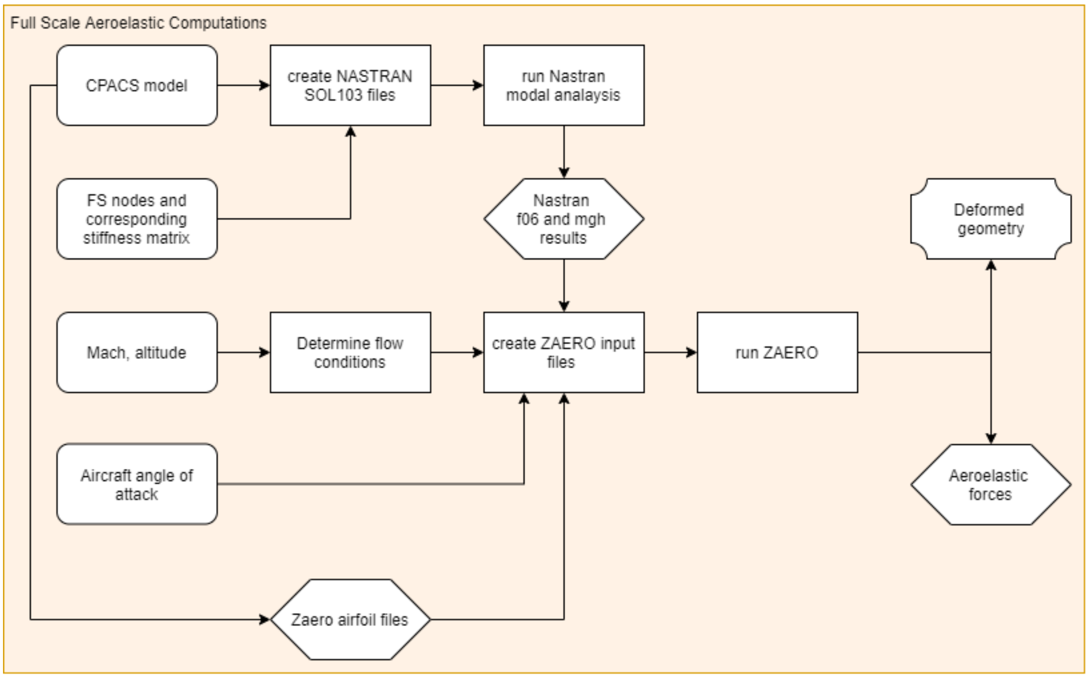

Figure B.3: Full-scale aeroelastic steps

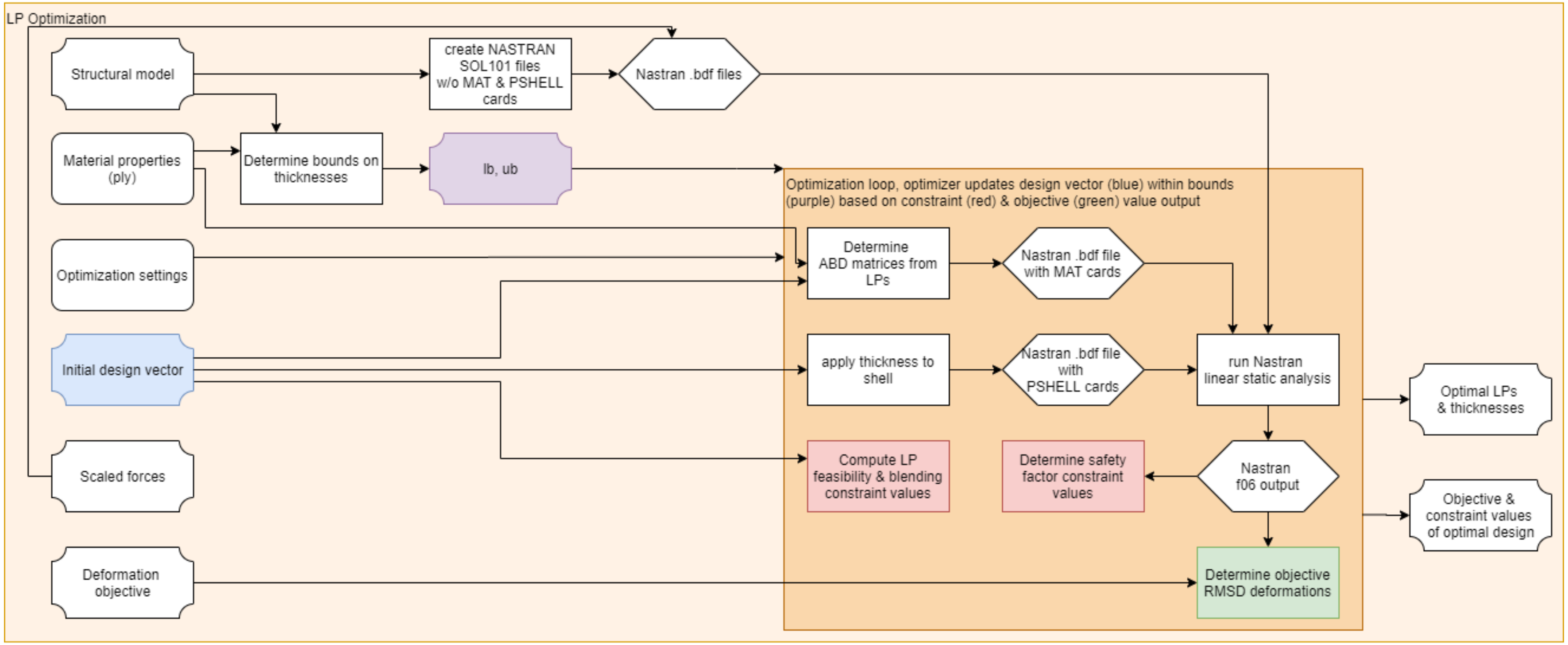

Figure B.4: Lamination parameter optimization function overview

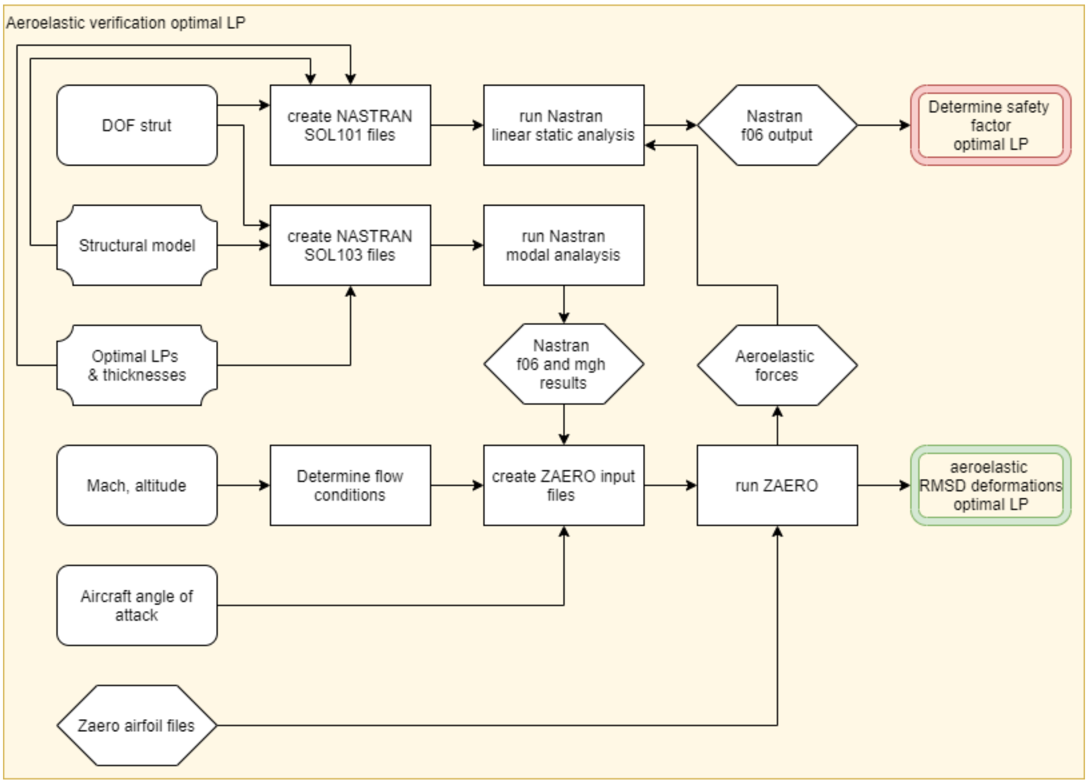

Figure B.5: Lamination parameter aeroelastic computation steps

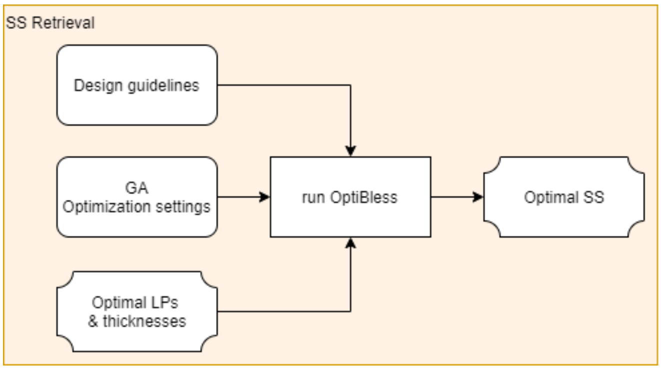

Figure B.6: Stacking sequence retrieval steps

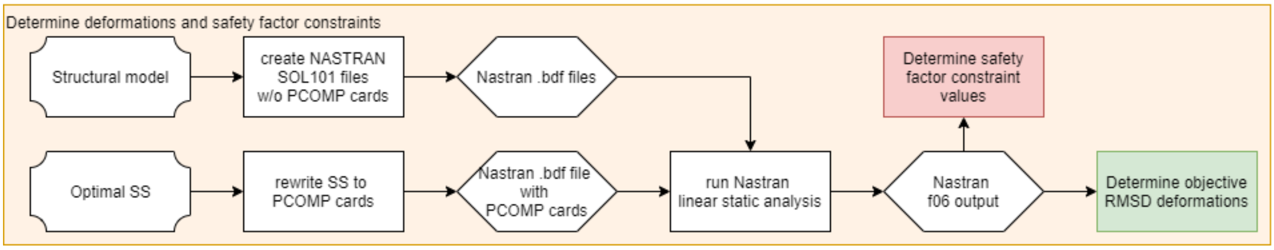

Figure B.7: Stacking sequence function value computation steps

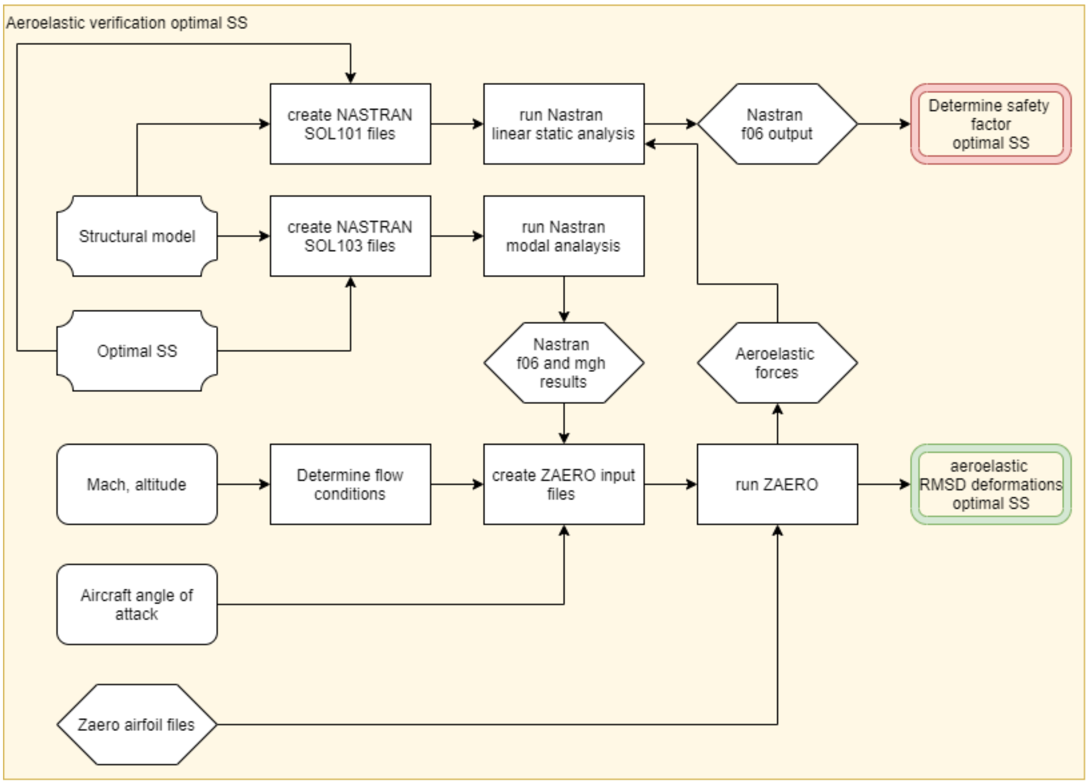

Figure B.8: Stacking sequence aeroelastic computation steps

C

Additional Results

This appendix shows additional results, one for each of the wings.

C.1. Cantilever Wing, Optimum Design for 6-Panels and $k_p = 2.5$

The results for three different angles of attack: 5 (for which was optimized), 3 and 1 degrees are shown in the sections below. The variation of the wing lift coefficient and the function value for varying angles is shown in the figure directly below.

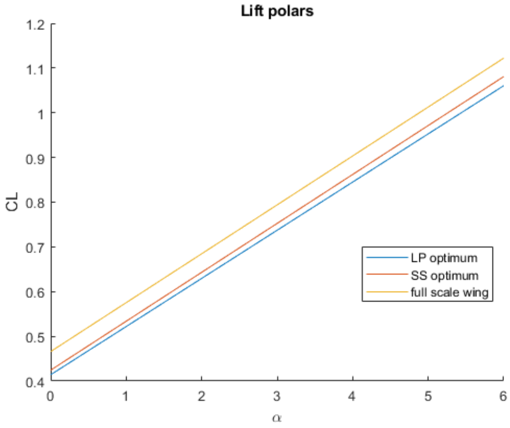

Figure C.1: Lift polar for full scale and found optima (LP and SS) after optimizing

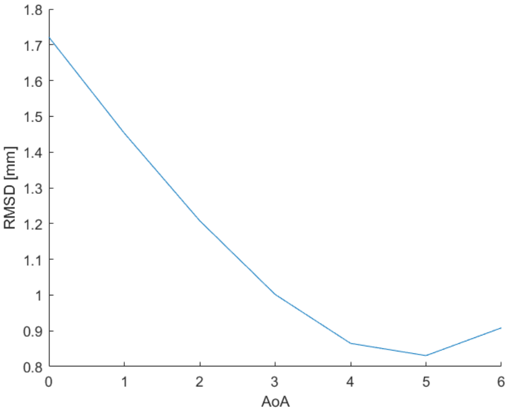

Figure C.2: RMSD with full scale deformation for best optimization result vs angles of attack

Angle of attack of 5 degrees

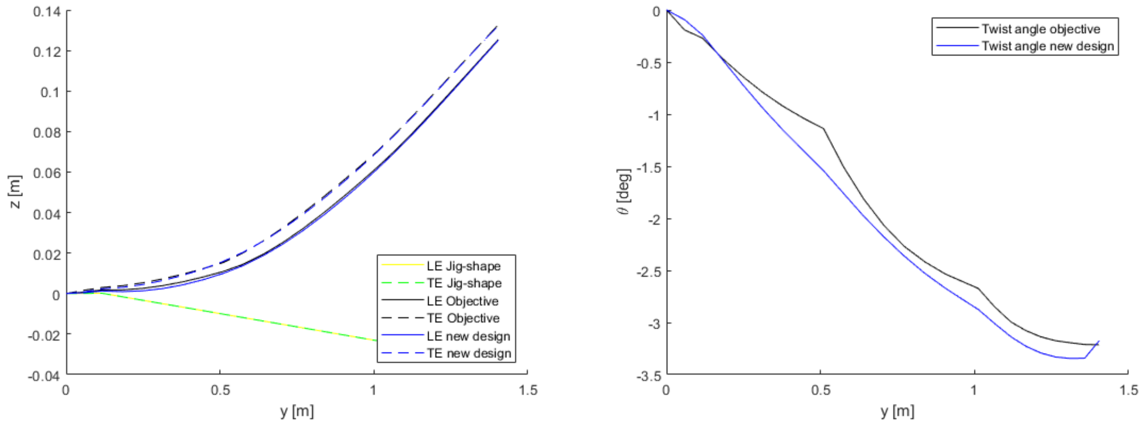

(a) Deformations (b) Twist

Figure C.3: Aeroelastic results for optimized design

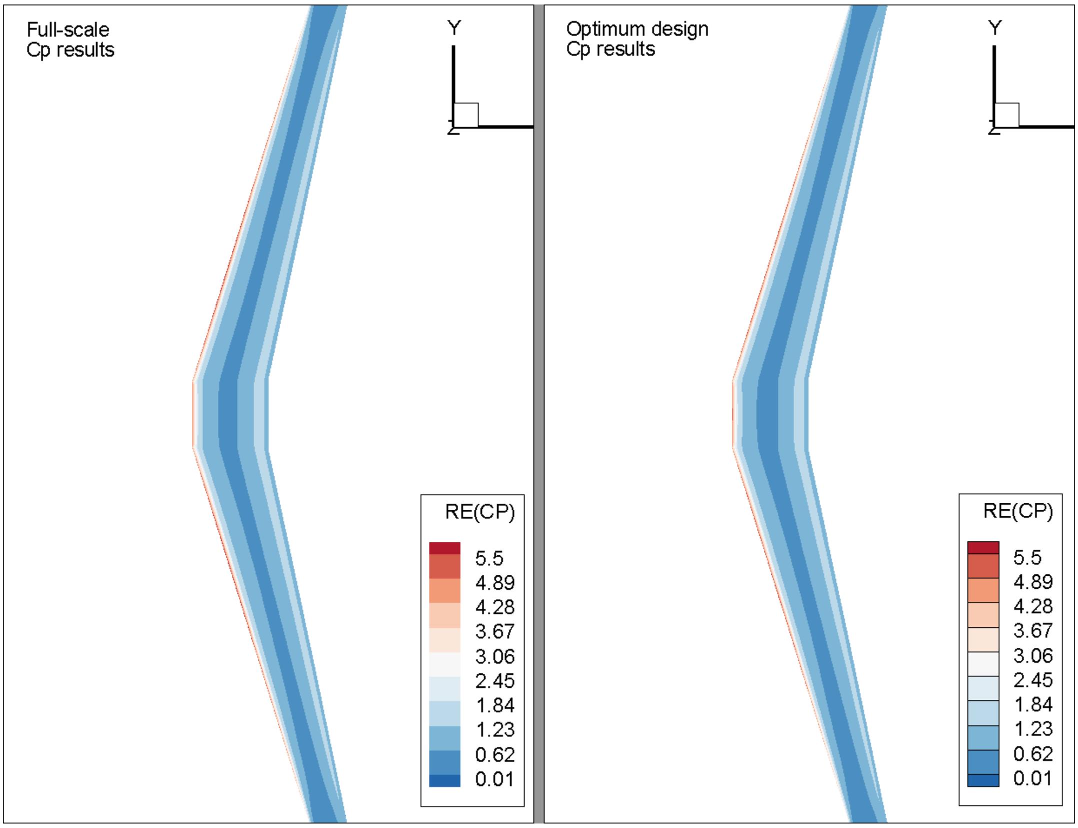

Figure C.4: Comparison between pressure coefficients of full scale and found optimum design

Angle of attack of 3 degrees

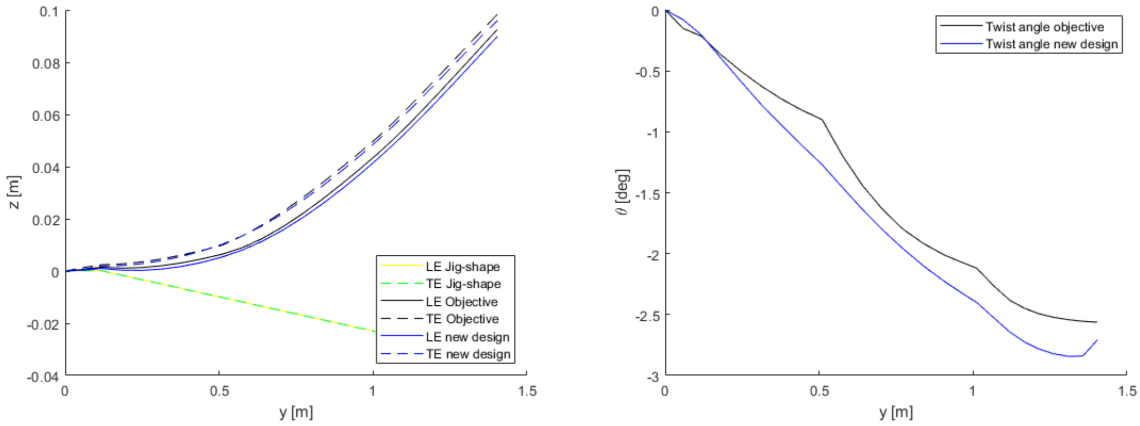

(a) Deformations (b) Twist

Figure C.5: Aeroelastic results for the stacking sequence found after optimizing

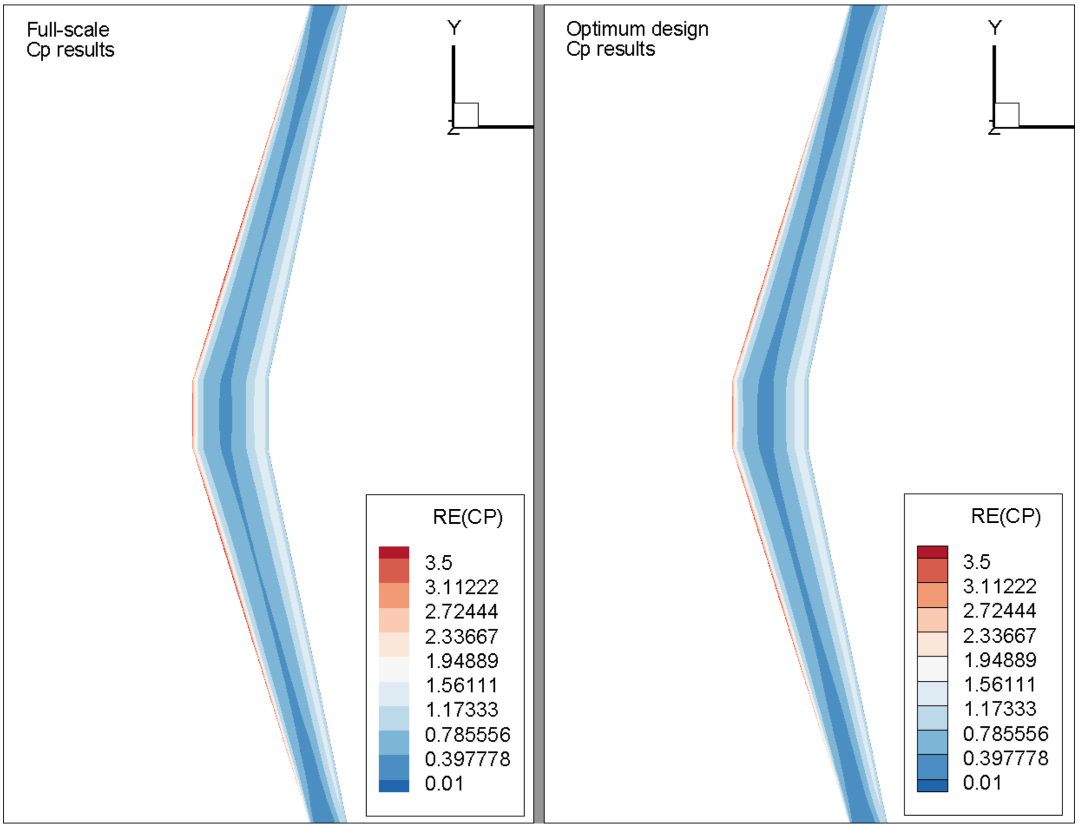

Figure C.6: Comparison between pressure coefficients of full scale and found optimum design

Angle of attack of 1 degree

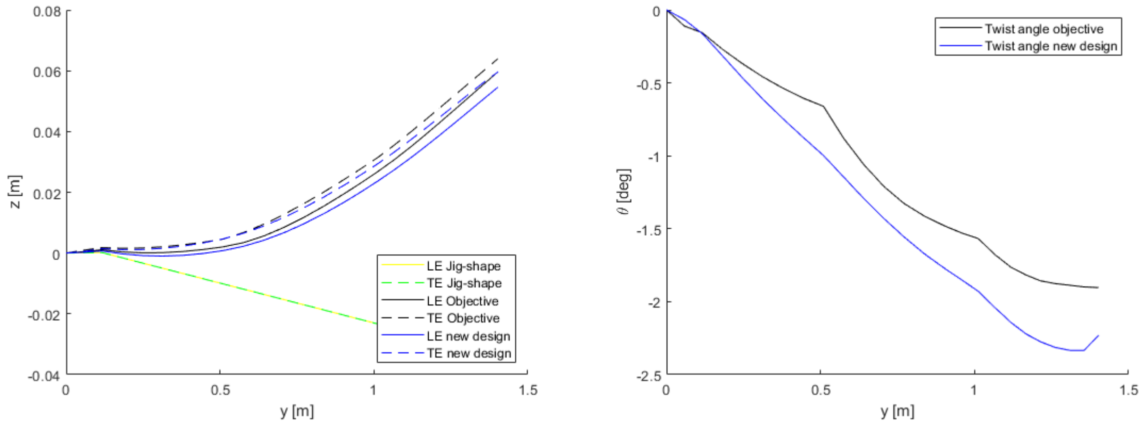

(a) Deformations (b) Twist

Figure C.7: Aeroelastic results for the stacking sequence found after optimizing

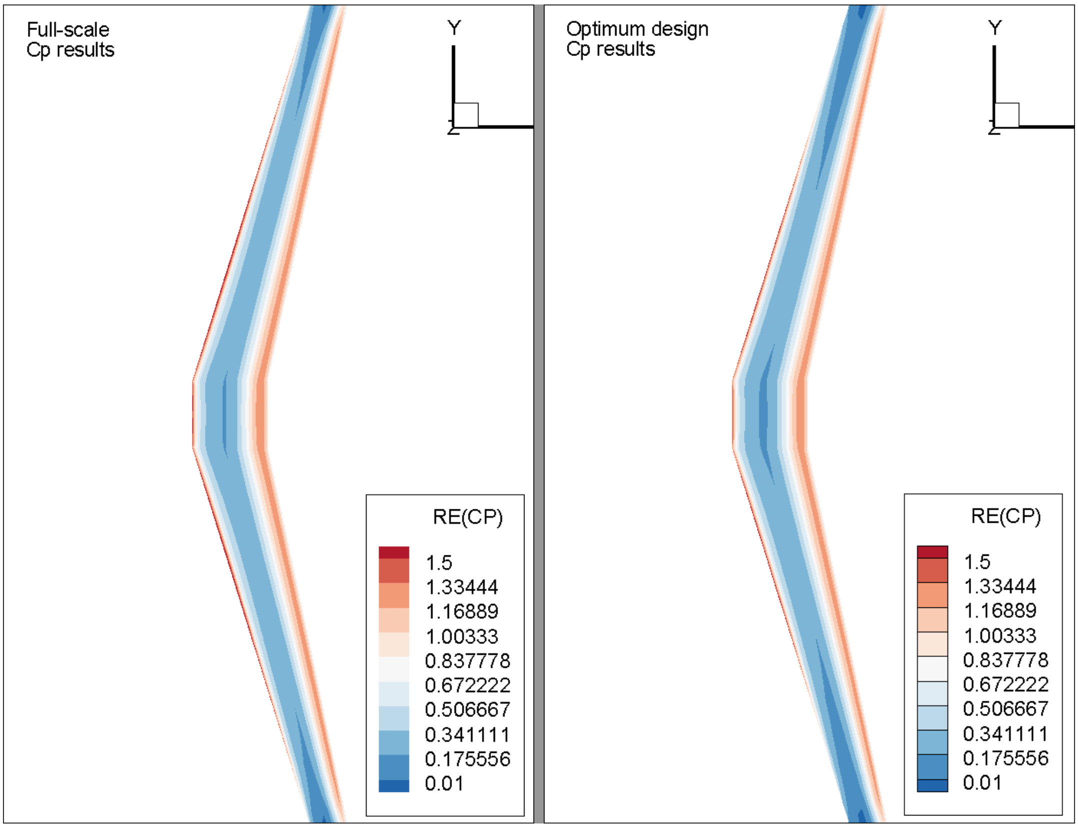

Figure C.8: Comparison between pressure coefficients of full scale and found optimum design

C.2. Strut-Braced Wing, Optimum Design for 8-Panels and $k_p = 2.5$

The results for three different angles of attack: 5 (for which was optimized), 3 and 1 are shown in the sections below. The variation of the wing lift coefficient and the function value for varying angles is shown in the figure directly below.

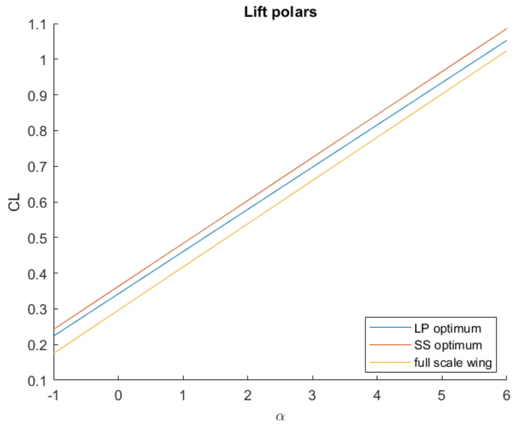

Figure C.9: Lift polar for full scale and found optima (LP and SS) after optimizing

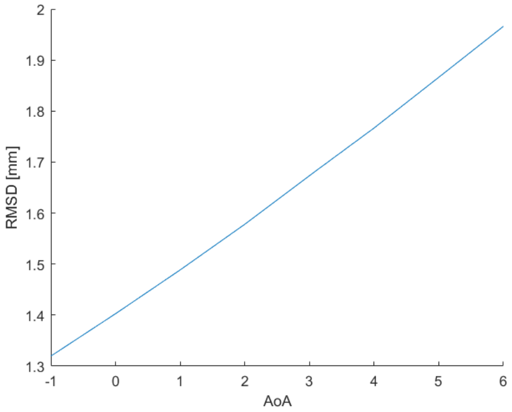

Figure C.10: RMSD with full scale deformation for best optimization result vs angles of attack

Angle of attack of 5 degrees

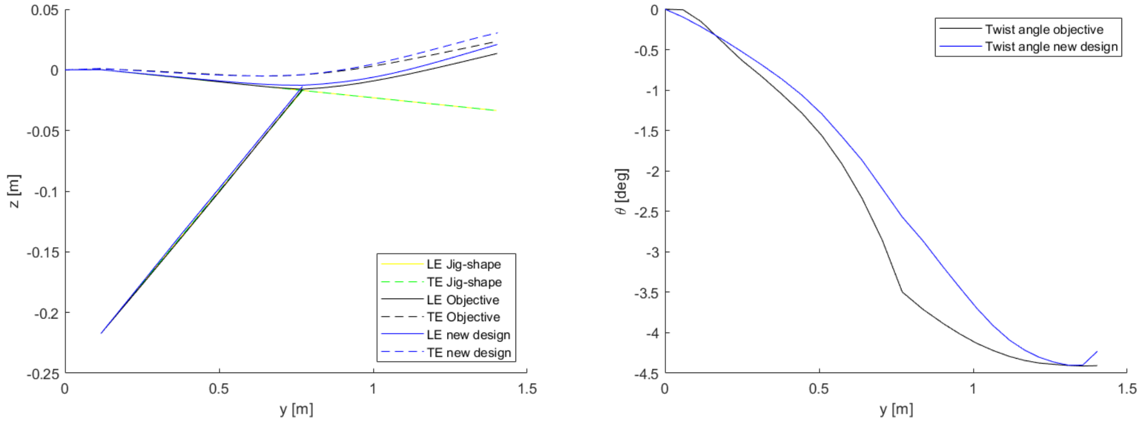

(a) Deformations

(b) Twist

Figure C.11: Aeroelastic results for optimized design

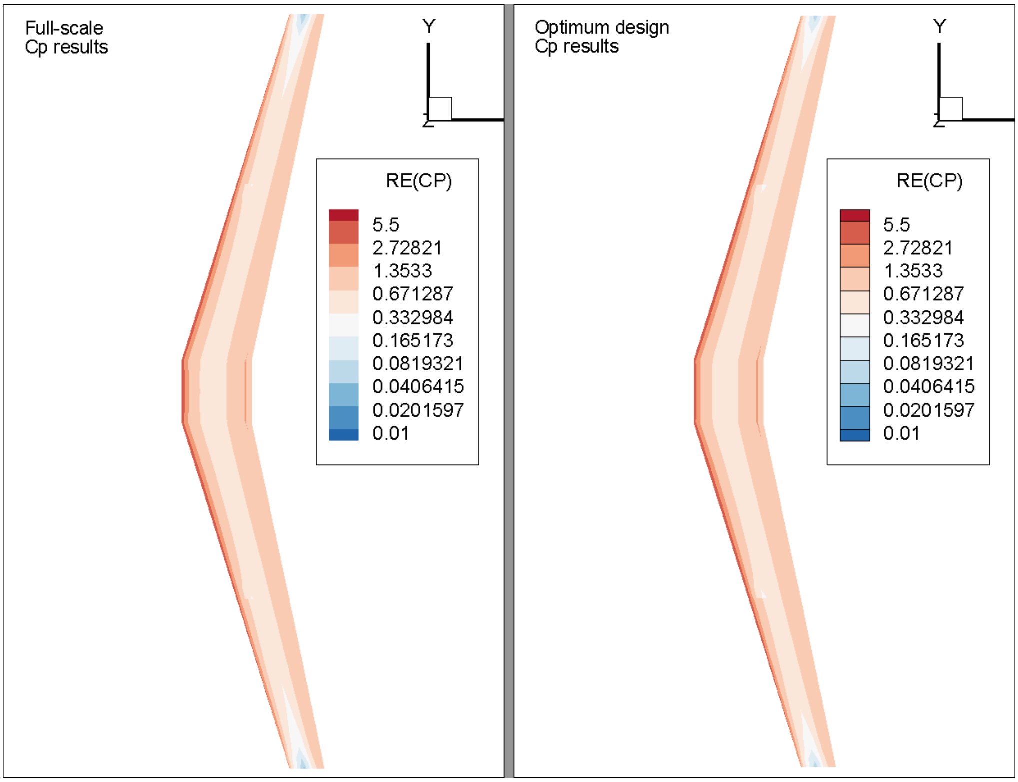

Figure C.12: Comparison between pressure coefficients of full scale and found optimum design

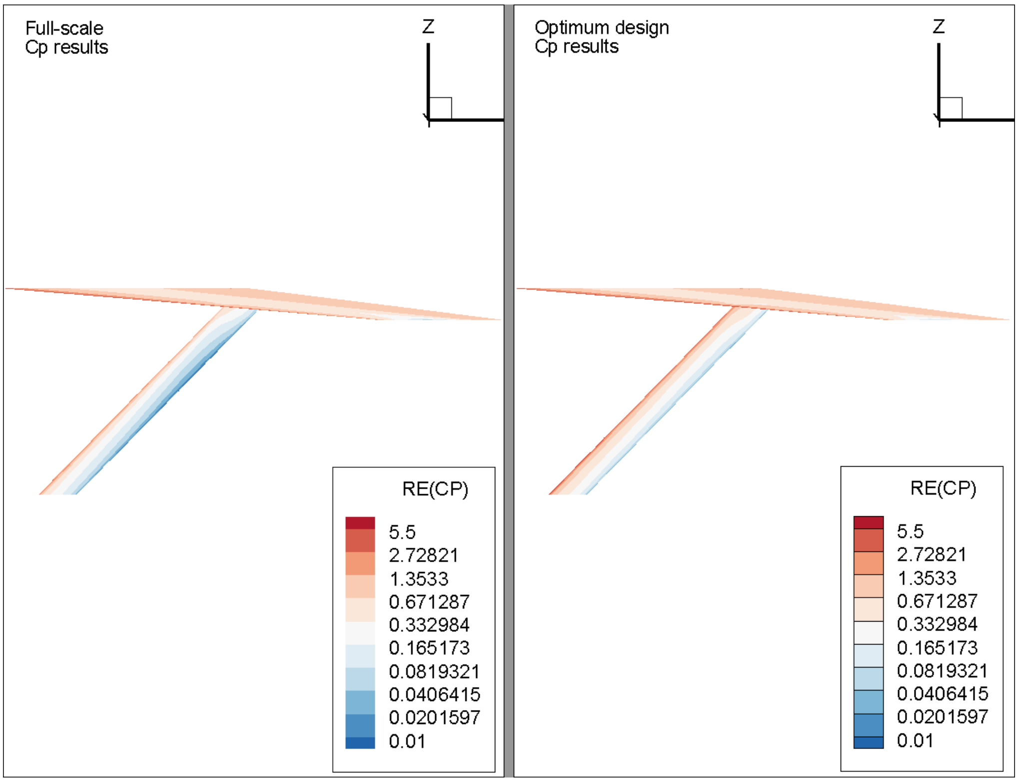

Figure C.13: Comparison between pressure coefficients of full scale and found optimum design. Side view of strut

Angle of attack of 3 degrees

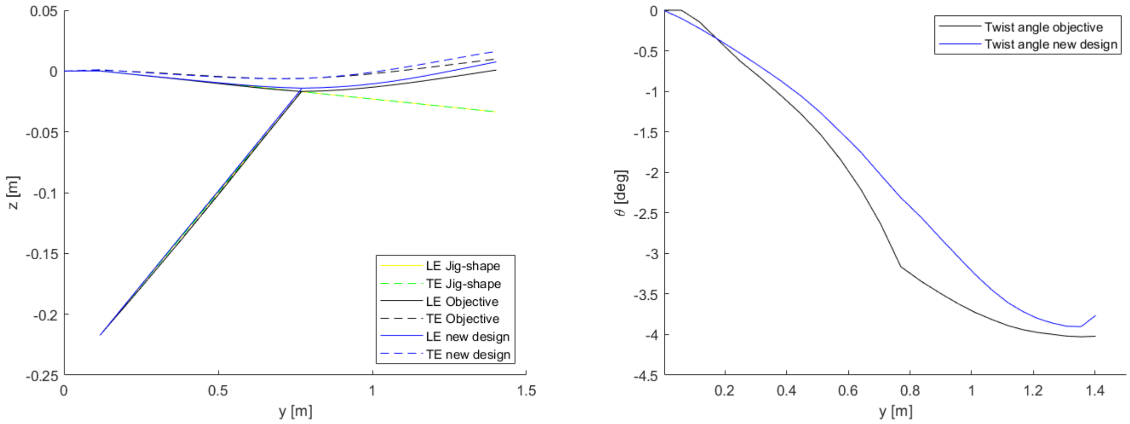

(a) Deformations

(b) Twist

Figure C.14: Aeroelastic results for optimized design

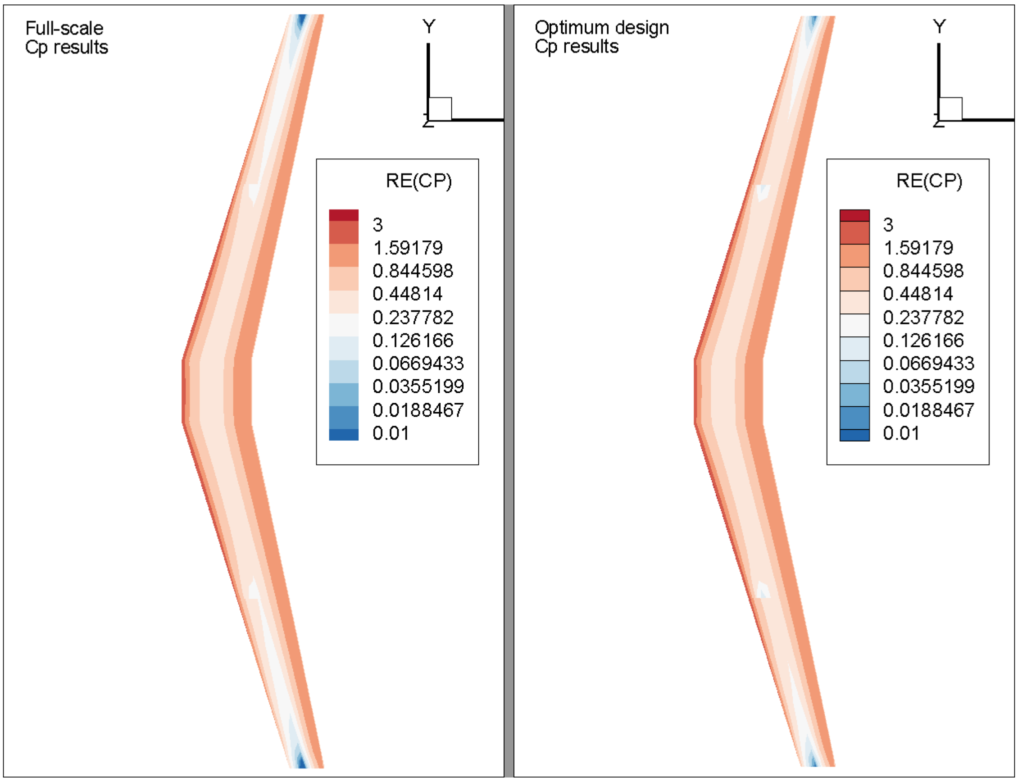

Figure C.15: Comparison between pressure coefficients of full scale and found optimum design

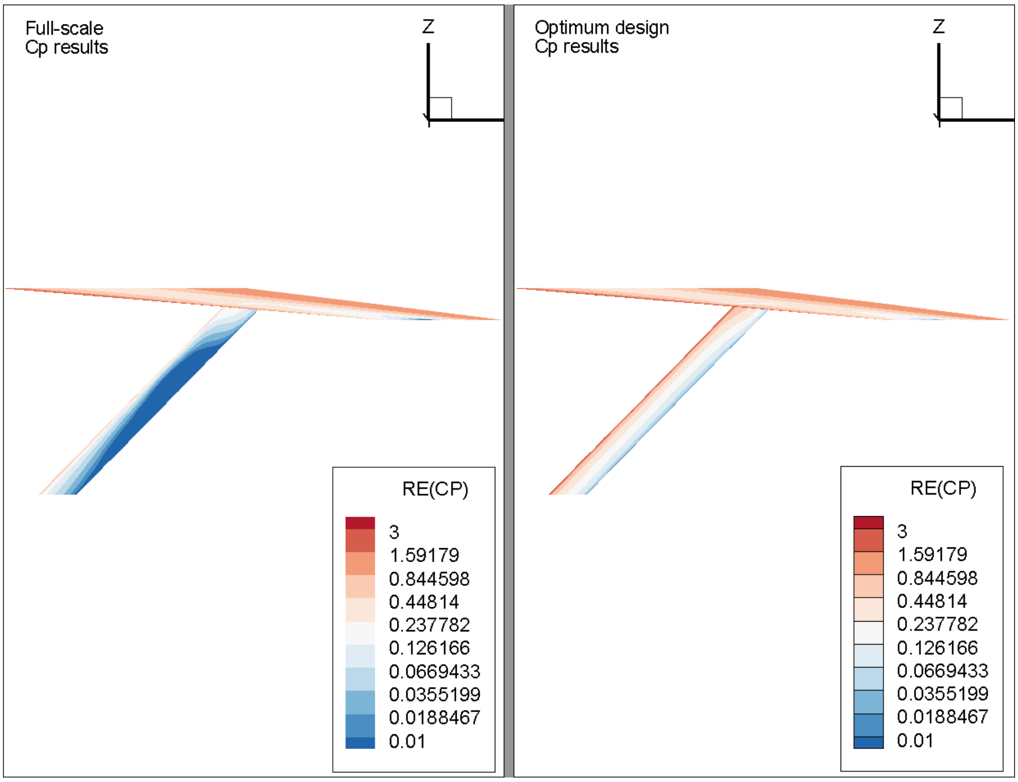

Figure C.16: Comparison between pressure coefficients of full scale and found optimum design. Side view of strut

Angle of attack of 1 degree

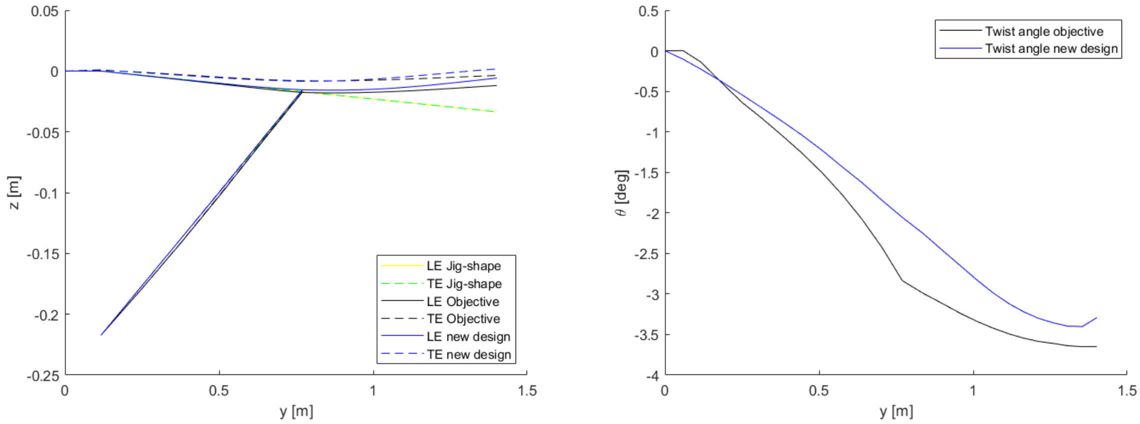

(a) Deformations

(b) Twist

Figure C.17: Aeroelastic results for optimized design

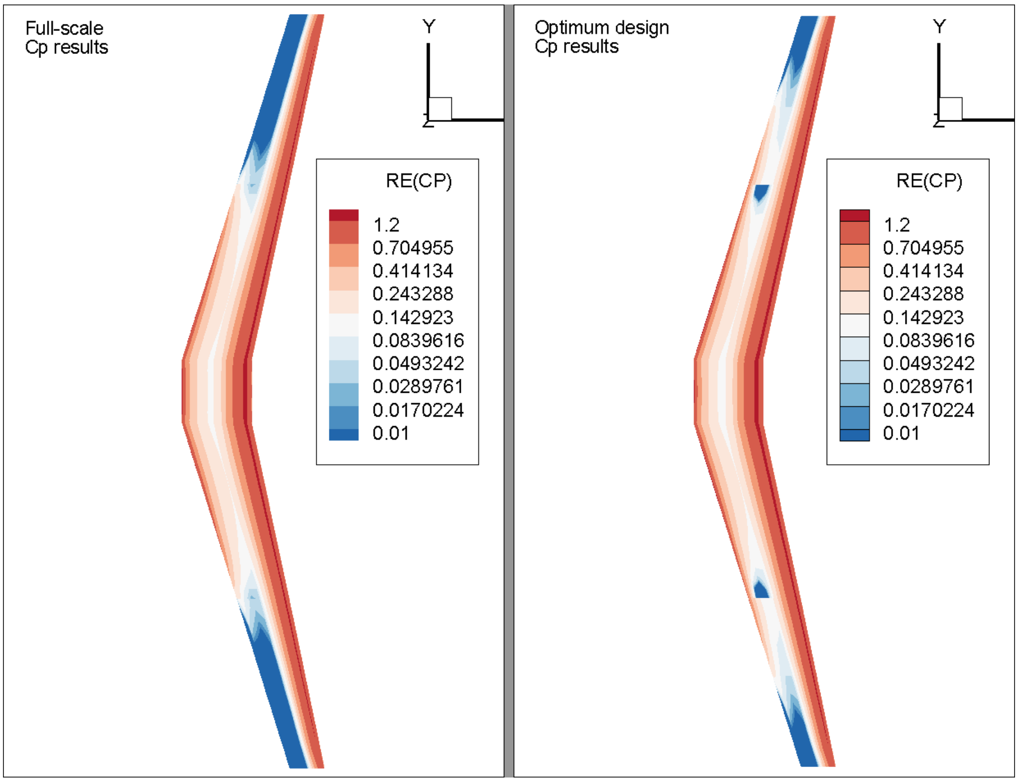

Figure C.18: Comparison between pressure coefficients of full scale and found optimum design

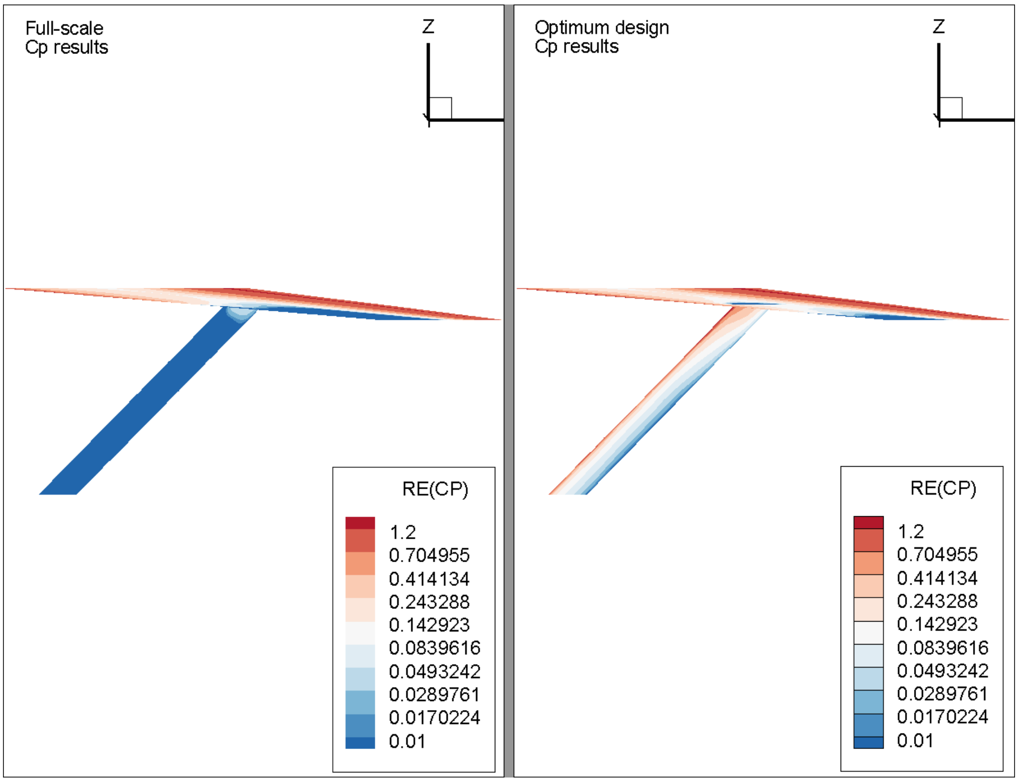

Figure C.19: Comparison between pressure coefficients of full scale and found optimum design. Side view of strut